"A STUDY OF THE PROFILES OF TWO ASTROPHYSICALLY INTERESTING NEUTRAL HELIUM LINES IN A LOW DENSITY LABORATORY PLASMA"

A thesis submitted for the Degree of

DOCTOR OF PHILOSOPHY

in the

UNIVERSITY OF LONDON

by

CHRISTOPHER JOHN CAIRNS

Department of Physics
Imperial College of Science and Technology
South Kensington
London SW 7

August 1970

ABSTRACT

This thesis describes an experiment to obtain line profiles of two neutral helium lines, 4^3D-2^3P at 4471A and 4^1D-2^1P at 4922A emitted by a low density helium plasma. Both of these lines have a forbidden component corresponding to the forbidden transitions 4^3F- 2^3P and 4^1F-2^1P the intensities of which are strongly dependent on the electron density of the plasma. The laboratory source used in the experiment was a pulsed, linear pinch observed in the afterglow of the decaying plasma in the region $T \sim 5,000$-$15,000$ °K and $n_e \sim 10^{15} - 10^{14}$. Profiles of the lines, obtained at $n_e = 10^{15}$ and $n = 4.10^{14}$, have been compared to the recently calculated theoretical profiles of Barnard, Cooper and Shamey and of Griem. Certain discrepancies between theory and experiment in the intensity of the forbidden line have been discovered and this has been explained in terms of the breakdown of the quasi-static approximation for the ions in the centre of the forbidden line.

TABLE OF CONTENTS

CHAPTER 1

INTRODUCTION

Some years ago, Baranger (1958) laid down the foundation of modern line broadening theory by developing the impact approximation for electron perturbers acting on spectral lines emitted from a plasma. This work was continued by Griem, Baranger, Kolb and Oertel (1962) and is now generally referred to as the GBKO theory. The theory has been reviewed on numerous occasions, i.e. Baranger (1962) and Cooper (1965), and consequently a further review will not be given here.

Since publication of the GBKO theory, there has been a great deal of work done on the comparison of experiment and theory. The hydrogen lines H_α , H_β and H_γ in particular have been studied with great care. Berg et al (1962) have published

comparisons of calculated profiles of H_β with experimental points and found agreement between the predicted and measured half-widths was 3%. They also found that for H_α and H_γ agreement between theory and experiment was about 15%. Many neutral helium lines have also been compared with the theory (see Berg et al [1962]) and here the theory-experiment agreement is typically about 20% for the half widths. In general, the further away from the hydrogenic case one goes, the worse is the theory-experiment agreement. This is demonstrated, for instance, in the measured half widths of A II and A III lines obtained by Roberts (1967), where theory-experiment agreement is often a factor of two or more out. Alternatively, for the He II lines 4686 and 3203, which are of course hydrogenic, theory and experiment agree to 10% (see Berg et al [1962]).

The theoretical calculations fall into two separate regimes. First, the statistical part which considers the physics of the perturbers and the way in which they can collide with emitters and disturb their wave trains. Secondly, the part which deals with the wave functions of the quantum mechanical states of the emitters. The excellent theory-experiment agreement for hydrogenic lines, where the emitted wave function can be calculated exactly, suggests strongly that the physics of the perturber statistics is correct.

In this way, the theory-experiment discrepancies which appear in the non-hydrogenic situation are probably due largely to errors in the emitter wave functions.

We have seen, then, that the GBKO theory is capable of accurately predicting the line profiles of hydrogen and helium. However, some of these lines, until recently, have presented theoretical difficulties. To understand how these difficulties arise, consider the following four categories which specify different types of line profiles:

(a) Hydrogenic
(b) non-hydrogenic
(c) isolated
(d) non-isolated.

The first two are self-explanatory. That is, for a hydrogenic emitter, there exists ℓ degeneracy between the states of the same principle quantum number. Electron collisions can then cause elastic transitions between these states. The difference between the second two has a similar basis. A line is isolated if the energy gap between the upper state of the radiating transition and its nearest neighbour is greater than the half-width of the line. ie $\Delta\omega \leq \omega_{\alpha\alpha'}$, where $\Delta\omega$ is the

half width and $\omega_{\alpha\alpha'}$ the energy separation between the two upper states. On this definition all hydrogenic lines must be overlapping. And indeed they are. However, the extremely small values of $\omega_{\alpha\alpha'}$ ($\omega_{\alpha\alpha'} \neq 0$ because of the Stark splitting by the ion-micro field) distinguish hydrogenic atoms from atoms where the splitting is small but finite. Hence we can differentiate three types of line: Hydrogenic, where the upper state splitting is determined by the Stark effect of the ion field and are therefore small compared with the line width. Overlapping and partially overlapping non-hydrogenic where $\omega_{\alpha\alpha'} \gtrsim \Delta\omega$,

and finaly, isolated lines defined by $\omega_{\alpha\alpha'} > \Delta\omega$.

RECENT THEORETICAL WORK

The GBKO theory was originally developed to deal with hydrogenic lines and we have seen that it shows excellent agreement with experiment. A simplification of the theory is capable of dealing with isolated lines also. See, for example, the neutral helium lines referenced above. However, until recently, the theory has not been applied to overlapping and partially overlapping non-hydrogenic lines. Barnard, Cooper and Shamey (1969), which will be referred to as BCS, and Griem*(1968) rectified this

*(Griem does 4471 only.)

situation by calculating the profiles of the neutral helium lines at 4471Å and 4922Å using the GBKO theory as a basis.

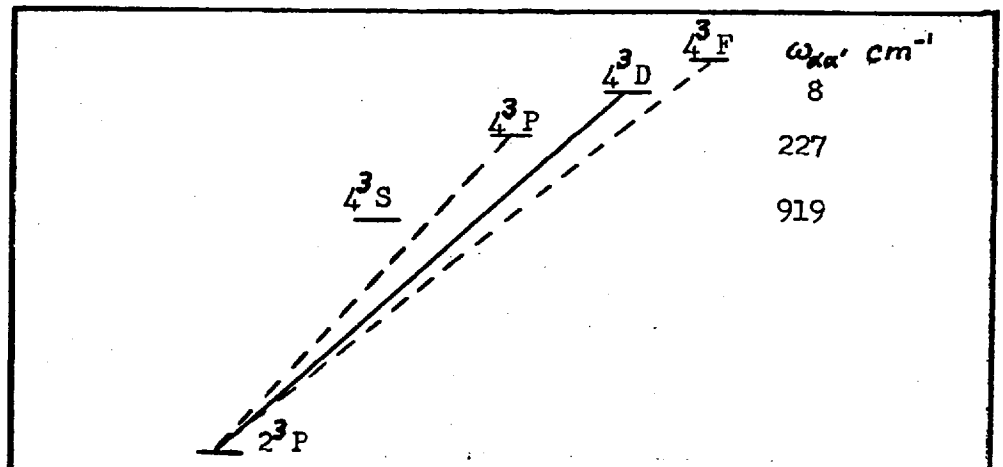

FIG. 1.1 Term diagram for HE I line 4471 with forbidden components

These two lines are particularly useful as a check on the theory. The line at 4471Å is the 4^3 D - 2^3 P transition and the line at 4922Å is 4^1 D - 2^1 P. As far as the following discussion is concerned, the two lines are similar and so reference will be made to only one of them, the triplet system.

The energy splittings between the sublevels of the upper state, n = 4, are shown in Fig. 1.1. The full line represents the allowed transition 4^3 D - 2^3 P and the two dotted lines the 'forbidden' transitions 4^3 P, 4^3 F - 2^3 P. How forbidden transitions arise will be discussed in Chapter 2.

For electron densities below 10^{14}, the smallest energy gap, $4^3D - 4^3F = 8\ cms^{-1}$, is larger than the line width and the three lines can be calculated using the theory for isolated lines. When $10^{14} \lesssim n_e \lesssim 10^{15}$ the line width $\Delta\omega \simeq \omega_{^3F-^3D}$, and the lines 4^3D, $4^3F - 2^3P$ are partially overlapping. At higher densities, these two lines become fully overlapping and for $n_e > 10^{17}$ the second forbidden line, $4^3P - 2^3P$, also begins to overlap with the other two. That is, by increasing the electron density, the line profile system goes smoothly from the isolated regime to the partially overlapping and then to the fully overlapping regime.

Griem and B.C.S. have calculated profiles for the lines over a range of densities and temperatures, $10^{14} \leq n_e \leq 10^{17}$ and $5{,}000^{\circ}k \leq T \leq 40{,}000^{\circ}k$ where T is the temperature of the electrons, ions and atoms, all assumed to be equal. A review of their calculations, with a special emphasis on where they differ from each other will be given in Chapter 3. It is the purpose of this thesis to compare the profiles of B.C.S. and Griem with experimentally obtained profiles and to comment on where the two calculated profiles differ from experiment.

PREVIOUS EXPERIMENTAL WORK

Previous experimental work on the lines 4471 and 4922 has been stimulated by the importance of the profiles of the lines in astrophysics. O and B class stars, which are particularly important to astrophysics because of the early position they occupy in the evolution of stellar histories, emit the lines 4471 and 4922 in absorption. The profiles of 4471 and 4922 are extremely sensitive to electron density. Hence, by studying the profiles emitted from the atmospheres of O and B class stars, and comparing them with profiles predicted by theory with a constructed model atmosphere for the star, (see Underhill 1966), an estimate of the electron density at various depths into the atmosphere of the star can be made. This, in turn, leads to further estimates of the star surface gravity and helium abundance.

Since Struve (1929) first identified the line 4471, together with its forbidden component, in a stellar spectrum, Wulff (1958) and Sadjian et al (1961) have obtained laboratory profiles. Wulff, using a pulsed arc source with $n_e = 3.10^{16}$ and $T = 30{,}000^{\circ}K$ obtained profiles which later proved to be in good agreement with B.C.S. The comparison was made by B.C.S.

and they claim agreement to within a few per cent for the intensity of the forbidden component $4^3F - 2^3P$, which is particularly sensitive to n_e. It should be pointed out that their comparison is not very decisive because Wulff could not obtain independent measurements of n_e. Instead, half-widths taken from many measured lines have been fitted to theory and a best value of n_e extracted. Sadjian's profiles, this time for 4922, were made at $n_e = 5.10^{16}$, and $T = 19{,}000^{\circ}K$. The source was a high purity Gerdien arc (1922). Electron density measurements were obtained from the Inglis-Teller relation, $\log_{10} n_e = 23.2 - 7.5 \log_{10} n$ where n is the principal quantum number of the highest observed member of a particular series, in their case $n = 7$. This is not a very accurate method and Sadjian in fact quotes $3.10^{16} \leq n_e \leq 7.10^{16}$. The factor of two uncertainty in n_e makes a precise comparison of his experiment with theory impossible.

More recently, Jenkins (1970) and Nelson (1970) have also worked on 4471. Jenkins used a pulsed linear discharge, very similar to the apparatus used in the present work, and observed profiles in the early stages of the discharge when the plasma was still pinched. His plasma parameters were $n_e \simeq 10^{16}$ and $T_e = 40{,}000^{\circ}K$. Measurements of isolated helium lines were in

good agreement with theory but 4471 showed an appreciable discrepancy with theory in the region of the forbidden line. However, he has shown, by careful measurements of radial density gradients using a laser interferometer, and radial emission coefficients, that radial gradients dominate the precise form of the profile. That is, by choosing a model plasma, which he has shown experimentally to be reasonable, the theory-experiment discrepancy can be accounted for. This does not mean that Jenkins has verified the Griem-BCS calculations, only that it could be correct. Nelson has obtained profiles on a pulsed arc at $n_e = 5.10^{16}$ and $T_e = 50{,}000^{\circ}K$. The electron density was taken from the half-widths of isolated lines whose density dependence has been well verified in the past. Comparison with BCS produced agreement of about 5% in the region of the 4^3D, $4^3F - 2^3P$ transitions and the area between them. In the far wings of the lines, Nelson's profile is about 40% lower than BCS. This fit between experiment and theory is obtained after normalising not only the peak height and wavelength of the $4^3D - 2^3P$ line but also he adjusts the position of the forbidden $4^3F - 2^3P$ line by shifting it 2Å nearer the allowed line. The justification is that the theory is not good at predicting line

shifts anyway and a small arbitrary shift is allowable. Doing this changes the intensity of his measured profile in the centre of the dip between the two lines by about 70% and brings it to about 5% of BCS. Without making this adjustment, theory-experiment fit is rather poor.

The works referred to above have been carried out in the range $10^{16} \leq n_e \leq 10^{17}$. This is a higher range than that of interest to astrophysicists studying O and B class stars where, typically, $10^{12} \leq n_e \leq 10^{16}$. To the author's knowledge, no laboratory work has been done on 4471 in this range. It was therefore decided to try to measure profiles at such electron densities with the double objective of checking the calculations of BCS and Griem at low densities and providing accurate profiles for the use of astrophysicists.

CHOICE OF APPARATUS

Jenkins (1970) has worked extensively on a linear pinch at Imperial College. He has been primarily concerned with the early stages of the discharge when the plasma was still compressed by magnetic fields and he has measured plasma parameters of typically $n_e \simeq 10^{16}$ and $T = 40{,}000^{\circ}K$. The discharge was reproducible to

about 5% from shot to shot which makes it useful for measuring line profiles from shot to shot measurements. The main difficulty encountered was due to radial gradients in the plasma which Jenkins discussed at length in his thesis, Observations made by Jenkins at later times, in the afterglow of the plasma, showed that the electron density decayed smoothly and reproducibly down to 10^{14}. At these later times, when currents are no longer flowing in the plasma, one can expect that radial gradients will be less pronounced and the reproducibility even better. A linear discharge, similar to the apparatus used by Jenkins, was built. A description of the apparatus and the equipment for detecting and measuring profiles is given in Chapter 4. Preliminary experiments on the discharge showed that, as was hoped, electron densities and temperatures were in the required range ($10^{14} \leq n_e \leq 10^{15}$; $T_e = 10.000^{\circ}K$), the discharge was sufficiently reproducible ($\simeq$ 5% from shot to shot) and, the most important, radial density gradients were not strong enough to make the interpretation of the profiles impossible.

CHAPTER 2

A PHYSICAL DESCRIPTION OF THE LINE BROADENING THEORY

In Chapter 3, a detailed review of the calculations of the two helium lines by BCS and Griem will be given. Before this, however, it is helpful to summarise briefly the present line broadening theory with a special emphasis on the physical mechanisms involved rather than on a detailed mathematical description. The full mathematical treatment is contained in the original papers of Baranger (1958) and GBKO (1962) and in the review articles of Cooper (1966) and Baranger (1962). Much of the account given below has been obtained from these publications and also from Burgess (1967).

The starting point for line broadening theory is the well known result for the power spectrum of a radiating quantum mechanical system.

$$P(\omega_{if}) = \frac{4}{3}\frac{\omega_{if}^4}{c^3}|\langle f|d|i\rangle|^2 \qquad 2.1$$

f and i are the final, initial states of a dipole transition induced by the dipole operator d and ω_{if} the frequency of the radiation. Eq. 2.1 can be rewritten.

$$P(\omega_{if}) = \frac{4}{3}\frac{\omega^4}{c^3}L(\omega) \qquad 2.2$$

Here, we have introduced the line shape function $L(\omega)$ which includes the matrix elements $\langle f|d|i\rangle$. It is often easier, and has become conventional, to calculate the Fourrier Transform of $L(\omega)$ rather than $L(\omega)$ itself. The Fourrier Transform is defined by

$$C(t) = \frac{1}{\pi}\int_{-\infty}^{\infty} e^{i\omega t}L(\omega)d\omega \qquad 2.3$$

THE AUTO-CORRELATION FUNCTION

The function C(t) can be identified as the auto-correlation function of the emitted light amplitude. Physically, this means

that C(t) is a measure of the extent to which the light train emitted at some time, s, correlates with itself at some later time, t + s. Consider Fig. 2.1 which represents a perfect monochromatic wave extending to t = $\pm\infty$.

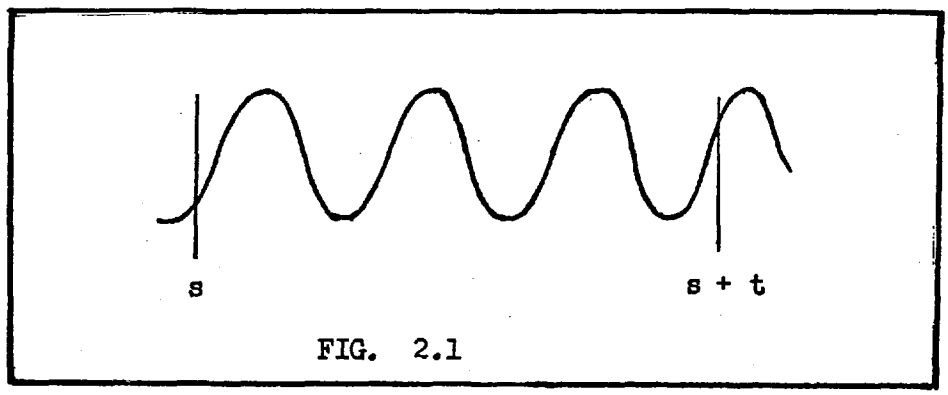

FIG. 2.1

It can be shown by the Wiener-Kinchine theorem (1934) that

$$C(t) = \lim_{S\to\infty} \frac{1}{S} \int_{-S/2}^{S/2} f^*(s) f(s+t)\, ds \qquad 2.4$$

Where f(s) is the function describing the dipole oscillator. In this case

$$f(s) = e^{i\omega_0 s} \qquad 2.5$$

Substituting eq. 2.5 into eq. 2.4 gives

$$C(t) = \lim_{S\to\infty} \frac{1}{S} \int_{-S/2}^{S/2} e^{-i\omega_0 s}\, e^{i\omega_0 (s+t)}\, ds$$

$$= e^{i\omega_0 t}$$

and $L(\omega) = \delta(\omega - \omega_0)$.

Now suppose the pure wave train is disturbed at some time, t_o, in the interval t. This is represented in Fig. 2.2 and it can be seen that in this particular case the perturbation is equivalent to a phase shift in the wave train.

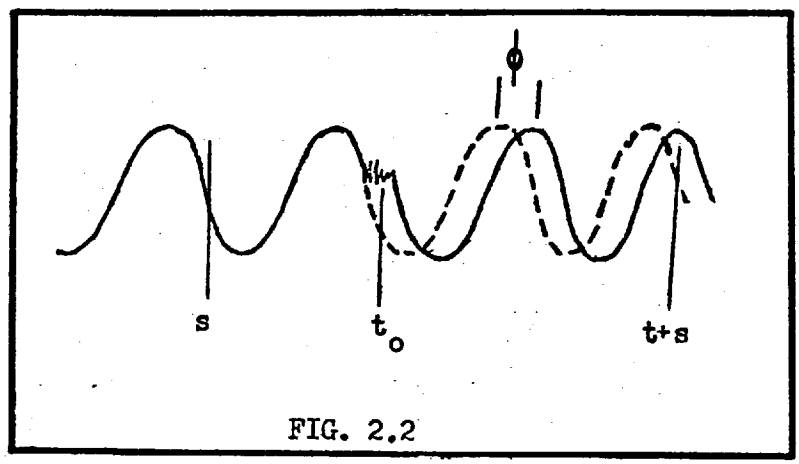

FIG. 2.2

In this case

$$f(s) = e^{i\omega_o s} \quad ; \qquad f(s+t) = e^{i\omega_o(s+t)+i\phi}$$

Now if similar collisions are occurring throughout the whole of the wave train, then the total phase change in some interval t can de defined as $\eta(t)$. It is necessary to impose many collisions because clearly, the effect of one collision is negligible as the limit $s \to \pm\infty$ is taken. Then

$$f(s) = e^{i(\omega_o s + \eta(s))}$$

$$f(s+t) = e^{i(\omega_o \overline{s+t} + \eta(s+t))}$$

Manipulation of the above equations yields

$$C(t) = e^{-nv(\sigma_r - i\sigma_i)t}$$

where n is the perturber number density, v is their average velocity and

$$nvdt(\sigma_r - i\sigma_i) = \langle e^{i\eta} - 1 \rangle_{Av.} \qquad 2.6$$

The exact derivation and meaning of eq. 2.6 need not concern us here. What is interesting is that, in this case

$$L(\omega) \sim [(\omega - \omega_o - nv\sigma_i)^2 + (nv\sigma_r)^2]^{-1} \qquad 2.7$$

Hence the line shape is dispersive and has a shift of $nv\sigma_i$ and a width of $nv\sigma_r$. A better physical understanding of what happens to line shape can be obtained by writing $\eta(t) = \int \phi(t) d\nu$ where the integral is over all perturbers and perturber velocities. Then eq. 2.6 becomes

$$\langle e^{i\eta} - 1 \rangle_{Av} \simeq \int [1 - \cos\phi] d\nu + i \int \sin\phi \, d\nu$$

The width, w , and shift, d , are therefore

$$w \sim \int [1 - \cos\phi] d\nu \qquad 2.8$$

$$d \sim \int \sin\phi \, d\nu \qquad 2.9$$

The width is caused mainly by phase changes $> \pi$ and the shift mainly by those $< \pi$. Physically, this can be understood by the concept of phase 'memory'. If ϕ is small and positive (say), we can equally well put ϕ as large and negative, i.e. $\phi = -(2\pi - \phi)$. However, the wave can remember its phase for small changes and 'remembers' that ϕ is really small and positive. The effect is, therefore, a phase change in the wave train. When ϕ becomes large, memory is lost. The wave does not know whether the change is positive or negative and hence only a broadening effect is observed.

Now, alternatively, let the radiation be totally terminated and then started up again at some long time later. Then clearly there will be no correlation between the two wave trains. Thus, the lifetime of the emitter has been shortened and a broadening of the line will result.

TWO APPROXIMATIONS USED TO CALCULATE THE AUTO-CORRELATION FUNCTION

It is important, now, to establish a relationship between the auto-correlation function and the line shape. The time intervals, Δt, involved in $C(t)$ are related to the separation, $\Delta \omega$, from the line centre of the corresponding point on the

line profile by

$$\Delta t \, \Delta \omega \simeq 1 \qquad 2.10$$

Therefore, in order to study the profile close to the line centre, it is necessary to calculate $C(t)$ for large Δt and similarly, to look at the line wings, small Δt must be considered.

We can also define another time, τ , over which a perturbing particle interacts with the emitter. A comparison of τ with Δt leads to two possible extreme limits.

1. $\Delta t_1 \gg \tau$

2. $\Delta t_2 \ll \tau$

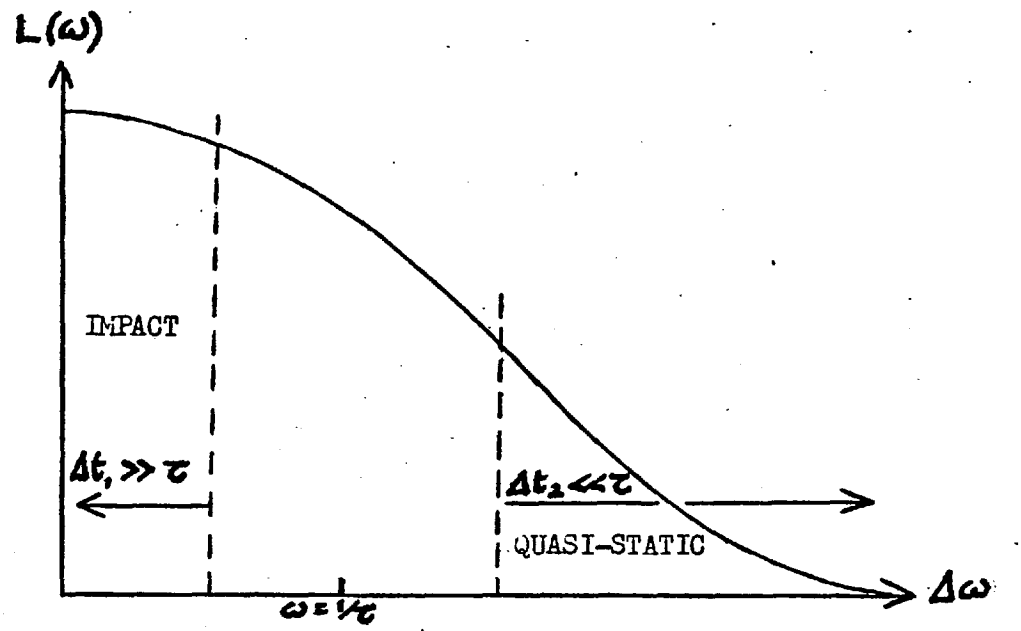

FIG. 2.3 Validity regions of Impact and Quasi-static approximations

Fig. 2.3 represents a line profile in which both extremes exist together with an intermediate region in which neither case is true. Such a line is unlikely to exist for a single value of τ . The exact position of the boundaries is not very well defined.

Consider case 1. Here the time involved in $C(t)$ is so large compared to a perturber collision time that the collision may be considered as an impact. That is, we are not interested in the exact form of the interaction, only in its final effect on the emitter. This is known as the impact approximation.

The second case says that in times Δt_2, the perturber does not appreciably change its position. Hence, the effect on the emitter of such perturbers can be calculated assuming they are static and then an average can be taken over all possible configurations of perturbers. This is the Quasi-Static approximation.

The great advantage of these extreme limits can be seen by looking at the form of the interaction time τ. For a perturber with impact parameter ρ and velocity v, τ can be written

$$\tau \simeq \frac{\rho}{v} \qquad 2.11$$

For typical laboratory plasmas, it frequently happens that for many lines, the ions may be treated on the quasi-static approximation and the electrons on the impact approximation. Fig. 2.4 shows a line in which this occurs. The reason that this can happen is, of course, because of the much greater thermal velocity of the electrons.

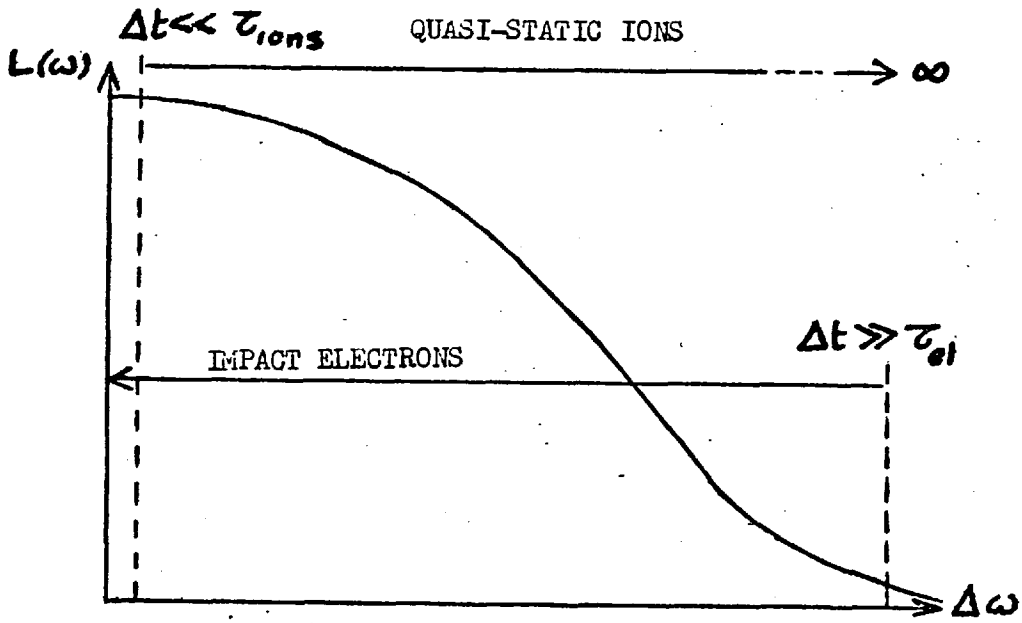

FIG. 2.4 Typical Validity regions for Quasi-static and impact approximations for ions and electrons

These two approximations will be individually discussed in the next sections.

THE QUASI-STATIC APPROXIMATION

We have seen that very often the ions may be considered as being stationary in the calculation of C(t). This does not mean that the ion-field, F, does not change. Only that we can

calculate C(t) for a particular ion-field in the presence of electron perturbers and then sum over all possible ion-fields. To do this, some ion-field strength distribution, W(F), must be used. In the last part of this chapter, the effect of using various different distributions will be discussed. Hence, C(t) may be written as

$$C(t)_{\text{electrons}} = C(t, F)$$

Here, all the electrons have been accounted for as a function of the ion-field F. Then averaging over all ion-fields gives

$$C(t)_{\text{electrons + ions}} = \int d\,F\,W(F)\;\; C(t, F)$$

C(t) depends on F through the Stark effect. The unperturbed energy levels of the emitter are shifted by the ion-field. Therefore, we can write the Hamiltonian of the emitter as a function of F and proceed to find the contribution of the electrons to C(t).

Before dealing with the electrons, it is worthwhile considering two important effects of the ion-field. First, the Stark effect produces only a shift in the line.

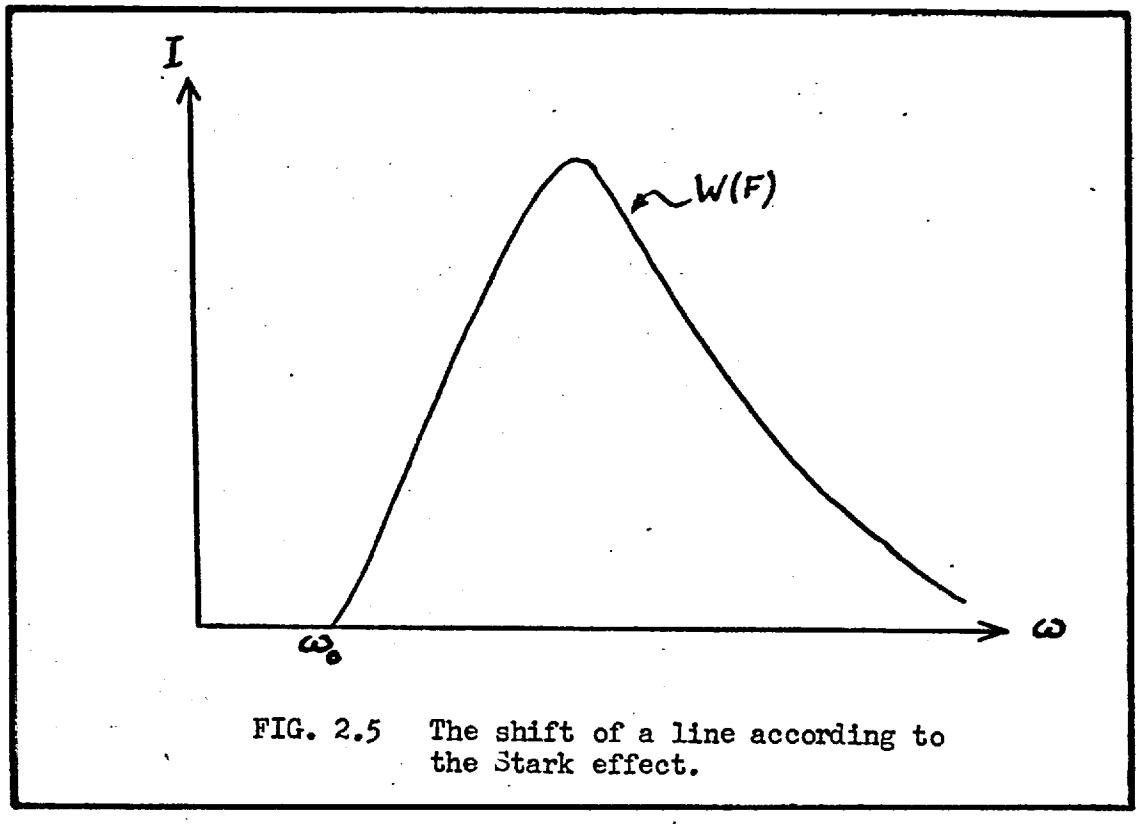

FIG. 2.5 The shift of a line according to the Stark effect.

Fig. 2.5 shows the shift of the centre of the line as a function the field strength, F, for an ion-field distribution W(F). At any given time, all possible values of F exist somewhere in the plasma and hence a broadening of the line is observed. The difference between an ion broadened line and a collision broadened line is that the ions shift the line centre, assymetrically, in one direction only whereas collisions smear the line out equally on both sides of the unperturbed frequency, ω_o .

The second important point is the production of 'forbidden' lines. The ion-field can mix the wave functions of two close

lying atomic energy levels so that the parity selection rule is broken down. If the atomic states α , α' and β are such that $\alpha\beta$ is an allowed transition, ($\Delta\ell = 1$) and $\alpha'\beta$ is forbidden ($\Delta\ell = 2$) then if $\omega_{\alpha\alpha'} \lesssim \Delta\omega_{\alpha\beta}$ (the width of the allowed line) the states α and α' are mixed strongly by the ion-field, and the transition $\alpha'\beta$ may occur. The strength of the forbidden line depends on the field strength. As F increases, the forbidden line becomes stronger but also shifts away from the allowed line. Fig. 2.6 shows the development of a forbidden line with increasing mean field strength.

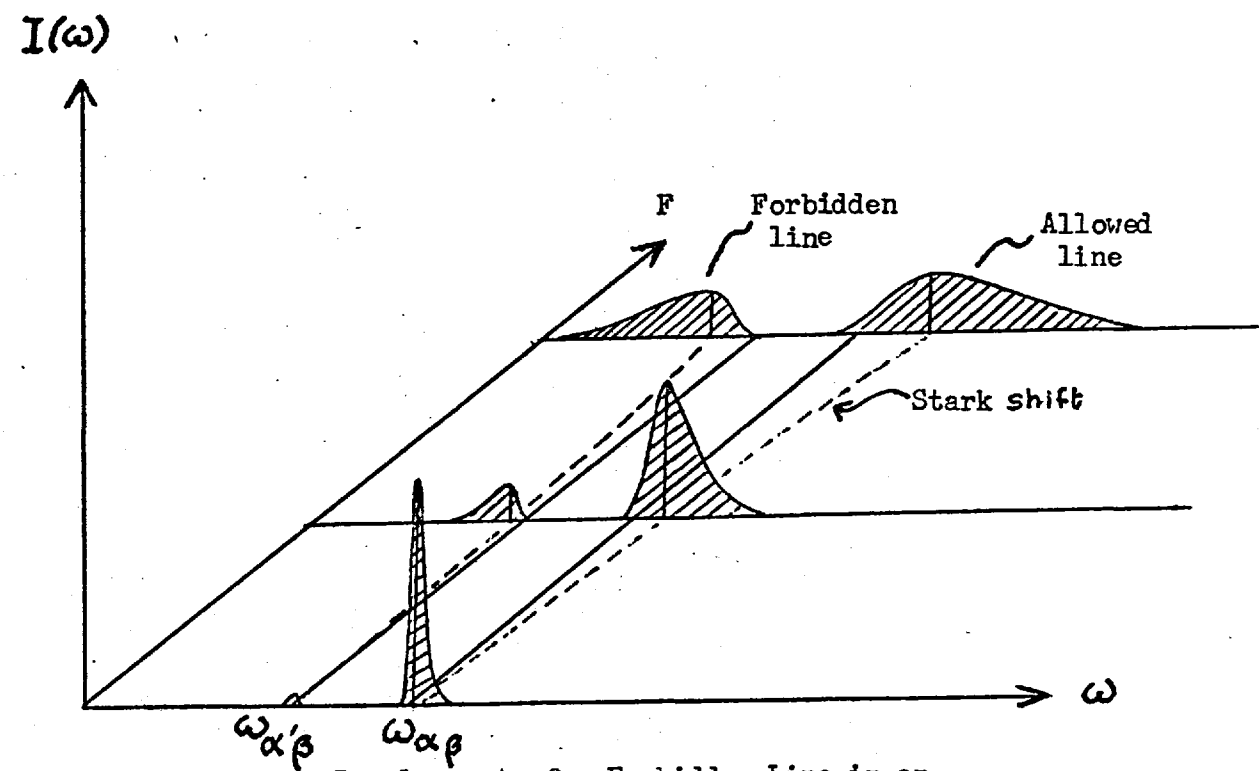

FIG. 2.6 Development of a Forbidden Line in an Ion Micro Field F.

Only the ion broadening is shown above. Note that there is no intensity, due to ions, in the central region between the two peaks. The ions can only shift the intensity out towards the wings of the line. As F increases, mixing between the upper states of the allowed and forbidden lines saturates and the forbidden line reaches a peak intensity equal to the intensity of the allowed line.

THE IMPACT APPROXIMATION

The essential feature of the impact approximation is that the electron collision time, τ , is usually short compared with times of interest in C(t). Expressed in terms of the line shape, this condition is, $\Delta\omega \ll \tau^{-1}$. To understand the impact approximation, it is useful to consider what can happen to the emitter in a collision. Basically, there are four types of collisional processes which can occur. Weak, strong, elastic and inelastic.

1. Weak Collisions

   The assumption here is that the probable effect of a collision on the emitter is small. The effects of a collision can then be expanded by perturbation theory. It is essential that

this can be done because weak collisions tend to be long range collisions and therefore overlap in time. By taking only the first non-vanishing order of the perturbation expansion, the time overlap of several collisions is removed and the effect of many weak collisions add scalarly. Baranger (1962) deals with this point fully.

2. Strong Collisions

Perturbers can come sufficiently close to the emitter that the perturber-emitter interaction is too large to be treated by perturbation theory. The effect of such a collision is to completely disrupt the wave train and the line is broadened by an amount proportional to the collision frequency. (See Lorentz Theory 1906.) These strong collisions do not occur very often if the impact approximation is to be valid; i.e. in making the impact approximation, it is assumed that the auto-correlation function does not change very much in a typical collision time. Hence, because strong collisions are infrequent and last only a short time, they do not overlap in time and, again, their effects add scalarly.

3. Elastic Collisions

This is simply a collision which does not change the atomic state of the emitter, i.e. only a phase change occurs.

4. Inelastic Collisions

Here, atomic transitions are induced by a collision. We distinguish between two different possible cases with reference to Fig. 2.7.

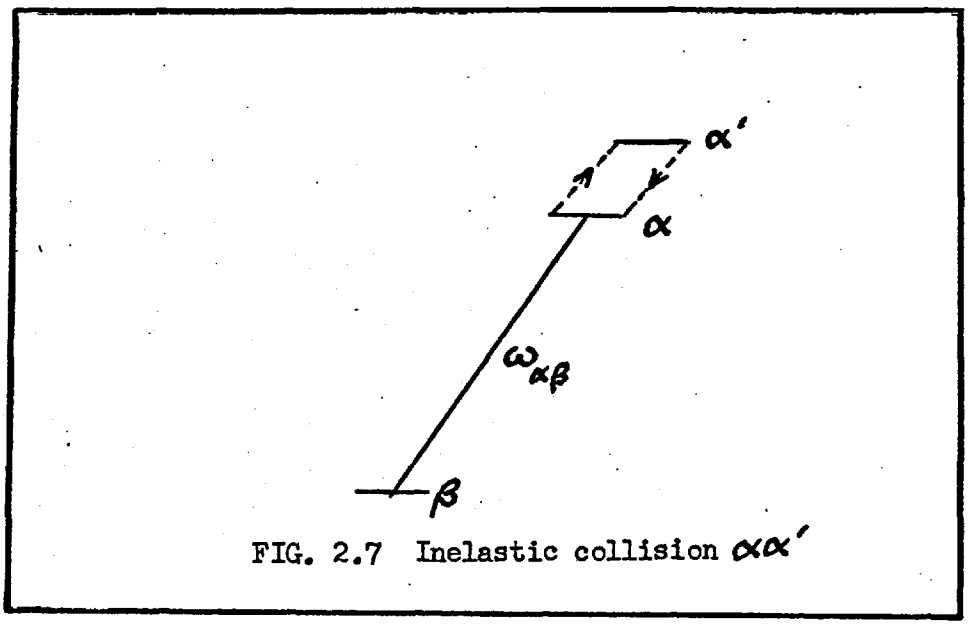

FIG. 2.7 Inelastic collision $\alpha\alpha'$

The emitter is radiating at a frequency $\omega_{\alpha\beta}$ and α' is a state lying close to α . Then a collision can cause the emitter to undergo the transition $\alpha\alpha'$ which terminates the radiation $\omega_{\alpha\beta}$. However, a subsequent collision can induce the transition $\alpha'\alpha$ and the radiation $\omega_{\alpha\beta}$ commences again. If the time interval

between the wave trains is large, then all memory of the phase between the wave trains is lost and a broadening of the line occurs. But if the interval is small, some correlation remains between the wave trains and a shift in the line is also induced. The latter is more probable when $\omega_{\alpha\alpha'} \sim \Delta\omega$, which is just the condition for overlapping lines.

MATHEMATICAL TREATMENT

Mathematically, the treatment of electron impact broadening can be reduced to finding the matrix elements of the electron broadening operator Φ. (See Griem 1964) C(t) can be written in terms of Φ :-

$$C(t) = d_\alpha \langle \alpha | \exp\left[-\frac{iH_a t}{\hbar} + \Phi_\alpha t\right] | \alpha' \rangle d^*_{\alpha'} \quad 2.12$$

H_a is the Hamiltonian of the emitter upper state a, d the dipole moment operator and α, α' the substates of a. Φ is given by

$$\Phi_a = \left\{ -\frac{i}{\hbar}\int_{-\infty}^{\infty} ds\, V'(s) + \left(\frac{i}{\hbar}\right)^2 \int_{-\infty}^{\infty} ds_1 V'(s_1) \int_{-\infty}^{s_1} ds_2 V'(s_2) \right.$$

2.13.

Here $V'(s)$ is given by

$$V'(s) = \exp\left[\frac{iH_A s}{\hbar}\right] V_{cl}(s) \exp\left[-\frac{iH_A s}{\hbar}\right]$$

H_A is the atomic Hamiltonian, $V_{cl}(s)$ is the classical perturber–emitter potential. Eq. 2.13 refers to a single electron collision. An essential feature of the impact approximation is that the average effect of the collision can be calculated and the average can then be multiplied by n_e, the electron density, to find the total effect. This averaging process reduces to evaluating:

$$\Phi \simeq -n_e \left(\frac{\hbar}{m}\right)^2 \int d\nu \, \mathrm{Re}_{cl}\left[\int_{-\infty}^{\infty} V_{cl}(s_1)\, ds_1 \int_{-\infty}^{s_1} V_{cl}(s_2)\, ds_2 + \cdots\cdots\right] \qquad 2.14$$

where

$$\int d\nu \equiv \iint dv\, d\rho\, 2\pi\rho v f(v) \qquad 2.15$$

Note that the first order term of eq. 2.13 has vanished in taking the angular average. Griem (1964) and Burgess (1968), among others, have both discussed this term. ρ and v are the electron impact parameter and velocity respectively and $f(v)$ is the electron velocity distribution, typically Maxwell. The integral over ρ has to be cut off at upper and lower limits. The upper limit, ρ_{max}, takes into account electron correlations. That is the field of electrons, whose impact parameter $> \rho_{max}$,

is shielded from the emitter by other, intervening, electrons. A lower limit, ρ min, takes into account strong collisions Electrons with $\rho < \rho_{min}$ are assumed to produce strong collisions and for these, some correction term is added to Φ . Strong collisions contribute, typically, about 20% of the total line width and hence errors in estimating ρ_{min} are not very important.

Finally, the line profile is obtained from the Fourrier transform of C(t) after an average over the ion-field has been taken

$$L(\omega) = \frac{1}{\pi} \int dF\, W(F) \Re \sum_{\alpha} d_{\alpha} \langle \alpha | [i\omega - \frac{iH_a(F)}{\hbar} - \Phi]^{-1} | \alpha' \rangle d^{*}_{\alpha'} \quad 2.16$$

THE ION MICROFIELD

The ion field, in general, effects the line profile most in the line centre and in the wings. The line centre is ion dependent in two ways. First the shift of the peak is determined largely by the ion-field and secondly, in the case of a hydrogenic line, the atomic energy levels are split and shifted in opposite directions leading to a dip or a pronounced peak in the line centre. In the wings, it is again necessary to distinguish between the hydrogenic and non-hydrogenic cases. In the former, where there

are components of the line shifted in both directions, the intensity of both wings is dominated by strong ion-fields. That is, the wings are produced by shifts in the line components due to the ion-field. For the non-hydrogenic case, only one wing, the wing to which the line is shifted, will be affected in this way.

The intermediate region, between the centre and the wings is usually dominated by electron broadening.

Calculations of the ion-field distribution, W(F), have been made in various approximations. The simplest of these is the nearest neighbour field

THE NEAREST NEIGHBOUR FIELD

Here, the ion-field is assumed to be due to the nearest ion only. This approximation will represent the true field only in the high field tail of W(F) where the field is due to a single ion coming close to the emitter. Hence accuracy can be expected only in the line wings (or one wing for a non-hydrogenic line) using this model.

The method of calculating W(F) on the nearest neighbour model is as follows. P(r) is the probability of finding an ion within a radius r. Then the probability of there being no ion is $P_-(r)$, and $P(r) + P_-(r) = 1$.

$$P_-(r)dr = P_-(r)[1-4\pi^2r^2Ndr-(\cdots)^2-\cdots\cdots] \qquad 2.17$$

The second term on the RHS of **2.17.** is the probability of there being one ion between r and r + dr, the third term, two ions etc. Then, ignoring high order terms gives,

$$dP_-(r) = -P_-(r)4\pi Nr^2dr$$

$$\therefore P_-(r) = \text{const. } exp[-\tfrac{4}{3}\pi Nr^3]$$

$$\therefore dP(r) = 4\pi Nr^2 exp[-\tfrac{4}{3}\pi Nr^3]dr \qquad 2.18$$

THE HOLTSMARK FIELD

The nearest neighbour model solves the problems of calculating the probability distribution of the ions, and then vectorially summing their fields, by ignoring them. Holtsmark (1919) was the first to attempt the solution. The physical assumption he made in calculating the probability distribution of the ions was that they moved independently of each other. That is, the interactions between the ions and electrons did not affect the paths along which they moved.

The field strength distribution is calculated in a similar manner to the nearest neighbour model. The difference is that the analysis leading to equation 2.18 must be performed in a 3N dimensional configuration space and the total ion-field is then, $F = |\Sigma_i F_i|$. This gives

$$dP(F) = W(\beta)\,d\beta$$

where

$$\beta = F/F_0 \; ; \quad F = e/r^2 \; ; \quad F_0 = e/r_0^2$$

and

$$W(\beta) = \tfrac{4}{3}\pi\beta^2[1 - 0.463 + 0.1227\beta^{-4} + \ldots]$$

or $$W(\beta) = 1.496\beta^{-5/2}[1 + 5.107\beta^{-3/2} + 14.9\beta^{-3} \ldots] \quad 2.19$$

(see Marganau and Lewis 1959)

The first of these applies when β is small and the other when β is large.

The assumption of no perturber - perturber interaction has to be investigated. This assumption is equivalent to saying that the thermal energies of the perturbers was much greater than their electrostatic interaction energies.

i.e. $$kT \gg e^2/r \qquad 2.20$$

The criterion for this to be true can also be expressed in terms of the parameter α

$$\alpha = r_0/r_D \qquad 2.21$$

Here r_0 is the mean interparticle distance, $\frac{4}{3}\pi r_0^3 n_e \sim 1$ and r_D is the Debye radius, $r_D = \left[\frac{kT}{4\pi N e^2}\right]^{1/2}$.

Then in the limit as $\alpha \rightarrow 0$, corrections due to interparticle interactions are negligible. The usefulness of the Holstmark distribution depends on what values the parameter α has in typical laboratory plasmas. α may be rewritten,

$$\alpha \sim (kT)^{-1/2} N^{1/6} \qquad 2.22$$

It is a very slow function of N and fairly slow with T. In the plasma to be described later, $\alpha = 0.3$, $n_e = 10^{15}$. For plasmas with $n_e \sim 10^{17}$, α can approach unity. It is therefore essential to investigate the effect of interparticle correlations on the ion distribution.

THE DEBYE-HÜCKEL POTENTIAL

One of the earliest interparticle correlation effects to be considered was the shielding of the ion-field by electrons. Because of the high electron velocity compared with the ion velocity, times long enough can be found such that all possible distributions of electrons round an ion occur, but short enough that the ion does not appreciably move. In this way, the field from a single ion is modified, or shielded, by a cloud of electrons which counteract the ion-field. The result is the Debye-Hückel potential (1923).

$$V = \frac{e}{r} \cdot e^{-r/r_D} \qquad 2.22$$

Ecker (1957) has numerically calculated Holtsmark Profiles modified by the Debye-Hückel potential. A simplified version of the potential was used.

$$V = \begin{cases} e^2/r & \dots\ r < r_D \\ 0 & \dots\ r \geq r_D \end{cases}$$

Fig. 2.8 shows his results for several values of the parameter δ defined by

$$\delta = \frac{4\pi r_D^3}{3} N \qquad 2.23$$

Note that $\delta \sim \alpha^{-1}$ and hence the Holtsmark curve corresponds to $\delta \to \infty$

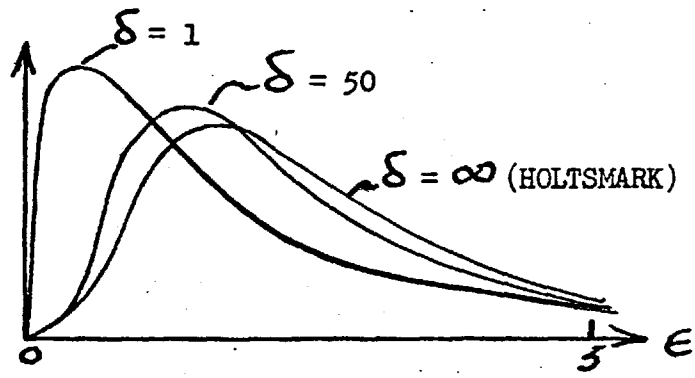

FIG. 2.8 The Ion Field calculated by Ecker.

It can be seen from Fig. 2.8 that perturber correlations may be very important.

THE MOZER-BARANGER FIELD

Ecker's calculations have accounted for electron shielding effects but ignore ion - ion interactions. Mozer and Baranger (1959) have put in these interactions. This is done by calculating first a distribution where there are no interactions and then adding onto it a series of corrections accounting for interactions. The probability of a given distribution can then be expressed by an equation of the form

$$
\begin{aligned}
V^M P_M(x_1 \ldots x_M) = {} & \prod g_1(x_i) + \Sigma_2 g_2(x_j, x_k) \prod g_1(x_i) \\
& + \Sigma_{22} g_2(x_j, x_k) g_2(x_l, x_m) \prod g_1(x_i) + \Sigma_{222} \ldots + \ldots \\
& + \Sigma_3 g_3(x_j, x_k, x_l) \prod g_1(x_i) + \Sigma_{33} \ldots + \ldots \\
& + \Sigma_{32} g_3(x_j, x_k + x_l) g_2(x_m, x_n) \prod g_1(x_i) + \ldots \\
& + \Sigma_4 \ldots + \\
& + \ldots \ldots
\end{aligned}
\qquad 2.24
$$

Some detailed consideration of eq.2.24 is necessary. First, the LHS. $P_M(x_1 \ldots x_M)$ is just the probability of finding particle 1 at position x_1 etc. and V^M is a normalising factor to express the probability per unit volume. On the RHS, the first term, $\prod g_1(x_i)$ where the product is taken over the

particles 1...M, is the no perturber interaction case. The second term is a correction term which accounts for the interactions between the particles j and k. This term, then, slightly changes the probability that particle j is in position x_j because of the interactions $\Sigma_k jk$. The $\Pi_i g_i(x_i)$ multiplies the second term by the probability that the particles $\sum_{1 \le i \ne j \le m} i$ were in their respective positions in the first place. Fig. 2.9 illustrates this.

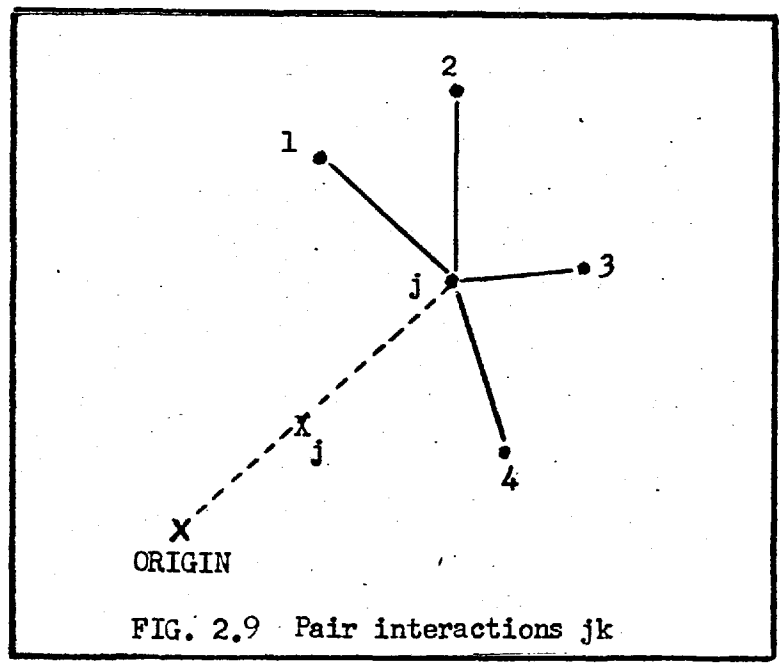

FIG. 2.9 Pair interactions jk

The probability that particle j is at x_j $[= P(x_j)]$ is modified by the interactions $\sum_k jk \prod_{i \ne j} P(x_i)$. The interactions are taken one at a time so that the correction to, say the j th

particle is made without any corrections to the remaining particles. The next term in eq. 2.24 considers two pairs of particles interacting in different parts of the plasma at the same time. That is, instead of accounting for all particles other than j and k in $\Pi_i g_1(i)$, another pair, l and m, are removed from the product and assumed to be interacting. This results in a term of the form

$$\Sigma_{22}\, g_2(x_j, x_k)\, g_2(x_l, x_m) \Pi g_1(x_i)$$

By removing more and more pairs the terms such as $\Sigma_{222\cdots}$ etc, are arrived at. Note that the $\Pi_i g_1(x_i)$ includes only those particles not already explicitly included in the Σ terms.

Each successive term in eq. 2.24 adds on a correction to the previous term. The third term, for instance, corrects the position of the k th particle by taking the kl interaction before correcting the j th particle with the jk interaction. Clearly, this term is important only when three particles come close together.

Mozer and Baranger (MB) now assume that the first correction, the pairwise interactions, are small. Hence, the subsequent corrections are even smaller and may be ignored.

The field distribution itself is calculated via its Fourier transform, F(k).

$$F(k) = \int \exp(ik\cdot E) W(E) dE$$

$$= \int \exp[ik\cdot(E_1 + \dots E_M)] P(x_1 \dots x_M) d^3x_1 \dots d^3x_M \quad 2.25$$

The exponential terms are then written

$$\exp(ik\cdot E_1) = 1 + \theta_1 \quad etc.$$

After some manipulation, the following equation is reached

$$F(k) = \exp\left[\sum_{p=1}^{\infty} (n^p/p!)\, h_p(k)\right] \quad 2.26$$

where

$$h_p(k) = \int \theta_1 \dots \theta_p g_p(x_1 \dots x_p) d^3x_1 \dots d^3x_p \quad 2.27$$

and

$$W(E) = (2\pi)^{-3} \int \exp(-ik\cdot E) F(k) d^3k$$

MB take only the first two terms of eq. 2.26 The first term gives the Holtsmark field at a neutral point and the second term the first order correction to it. The Debye-Hückel shielded field is used to calculate the pair-correlation term.

$$P_2(x_1, x_2) = V^{-2} \exp(-e^2\phi_{12}/kT)$$

$$\phi_{12} = |x_1 - x|^{-1} \exp(-|x_1 - x_2|/r_D')$$

and

$$g_2(x_1, x_2) = \exp(-e^2\phi_{12}/kT) - 1 \qquad 2.28$$

Eq. 2.28 is then linearised to give

$$g_2(x_1, x_2) = -e^2\phi_{12}/kT$$

$$h_2(k) = -(e^2/kT)\iint \theta_1 \theta_2 \phi_{12}\, d^3x_1\, d^3x_2$$

Note that r_D is replaced by $r_D' = r_D/\sqrt{2}$. This accounts for the fact that the ion-field is shielded not only by electrons but also by other ions.

A similar treatment can be used to calculate the field at a charged point. A further correlation now enters each term because of the interaction between the origin and the ion. Hence $g_1(x)$ instead of being unity, becomes

$$g_1(x) = \exp\left[-\frac{e^2}{rkT} \cdot \exp(-r/r_D')\right]$$

A correction must also be made to $g_2(x_1, x_2)$ but as this would be a three body correction, it is omitted and g_2 remains unchanged.

Figs. 2.10 - 2.11 show the distribution obtained by MB compared with Holtsmark for several values of α.

HOOPER'S CALCULATIONS

Using the same physical basis, Hooper (1968) calculated ion-field distributions. His mathematical treatment is more sophisticated than MB and enable him to account for higher order correlations. As Hooper uses essentially the same physics as MB, only the mathematics being different, a description of his calculation will not be given here. However, he has performed a Monte Carlo calculation for W(F) and compared it with his results and those of MB. These are shown in Figs. 2.10 - 2.12.

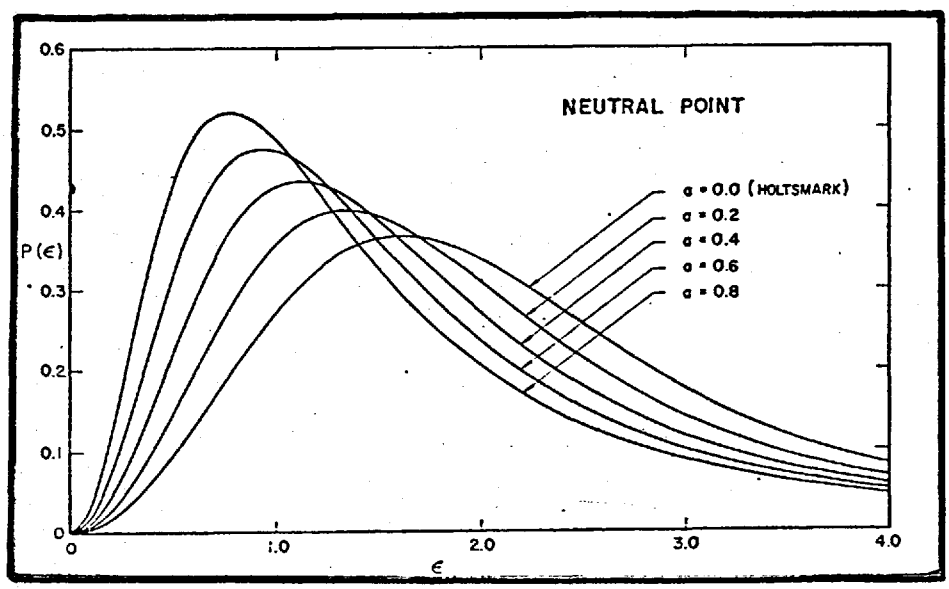

FIG. 2.10 Hoopers Calculations of W(F) for various values of α.

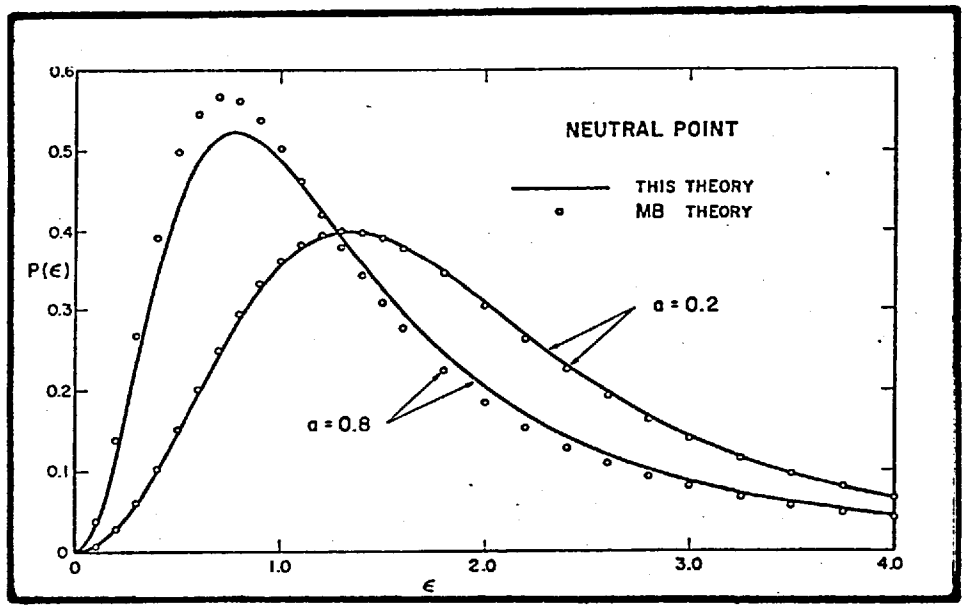

FIG. 2.11 Comparison of Hooper and MB for α = 0.8, 0.2.

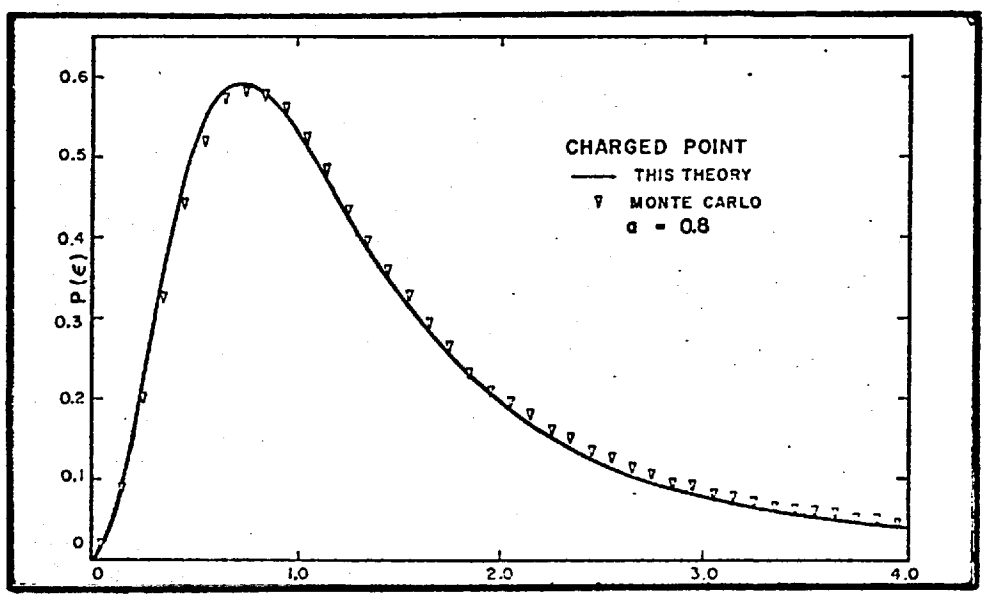

FIG. 2.12 Comparison of Hooper with Monte Carlo computations for α = 0.8.

Figs. 2.10 - 2.12 are taken from Hooper (1968). His notation is different from that used earlier in this chapter.

$$\epsilon = \beta = F/F_0$$

Two points emerge from a study of the various ion-fields. First, Fig. 2.12 shows the very good agreement between Hooper and the Monte Carlo computation for $\alpha = 0.8$. At this value, particle correlations are important, as can be seen by comparison with the Holtsmark result. This agreement is a good indication that Hooper's curves are accurate for high values of α. Secondly, Fig. 2.11 shows that for low values of α, Hooper and MB agree exactly and even at high α, the discrepancy between the two is very small except at the peak of the curve where disagreement is about 10%. In the present experiment, $\alpha = \cdot 3$ which is in the region of complete agreement between Hooper and MB. Hence, the errors incurred in the line profile calculations of Griem and BCS, both of whom use Hooper's field, due to an incorrect ion-field distribution can be dismissed as negligible.

CHAPTER 3

A COMPARISON OF THE CALCULATIONS OF BCS AND GRIEM

As we have seen, the problem of calculating line profiles divides into two sections. First, the ion broadening is treated by the quasi-static approximation and then the electron broadening by the impact approximation. The ion broadening presents relatively little difficulty and so will be dealt with first.

ION BROADENING

Both Griem and BCS make the same basic approximations, that

(a) lower state broadening is negligible,

(b) the singlet and triplet systems can be treated separately,

(c) only levels with principal quantum number $n = 4$ need be considered.

The problem, then, is to calculate the energy levels of the upper state in the presence of an ion-field.

BCS use the full perturbation theory to do this. They calculate the dipole matrix elements $\langle P|d|D\rangle$, $\langle D|d|F\rangle$, [P = 4 P level, etc.] over the whole range of ion-field strengths using the Coulomb approximation. Note that over the range of n_e considered, the Stark effect changes from quadratic at low densities to linear at high densities. Griem makes an approximation at this stage. Because of the large splitting of P-D states compared with the D-F states $[\omega_{PD}/\omega_{DF} \simeq 30]$ he uses the perturbation theory only for the D and F levels. The P level is considered separately and assumed to follow the quadratic Stark effect only. This is true for $n_e \leq 10^{16}$ but for higher values linear Stark effect must be used. When $n_e < 10^{16}$, Griem uses the profiles of Gieske (1968). Furthermore, Griem determines the elements $\langle D|d|F\rangle$ by using hydrogen radial matrix elements. All the above approximations are well verified and do not introduce significant errors into the calculations.

Finally, the integration over the ion-field distribution is performed. The distribution functions of Hooper (1968) are used by both Griem and BCS and again, these can be relied upon to a high degree of accuracy.

ELECTRON BROADENING

The line shape, L(W) is given by

$$L(\omega) = -\frac{1}{\pi}\int dF\, W(F)\, \mathcal{R} \sum_{\alpha\alpha'\beta} \langle\alpha|d|\beta\rangle\langle\alpha'|d|\beta\rangle$$

$$\times \langle\alpha|[i(\omega-\omega_{\alpha\beta}) + \Phi]^{-1}|\alpha'\rangle \qquad 3.1$$

It is the last part of 3.1 which concerns the electron broadening, in particular the electron broadening operator. Φ . As explained in Chapter 2, Φ is calculated by perturbation theory to second order.

$$\Phi_{\alpha\alpha'} = -\left(\frac{n_e}{\hbar^2}\right) \sum_{\alpha''} \int_{-\infty}^{\infty} dt \int_{-\infty}^{t} dt'.\, exp[i(\omega_{\alpha\alpha'}t - \omega_{\alpha'\alpha''}t')]$$

$$\times [\langle\alpha|V(t)|\alpha''\rangle\langle\alpha''|V(t)|\alpha'\rangle \qquad 3.2$$

$$V(t) = \frac{ed\cdot(\rho+vt)}{(\rho^2+v^2t^2)^{3/2}} \qquad 3.3$$

The square brackets in 3.2 imply an average over electron impact parameters and electron velocities.

$$[\cdots] = \int_0^{\infty} 2\pi\rho\, d\rho \int_0^{\infty} f(v)\, dv \qquad 3.4$$

We have seen that the essential difference between the theory for isolated lines and overlapping lines is that in the

latter case some correlation in the emitted wave remains even after the emitter changes its state to the nearby upper state. Fig. 3.1 shows the relevant term diagram for the lines 4471 and 4922 of He I.

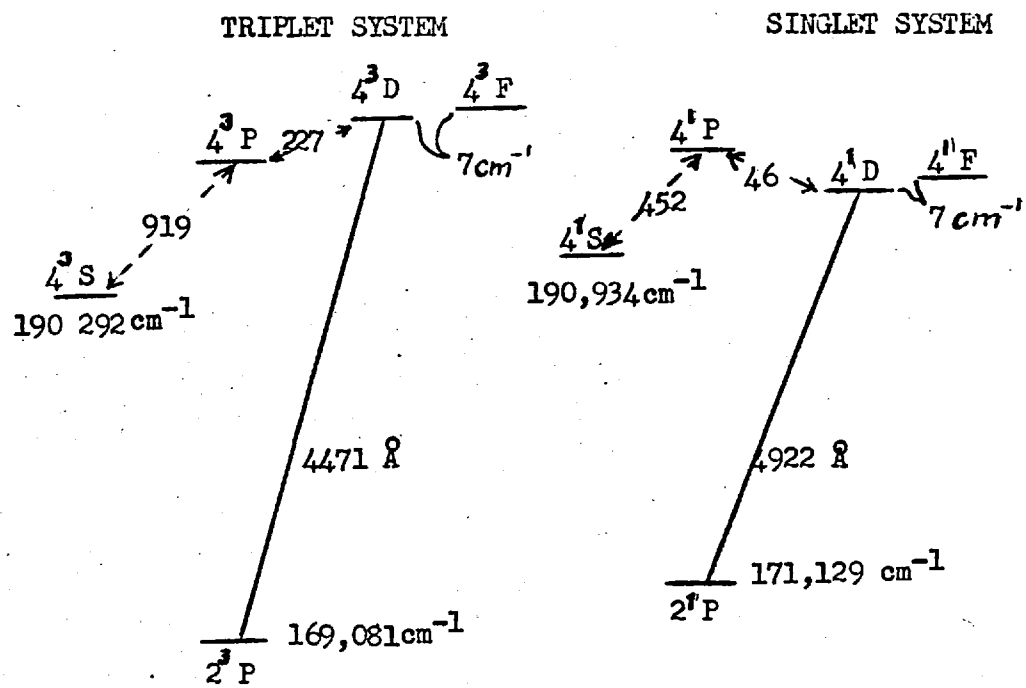

FIG. 3.1 Term diagrams of Helium I 4471 and 4922. The 2P and 4S levels are given in cms^{-1}. The other figures are energy differences in cms^{-1} between neighbouring levels.

Referring to the triplet system only, there are two lines which can overlap $4^3D - 2^3P$. These are $4^3F - 2^3P$ and $4^3P - 2^3P$. However, because of the relatively large splitting between $4^3P, - 4^3D$ levels, the latter line remains isolated until $n_e > 10^{17}$ but the first line must be considered at least partially overlapping when $n_e > 10^{14}$

The overlapping lines are accounted for in the theory by considering off-diagonal elements of the last matrix in eq. 3.2. That is, the following elements must be calculated

$$\sum_{\alpha''} \langle D|V(t)|\alpha''\rangle\langle\alpha''|V(t)|F\rangle \qquad 3.5$$

$$\sum_{\alpha''} \langle D|V(t)|\alpha''\rangle\langle\alpha''|V(t)|P\rangle \qquad 3.6$$

BCS carry out these calculations but Griem ignores the term 3.6. This, however, does not effect his results because the P level overlaps only at densities in excess of 10^{17} when his approximations concerning ion-broadening are invalid anyway and he uses Gieske's results.

The profiles obtained are then averaged over the magnetic substates and fine structure splitting of the lower level in both sets of calculations.

It now remains only to calculate the angular average in eq. 3.2. This is done by rewriting 3.2 in the form

$$\Phi_{\alpha\alpha'} = \frac{4\pi n_e}{3}\left(\frac{e}{\hbar}\right)^2 \sum_{\alpha''} \langle\alpha|d|\alpha''\rangle\langle\alpha''|d|\alpha'\rangle$$
$$\times \int dv\, f(v) v^{-1} \int d\rho\, \rho^{-1}\left[A(z,z') + iB(z,z')\right] \qquad 3.7$$

The functions A(Z, Z') and B(Z, Z') are generalisations of A(Z) and B(Z) defined and discussed by GBKO (1960)

$$z = \rho\omega_{\alpha\alpha''}/v$$

$$z' = \rho\omega_{\alpha'\alpha''}/v$$

The next step is to evaluate the integral over ρ of eq. 3.7. To do this, it is necessary to introduce upper and lower cut-offs, ρmax and ρmin. in ρ to account for long range electron correlations and strong collisions. The usual method of establishing ρmin. is to assume the field of one electron is unaffected and then shield the field of all the others. Hence, in expressions such as

$$\int dt \int dt'\, V(t) V(t')$$

one V(t) is shielded but not the other. The shielding is obtained by cutting off ρ at about the Debye radius.

$$\rho_{max} = 1.12\,\rho_D \qquad 3.8$$

This is the prodecure followed by Griem. BCS adopt the suggestion of Chappel et al (1969) and Burgess (1970) who maintain that both fields should be shielded. The value of ρmax is then reduced by a factor 1.65.

$$\rho_{max} = 0.682\,\rho_D \qquad 3.9$$

Strong collisions are, by definition, those collisions for which perturbation theory is not applicable. Hence we may write

$$|\langle\alpha|\,\Phi(\rho_{min})|\alpha\rangle| \simeq \tfrac{2}{3}\left[\frac{\hbar}{mv\rho_{min}}\right]^2 n^4 \simeq 1 \qquad 3.10$$

Estimates of the strong collision cut-off can be made from eq. 3.10. BCS use a more complicated version of eq. 3.10. They calculate a separate ρ min. for diagonal and off diagonal elements of Φ and then, because perturbation theory can be expected to break down at about the same ρ min. for all matrix elements, they finally take

$$\rho_{\alpha\alpha'}^{min} = MIN\left(\rho_{\alpha\alpha}^{min}\,;\,\rho_{\alpha'\alpha'}^{min}\,;\,\lambda\right) \qquad 3.11$$

$\lambda\!\!\!^{-}$ is the de Broglie wavelength and is used to prevent the divergence of the classical path approximation. BCS then account for strong collisions by adding the Lorentz-Weisskopf term, $\pi\left[(\rho_{\alpha\alpha}^{min})^2 - \lambda\!\!\!^{-2}\right]$ onto the elements of Φ.

Griems' treatment of the term

$$\int dv\, f(v) v^{-1} \int d\rho\, \rho^{-1} \left[A(z) + i B(z)\right]$$

differs appreciably from BCS. The integral is evaluated using the 'high temperature limit' approximation. Basically, this involves taking the limit of A(Z), B(Z) as $Z \to 0$.

$\lim_{z\to 0}\left[A(z); B(z)\right]$ = 1 and 0 respectively. (Note $Z = \frac{\rho\omega}{v}$).

The justification for this step is that not only does $z \to 0$ as $v \to \infty$ but also as $\omega \to 0$. This assumption can be checked for typical parameters of the plasma to be described in this thesis.

$$v \simeq 4.10^{7}\ cm.\ sec^{-1}$$
$$\rho \simeq n_e^{-1/3} \simeq 10^{-5}\ cm.$$
$$\omega \simeq 7\ cm^{-1}\ [4^3D - 4^3F]$$
$$\therefore\ z \simeq 5.10^{-2}$$

Comparison with the A and B functions, plotted against Z in GBKO, shows that the high temperature limit is indeed valid at

least for the 4^3 D – 4^3 F. Consideration of the 4^3 D – 4^3P proves otherwise. Now $\omega = 227 cm^{-1}$ and hence

$$z = 1.5$$
$$A(z) = 0.3$$
$$B(z) = 0.6$$

This invalidity does not in fact effect Griems results. He has already limited the range of his calculation to $n_e \leq 10^{16}$ and in this range, the influence of the 4^3P level is negligible anyway.

The integral over ρ introduces the functions a(Z), b (Z), defined by GBKO. With these, and the high temperature limit, eq. 3.2 becomes

$$\Phi = \Phi_{str.} - \frac{4\pi}{3}\left(\frac{\hbar}{m}\right)^2 n_e \int dv\, v^{-1} f(v) \sum_{\alpha'} \left| \frac{\langle \alpha | d | \alpha' \rangle}{a_o} \right|^2$$
$$\times \left[\ln\left(|z_{\alpha\alpha'}^{min}|^{-1} \right) \pm i\frac{\pi}{2} \right] \qquad 3.12$$

where

$$\ln |z_{\alpha\alpha'}^{min}|^{-1} = \lim_{z \to 0} [a(z)]$$
$$\pm i\frac{\pi}{2} = \lim_{z \to 0} [ib(z)]$$
$$a_o = \frac{\hbar^2}{me^2}$$
$$\Phi_{str.} = \text{term accounting for strong collisions}$$

In order to estimate Φ^{strong}, Griem assumes a similar criterion as BCS to obtain ρ min.

$$\rho_{min} \simeq \frac{\hbar}{mv} n^2 \qquad 3.13$$

Then, according to GBKO,

$$\Phi_{str.} \simeq -n_e \int dv f(v) \pi \rho_{min}^2(v)$$

$$\rightarrow 0 \text{ in the high temp. limit}$$

Griem does not put $\Phi^{\text{strong}} = 0$ but adds $\frac{1}{2}$ inside the square brackets of 3.12 to account for strong collisions.

Rather than integrate over the velocity distribution $f(v)$, Griem substitutes a Maxwell average $\bar{v}$

$$\frac{1}{2} m \bar{v}^2 = kT$$

Then, using eq. 3.13, he has

$$z_{min} = \frac{8\hbar\omega_{\alpha\alpha'}}{kT}$$

$$\Phi_{\alpha\alpha'} = -\frac{4\pi}{3}\left(\frac{\hbar}{m}\right)^2 n_e \sum_{\alpha'} |\langle\alpha|d|\alpha'\rangle|^2 \left[\frac{1}{2} + \ln\left(\frac{kT}{8\pi\omega_{\alpha\alpha'}}\right) \pm i\frac{\pi}{2}\right] \qquad 3.14$$

The imaginary term in 3.14 is dropped. This corresponds to neglecting the shift caused by electron impacts.

At this stage it is possible to explain more fully Griems' procedure for the weak collision cut-off. The cut-off actually occurs not in ρ but in $\omega_{\alpha\alpha}$ of eq. 3.14. In fact Griem uses three alternative cut-offs.

$$\omega_{\alpha\alpha'} = MAX.\left[|\omega_D - \omega_F|\ ,\ \omega_P\ ,\ |\omega - \tfrac{1}{2}(\omega_D + \omega_F)|\right]$$

These characteristic frequencies are the separation of the allowed and forbidden component, the electron plasma frequency and the separation from line centre. The first of these corresponds to neglecting the cut-off, the second to the Debye cut-off and the third to the Lewis (1961) cut-off. For the range of interest in the present work, it can be shown that

$$\omega_P \simeq 5.10^{11}\ sec^{-1}$$
$$(\omega_D - \omega_F) \simeq 2.10^{11}\ sec^{-1}$$
$$\omega - \tfrac{1}{2}(\omega_D + \omega_F) \simeq 0 - 10^{12}\ sec^{-1}$$

Hence, for most of the line profile the cut-off used is effectively the Debye radius. In the line wings, this switches to the Lewis cut-off, but since the wings are dominated by ion broadening, the profiles are not greatly effected.

In spite of the numerous approximations made by Griem, there is very little difference between the two calculations.

Griem estimates, for instance, that the combined errors due to the use of hydrogen radial matrix elements and the high temperature limit amount to about 10%. Variations in the treatment of strong collisions will also not produce a significant error as strong collisions contribute only about 20% of the broadening anyway.

The only fundamental difference is in the upper cut-off, ρ max. Griem is therefore overestimating the electron impact width compared to BCS. We can therefore expect the region between the two peaks in the profile to differ most. The reason for this is that this region is not effected by the ions and hence electrons only are contributing to the intensity of the dip between the peaks.

Fig.9.1 shows profiles of BCS and Griem superimposed. It can be seen that it is indeed in the dip and near the line centre that the two profiles differ from each other most. It is one of the aims of this work to attempt to compare Griem and BCS with experimental profiles. However in the range of electron densities ($10^{14} - 10^{15}$) in which the present experiment is performed, the differences between Griem and BCS are relatively small. It will be seen later in this thesis that much larger discrepancies between theory and experiment appear. A comparison of the accuracy of Griem and BCS is therefore impossible but the possibility of a

fundamental error in both theories has been suggested by Burgess (1970a). This aspect of the thesis will be discussed in a later chapter.

CHAPTER 4

DESCRIPTION OF APPARATUS

THE DISCHARGE

The work undertaken in this project was, to a certain extent, an extension of work carried out by Jenkins (1970). The apparatus used was therefore a copy, with minor modifications of the theta pinch pre-ioniser used by Jenkins at Imperial College. This consisted of a cylindrical pyrex tube with ring electrodes placed at each end thus enabling observations of the discharge to be made down the axis of the tube. A 1μF rapid discharge capacitor was connected in parallel to the electrodes and charged up to 20 kv. Continual breakdown of the gas in the discharge tube was prevented by a three pin spark gap which could be triggered externally.

Fig. 4.1 shows a schematic diagram of the discharge tube. Originally plain quartz windows were placed on the ends of the electrode assemblies, but these were later replaced by quartz inserts which effectively limited the length of the plasma column to be equal to the distance between the electrodes. The resistor, R, was approximately 3Ω and critically damped the discharge.

The gas supply system was continuously pumped by a rotary pump. A diffusion pump was also incorporated into the system so that the discharge tube could be evacuated to about 10^{-4} mm Hg before commencing a run. The operating gas pressure was measured on a McLeod gauge.

A survey spectrum of the discharge was obtained on a quartz prism spectograph. Fig. 4.2 shows the spectra at various gas filling pressures. The gas used was 99.995% pure helium and the spectra show that in the visible region there are very few impurity lines. The final operating pressure was chosen to be 0.5 mm.Hg At this pressure, the He I lines 4471 and 4922 are clearly visible and also the He II lines 4686 and 3203 can still just be seen. Note that at both higher and lower presence, the He II lines disappear. It was hoped that the pressure of He II lines would be helpful in later diagnostic measurements, though, in the event, this was not the case.

FIG 4.1.

SCHEMATIC DIAGRAM OF DISCHARGE TUBE

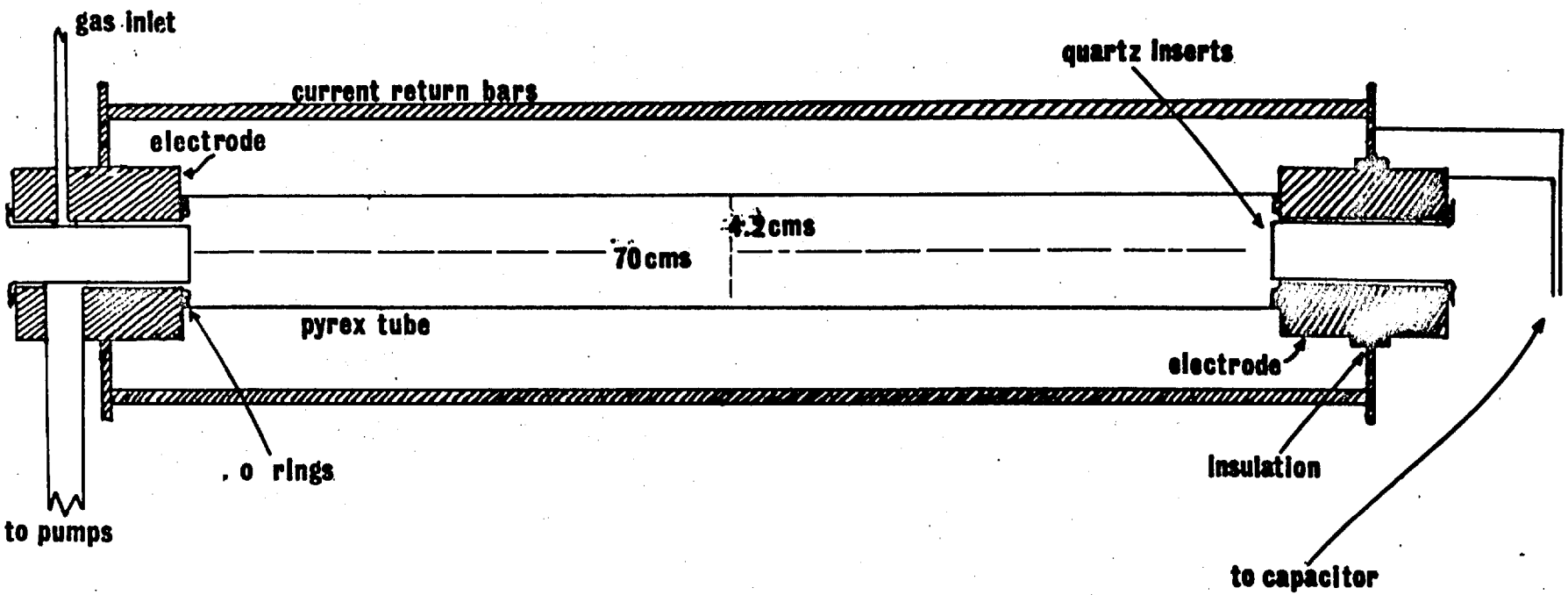

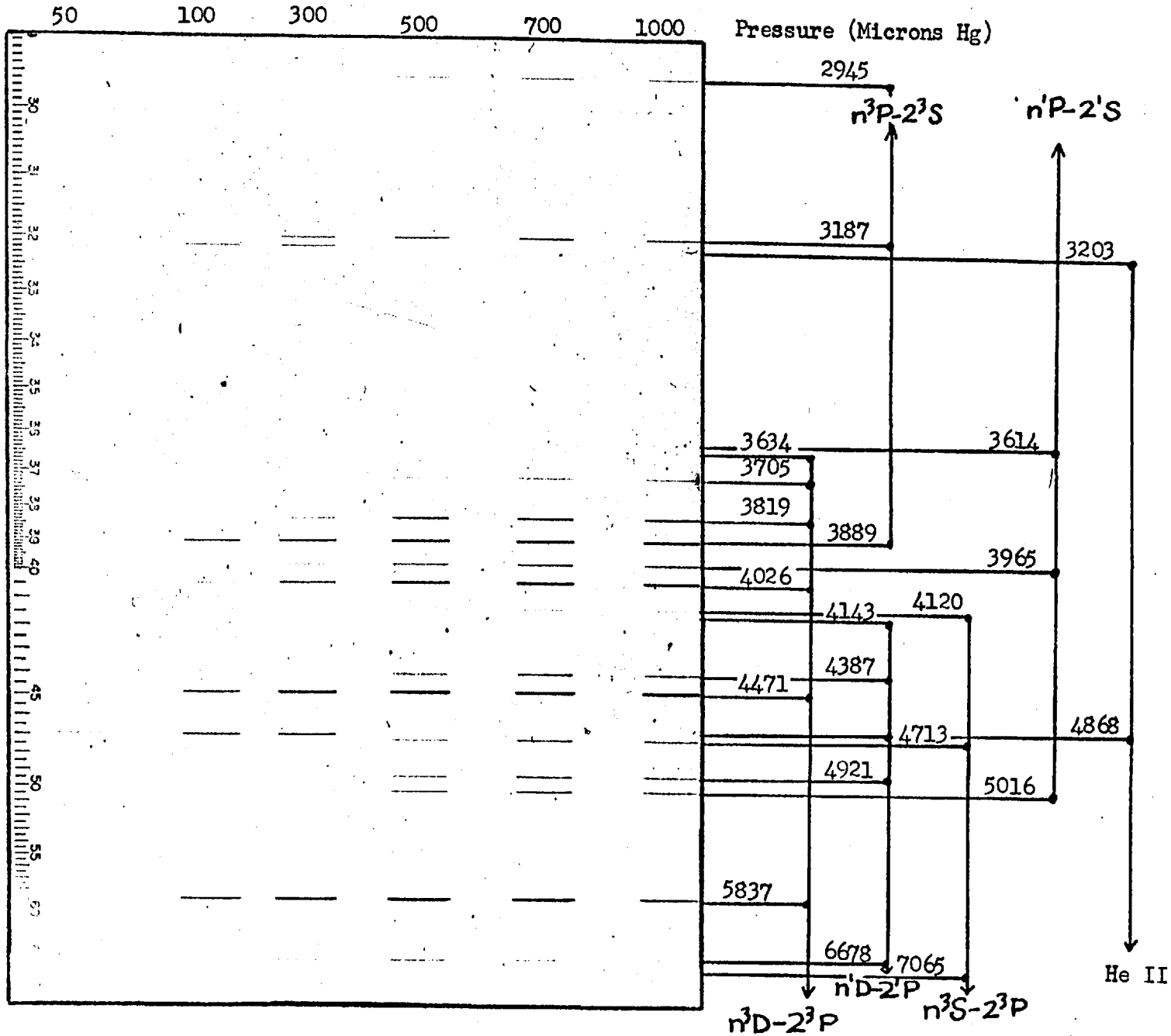

FIG. 4.2

Spectrum of discharge at various pressures

DETECTING EQUIPMENT

Line profiles were obtained photo-electrically. Light from the plasma was passed through a monochromator and into a photo-multiplier. The photo-multiplier output was then displayed on an CRT via an emitter follower and the CRT trace photographed on 35 mm film. In this way, a time history of a small wavelength section of the plasma was obtained and a line profile built up by scanning across the line on a shot to shot basis. Fig. 4.3 shows a block diagram of the whole apparatus. The discharge was triggered manually. A ~~Rogeski~~ Rogowski coil, wound round the discharge tube, was used to trigger the CRT and its output was also displayed on the CRT. This showed that current ceased to flow in the tube after about 5μS. The exact form and magnitude of the current is not important in the present experiment. Previous work by Jenkins (1970) has shown that in the early stages of the discharge $n_e \simeq 10^{16}$ and as, we are now interested in $n_e \simeq 10^{14}-10^{15}$, only later times, in the plasma afterglow, need be considered. However, the ~~Rogeski~~ Rogowski coil output provided a useful time reference signal. Throughout this thesis, all times are measured from the peak of the ~~Rogeski~~ Rogowski signal.

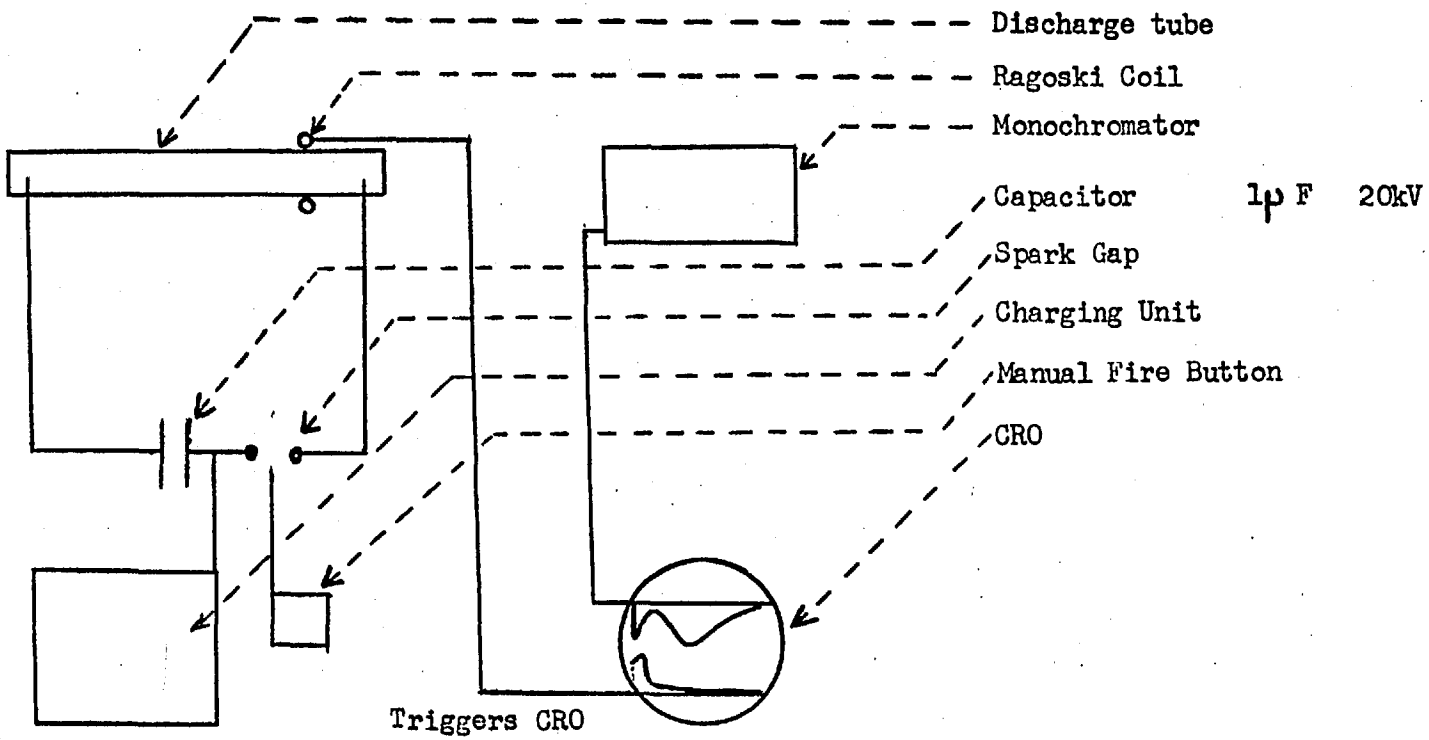

FIG. 4.3 Block Diagram of Apparatus

THE MONOCHROMATOR

A 'Monospek 1000' monochromator was used in the experiment. This was a Czerny-Turner instrument, the mirrors were 1 m focal length and the grating had 12,000 lines/cm blazed at 5,000 Å. The reciprocal dispersion was 8 Å / mm and the numerical aperture f/10. The manufacturers claim a resolving power based on the profile of the Hg doublet at 3132 Å and this profile was scanned to check that the instrument was correctly lined up. Then the instrument profile was obtained by scanning the narrow Hg line at 3125 Å and also the cadmium line at 4678Å using low pressure lamps in both cases. The instrument profiles obtained were approximately triangular with a whole-half width of 0.15 Å when both exit and entrance slits were 10μ wide.

One small modification was made to the monochromator. The mechanism for rotating the grating was far too coarse and therefore the drive was taken off one of the intermediate gears. This enabled the grating to be rotated in steps of 0.05 Å.

PHOTOMULTIPLIER AND EMITTER FOLLOWER

An EMI 1P28 photomultiplier was used to detect the light. An emitter follower was then placed directly on the back of the

photomultiplier. The reason for this was that it was not always physically possible to place the CRT near to the photomultiplier and therefore a long cable had to be used to connect the two. Thus a considerable capacitance was introduced into the circuit which adversely effected the integrating time of the detector-CRT system. An emitter-follower is basically a high input impedance low output impedance device. The integrating time is given by

$$\tau = R_i C_i$$

where R_i and C_i are the input resistance and capacitance of the emitter follower. By placing the emitter follower next to the photomultiplier C_i was kept to a minimum and hence the signal, which was proportional to R_i, was maximised for a given τ. Fig. 4.4 shows the circuit diagram of the emitter follower.

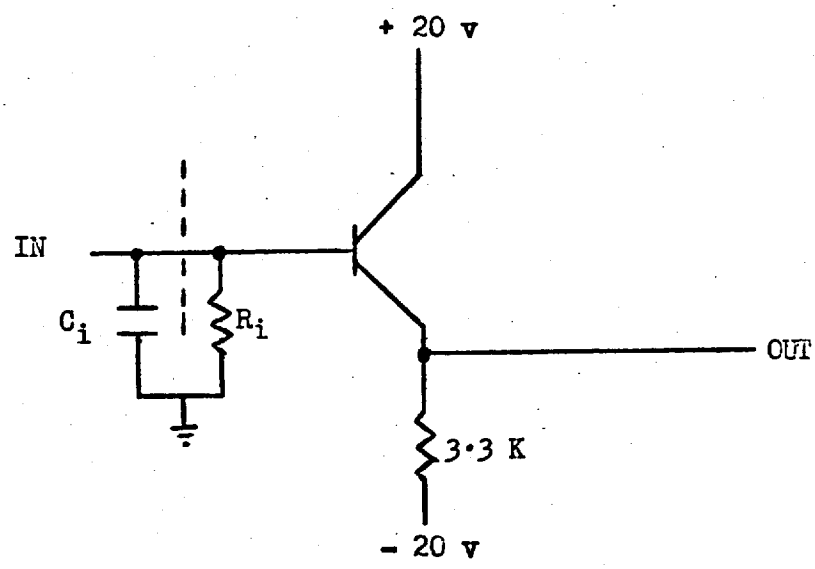

FIG. 4.4 Circuit Diagram of Emitter Follower

C_i was just the stray capacitance of the photomultiplier-emitter follower input system. R_i was adjustable. The choice of R_i and hence τ was important as clearly, a large integrating time would distort the line profiles. Hence an experiment was performed to determine a suitable value of τ.

A very fast light source was placed in front of the photomultiplier. This consisted simply of a length of co-axial cable continuously charged until it broke down across the free end. The time constant of the cable was a few nano-seconds. The response time of the emitter follower was then measured by displaying the emitter follower output on a CRT. Table 4.1 shows the response time for various values of R_i.

R_i	τ
1 K	25 nS
82 K	2 μS
220 K	4 "
470 K	10 "

Table 4.1 Integrating time, τ, for various input impedances, R_i, in the emitter follower

The first value of table 4.1, $\tau = 25nS$ was much faster than the plasma decay ($\sim 20\mu S$). Therefore, using this value guaranteed that an accurate profile was obtained. Using this profile as a standard, comparisons with the other input impedances were obtained. The results are shown in fig. 4.5. The curves are approximately normalised to each other and represent the total integrated line, 4471. For times $> 30\mu S$, the $\tau = 2\mu S$ curve follows the $\tau = 25nS$ curve very closely but it can be seen that when $\tau = 5\mu S$ the emitter follower is not able to match the true curve until about $60\mu S$. The effect of a long integrating time on the profile is relatively small because all points on the profile tend to be changed in the same way. However, the forbidden line falls off faster in time than the allowed line and hence it is important that these integrating errors do not occur. For all subsequent experimental work, R_i was 82 K giving an integrating time of $2\mu S$.

LINEARITY OF THE PHOTOMULTIPLIER, EMITTER FOLLOWER CRT SYSTEM

Fig. 4.6 shows the system used to check the linearity of the detecting system.

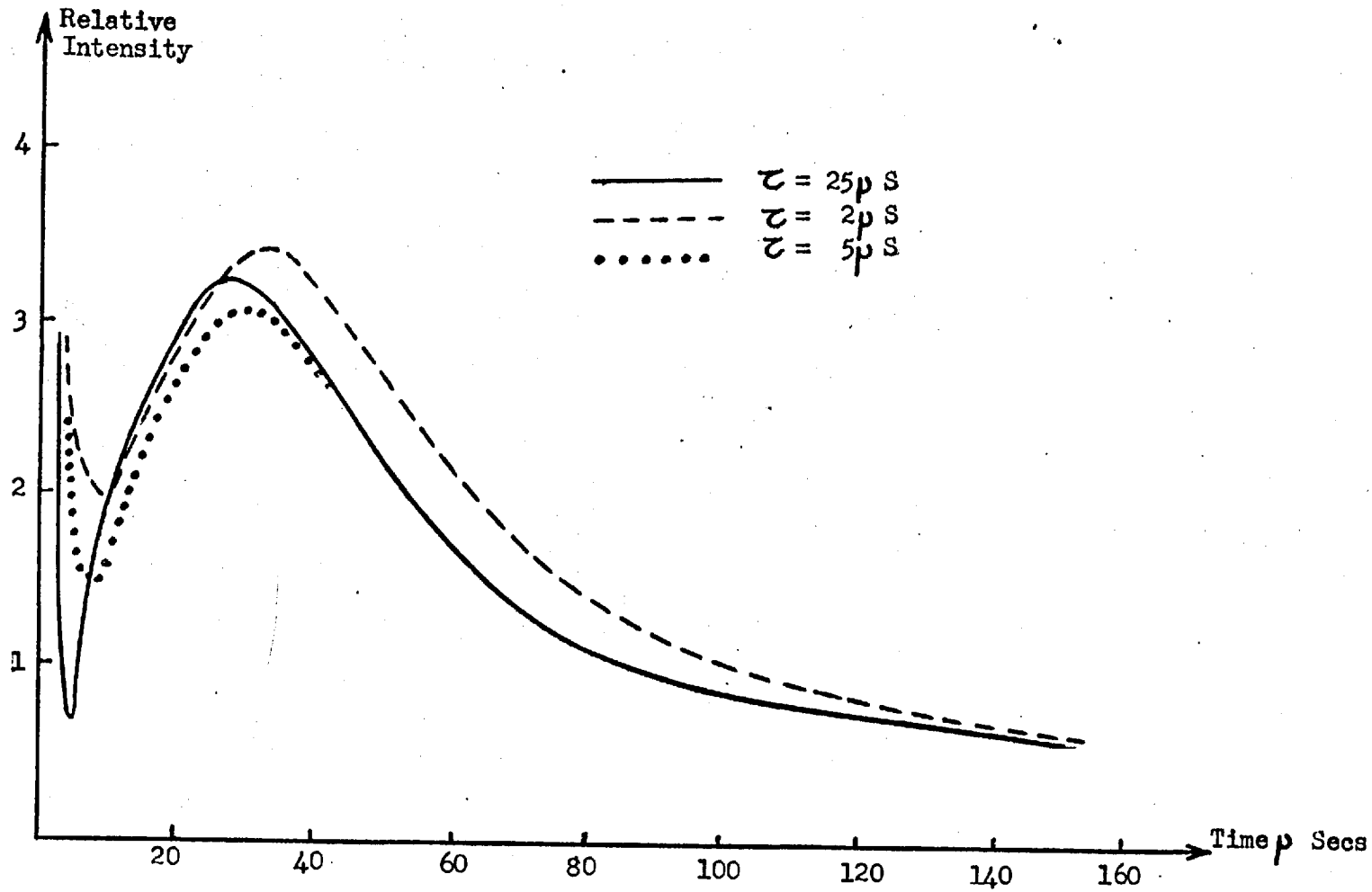

FIG. 4.5 Total integrated line 4471 for various values of Emitter Follower integrating time, τ .

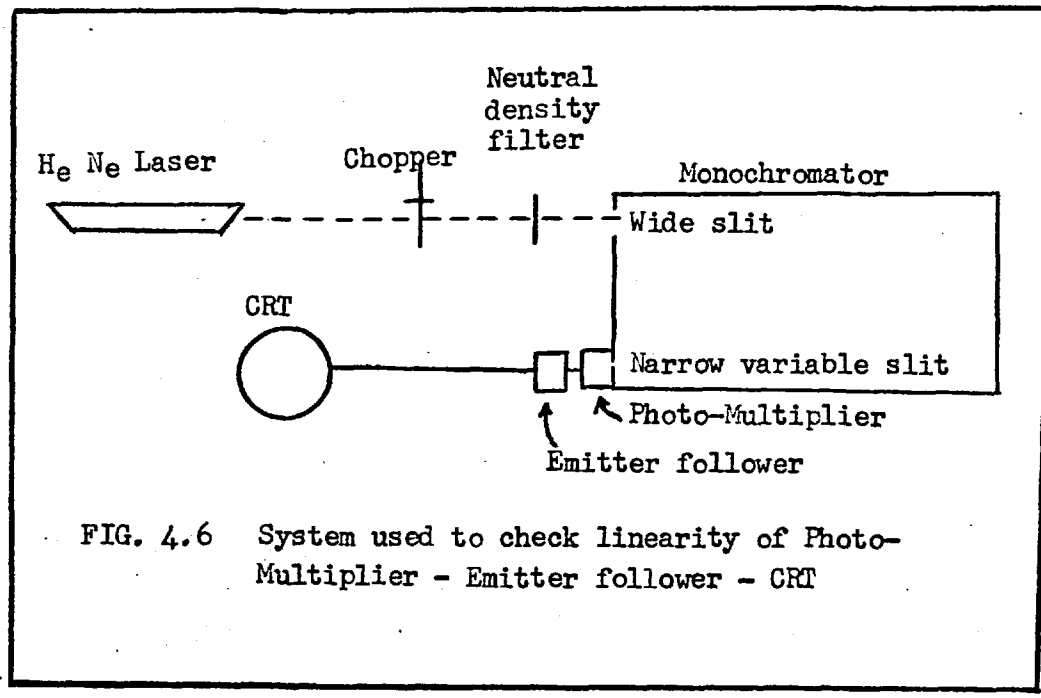

FIG. 4.6 System used to check linearity of Photo-Multiplier - Emitter follower - CRT

The source used was a HeNe laser which produced a spot about 3 mm diameter on the entrance slit of the monochromator. The laser beam was mechanically chopped at about 50 KHz and a series of neutral density filters were used to cover the whole operating range of the system. A wide ($\sim 100\mu$) entrance slit was used to produce a wide image on the exit slit. Then, as long as the exit slit is narrow compared to the entrance slit, the CRT reading should be proportional to the exit slit setting. Experiment showed that the system was linear.

THE LINE PROFILES

Each line was scanned in steps of .04Å in the line centre. This represents 30% of the instrument width. Every point on the profile was photographed five times, each shot superimposed on the same frame, and then a further shot, with the monochromator exit slit closed, was added to produce a baseline. Figs. 4.7 and 4.8 show typical frames, the first near the line centre and the second in the far wings. The wavelength band is 0.15Å.

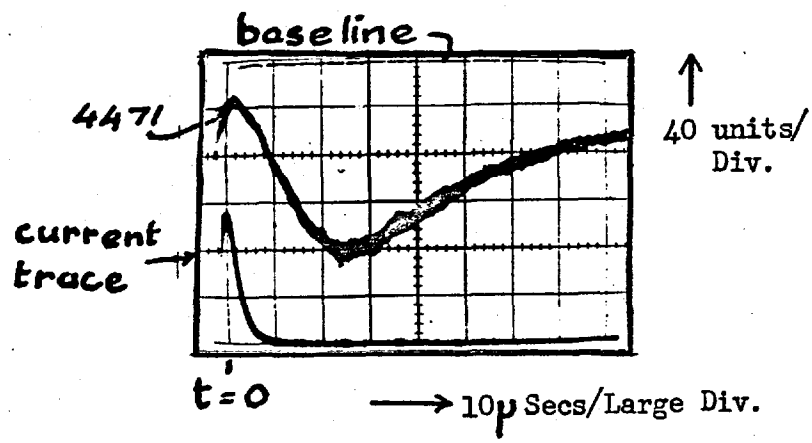

FIG. 4.7 LINE CENTRE

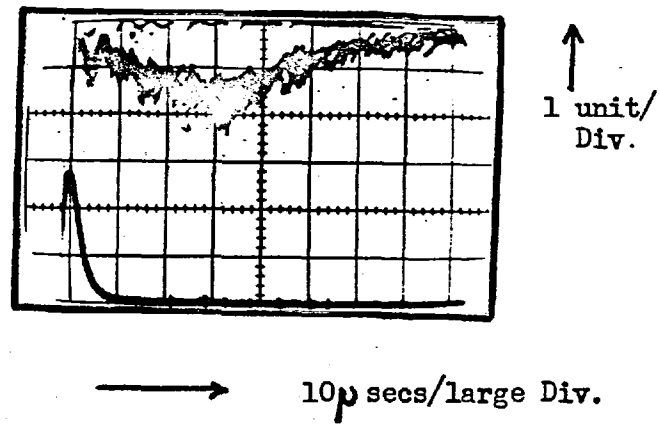

FIG.4.8 LINE WINGS

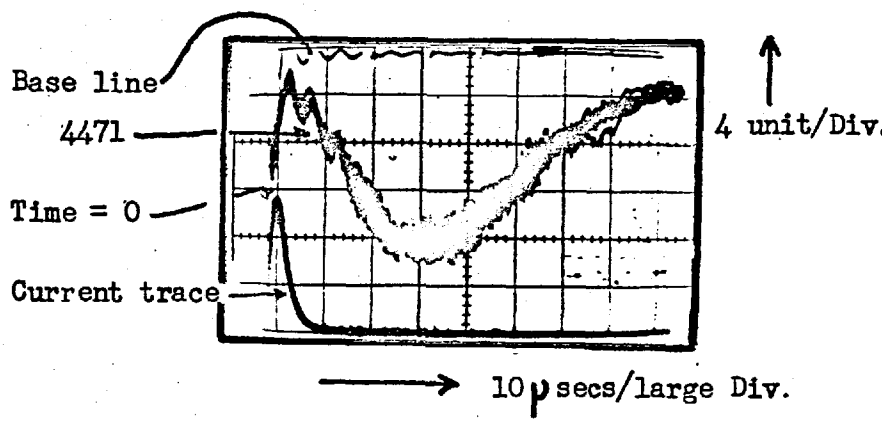

FIG.4.9 CENTRE FORBIDDEN
LINE

TYPICAL TIME HISTORIES OF SEVERAL REGIONS OF 4471

In the line centre, the separate shots can barely be distinguished. Here, the plasma reproducibility is $\sim 5\%$. This situation steadily deteriorates as the intensity falls until in the far wings the signal is largely dominated by photomultiplier noise. The measured line intensity at this point is, for 4471 at $n_e = 10^{15}$ a factor of about 200 less than the line centre. The success of the experiment depended critically on whether enough light was present to obtain accurate profiles of the forbidden component. Fig. 4.9 shows a typical photograph of the centre of the forbidden line at 4470 Å, with $n_e = 10^{15}$. Here the intensity is down by a factor of 10 on the centre of the allowed line. Nevertheless, it can be seen that photomultiplier noise did not present a severe problem.

OPTICAL ARRANGEMENT

It will be seen in Chapter 8 that the optical system was extremely important. The reason why this is so will become clear then. Fig. 4.10 shows the system used.

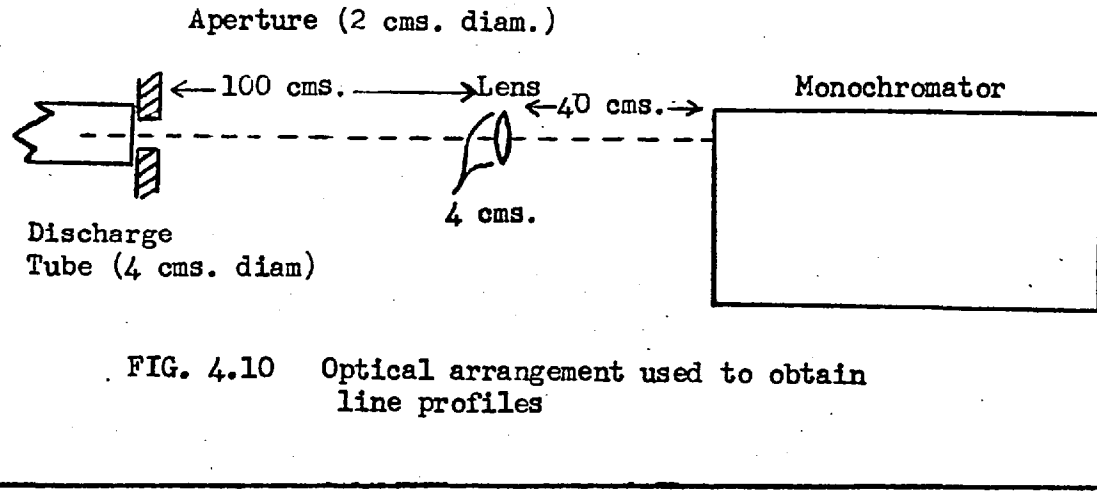

FIG. 4.10 Optical arrangement used to obtain line profiles

A single lens was used to produce an image of the plasma on the monochromator entrance slit. The finite length of the plasma tube prevented perfect focusing of the plasma, but the arrangement above had an image depth of focus of only about 5 cm. The size of the image varied from about 2 cm. diameter to about 1 cm diameter for different sections of the plasma. Therefore, by varying the height of the entrance slit, a considerable degree of control could be exercised over the region of plasma radiating into the monochromator. The significance of this will be discussed in Chapter 8.

A SURVEY OF THE EXPERIMENTAL WORK NECESSARY TO ESTABLISH LINE PROFILES

Before an experimentally observed profile can be compared with the theory, it is essential that the plasma parameters n_e (electron density), T_e (electron temperature), T_a (atom temperature) and τ_ν (optical depth) are known. It is also important to know the extent to which the profiles are distorted by radial density and temperature gradients in the plasma.

Chapter 5 - 8 deal with the diagnostics of the experiment. Although each parameter is treated in a separate chapter, there is considerable interdependence between them. For instance, in many cases lines are appreciably self-absorbed and when one such line has been used to measure the temperature, a correction for absorption was necessary. Similarly, density measurements assume a knowledge of the temperature and temperature measurements require information on the prevailing equilibrium relations which in turn depend on the density. Consequently, the following chapters continually refer not only to previous chapters but also to subsequent chapters. The purpose now is to clarify any confusion before it arises.

Briefly, then, the format of Chapters 5 - 8 is as follows. Chapter 5 describes the technique used to measure the optical depth of the plasma in the region of a line and how the measured line is corrected to produce what would be observed were the plasma optically thin. This procedure is applied to all lines, whether explicitly stated or not, used to determine densities and temperatures.

Chapter 6 is concerned with density measurements. Laser interferometry was used to measure n_e. This method is independent of the temperature and absorption but does depend, though not critically, on the population densities of the atomic states. Sufficiently accurate determinations of the relevant population densities can be made with only very approximate values of and the temperature. A further determination of n_e was made from the half-widths of H_β. Corrections to the half-width for both absorption and temperature have been made where necessary.

Chapter 7 deals with temperature measurements. Both Doppler temperatures and electron temperatures have been measured and again some knowledge of n_e and the equilibrium conditions is required. Finally, Chapter 8 describes the extent and effect of radial gradients on the profiles. In practice, radial gradients

were not important and therefore the parameters measured in Chapters 5 - 7 were assumed to describe a homogeneous column of plasma down the centre of the tube.

With this brief introduction the experimental work will be described in the following chapters.

CHAPTER 5

THE OPTICAL DEPTH OF THE PLASMA

It is essential to investigate the optical depth, $\tau(\omega, x)$, of the plasma to determine what effect self-absorption has on radiation emitted by the plasma. The optical depth is given by eq. 5.1.

$$\tau(\omega, x) = \int_{x}^{x_o} k'(\omega, x)\, dx \qquad 5.1$$

Here, x_o is the near boundary of the plasma and $k'(\omega, x)$ the effective absorption, i.e. the difference between absorption and re-emission.

$$k'(\omega, x) = 2\pi^2 r_o c f_{mn} N_n(x)\left[1 - \frac{g_n}{g_m}\frac{N_m(x)}{N_n(x)}\right] L(\omega, x) \qquad 5.2$$

This is the effective absorption coefficient of the line nm, f_{mn} is the oscillator strength, r_o the classical electron radius, N_m and N_n the population densities of the upper and lower states and g, the statistical wt.

Assuming that the line profile is dispersive, and using the normalisation condition that,

$$\int_{-\infty}^{\infty} L(\omega)\, d\omega = 1$$

gives $$L(\omega) = \frac{d}{\pi(\omega^2 + d^2)}$$

where d is the $\frac{1}{2}$ ($\frac{1}{2}$)width of the line. The optical depth of the line at line centre may then be written as,

$$\tau(\omega_o) = 2\pi^2 r_o c f_{mn} N_n L(\omega_o) X_o \quad \cdots X_o = \text{plasma length}$$

Note that the term $\frac{g_n N_m}{g_m N_n}$ has been dropped. This will not effect an order of magnitude calculation.

$$\therefore \tau(\omega_o) = 2\pi^2 r_o c f_{mn} N_n \cdot 1/\pi d \cdot X_o$$
$$= 2\pi^2 r_o c f_{mn} N_n \lambda^2 / 2\pi^2 c d' X_o$$

where d' is the $\frac{1}{2}$ ($\frac{1}{2}$)width expressed in cms rather than cms^{-1} and λ is the wavelength of the line centre.

$$\therefore \tau(\omega_o) \sim 2.10^{-13} N_n$$

Hence, when N_n is $\sim 10^{13}$, the optical depth $\tau(\omega_o) \sim 1$ and the absorption at the line centre will be significant.

A crude estimate of the population N_n can be obtained by assuming that the state n is in LTE with the electrons and using a modification of Saha's equation (Griem 1964),

$$n_e N_1^z / N_n^{z-1} = 2 g_1^z / g_n^{z-1} \left[mkT / 2\pi\hbar^2 \right] \exp(-E_n / kT)$$

where N^{z-1} is the ground state population density of the ~~first~~ z^{th} ionization stage. When $n_e \sim 10^{15}$ and $T \sim 1$eV

$$N_{2^3P} \sim 10^{14}$$

This suggested that there was a strong possibility that

absorption of 4471 would therefore, be severe. However, the LTE assumption is not necessarily valid. In fact it will be shown later that LTE does not hold for the 2^3P level and that the lower lying levels were underpopulated with respect to the electron density. It is difficult to calculate the magnitude of the lower state population and so there remained the possibility that absorption was an important effect.

Initial measurements of the line profile of 4471 showed that its half-width was almost a factor of two broader than predicted by both BCS and by Griem. One possible cause of this discrepancy was self-absorption of the radiation in the plasma. Therefore an experiment was carried out to measure the optical depth of the plasma. Fig. 5.1 shows the apparatus used.

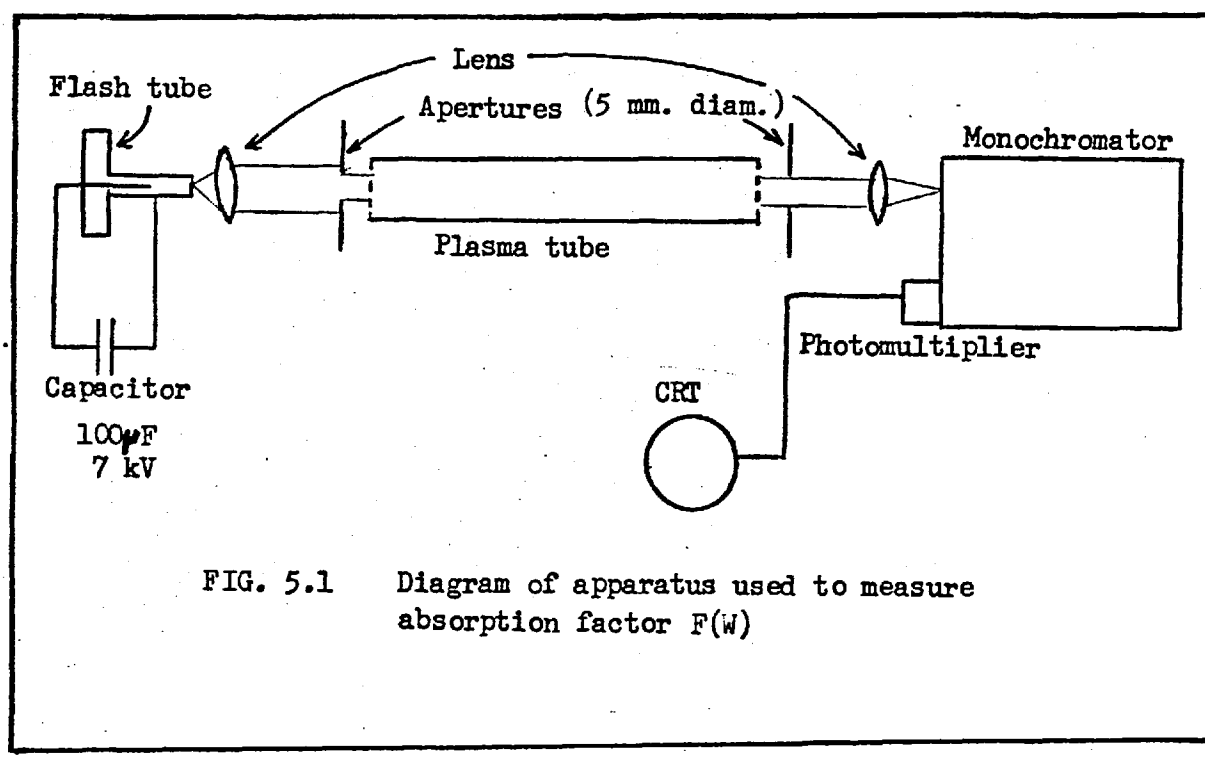

FIG. 5.1 Diagram of apparatus used to measure absorption factor F(W)

A background continuum source was used to irradiate the plasma. The combined light from the plasma and source was then scanned across a line and the absorption-profile of the line was measured. The background source was a flash-tube operated by a $10\mu F$ capacitor charged to about 7kV. The pulse width was $2\mu S$ and about five time more intense, under operating conditions than the peak intensity of 4471. Fig. 5.2 shows the triggering sequence used in the experiment.

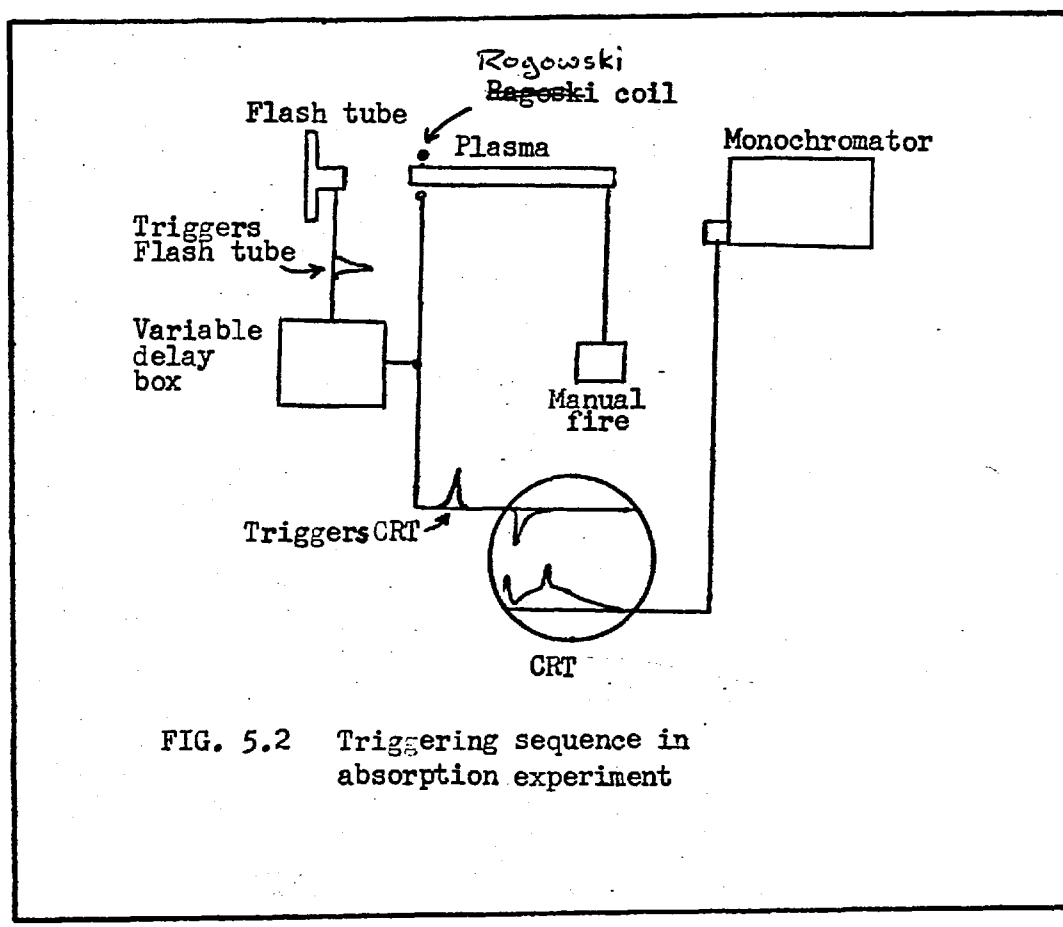

FIG. 5.2 Triggering sequence in absorption experiment

Use was made of the dual time base and delayed trigger facilities of a Tekronix 556 CRT. The Rogowski coil pulse was used to trigger the upper beam of the CRT. A variable time delayed pulse output from the CRT then triggered the flash tube. In this way the absorption in the plasma could be measured at any point in the plasma decay. Fig. 5.3 shows typical CRT traces.

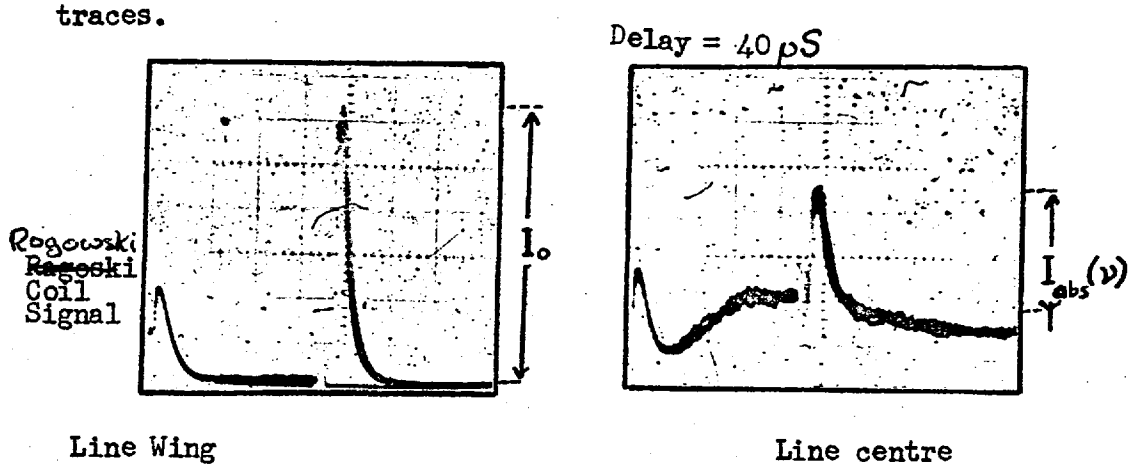

FIG. 5.3 Typical absorption results for 4471

The lower trace is the signal from the photomultiplier and shows 4471 with the flash tube pulse superimposed on top of it after a delay. Each photograph shows about five shots of the same event. The magnitude of the unabsorbed signal from the flash tube was measured by extending the line scan out beyond the line wings where absorption is negligible. In the line centre, where the plasma emission was appreciable, the flash tube signal was

corrected by subtracting ~~plasma~~ the ~~emission~~ plasma emission signal from the flash-tube signal. The flash tube continuum was scanned, in the absence of the plasma, across the region of the line to make sure there was no inherent variation in the continuum intensity.

In order to correct the observed line profiles for absorption, the following procedure was carried out. The observed emission, $I_{obs}(\nu)$, can be written

$$I_{obs}(\nu) = S_\nu \left[1 - e^{-\tau_\nu}\right] \qquad 5.4$$

S_ν is the source function.

The intensity of an optically thin line, $\tau_\nu \ll 1$ may be defined as

$$I_{thin}(\nu) = S_\nu \tau_\nu \qquad 5.5$$

Substituting 5.5 into 5.4 gives

$$I_{obs}(\nu) = \frac{I_{thin}(\nu)}{\tau_\nu}\left[1 - e^{-\tau_\nu}\right]$$

$$\therefore \; I_{thin}(\nu) = I_{obs}(\nu)\left[\frac{\tau_\nu}{1 - e^{-\tau_\nu}}\right] \qquad 5.6$$

If the unabsorbed flash tube signal is I_o and the observed, i.e. absorbed, profiles are $I_{abs}(\nu)$ then

$$e^{-\tau_\nu} = \frac{I_{abs}(\nu)}{I_o} \qquad 5.7$$

Eqs. 5.6 and 5.7 yield

$$I_{thin} = I_{obs}(\nu)\left[\frac{\ln(I_o/I_{abs}(\nu))}{1 - I_{abs}(\nu)/I_o}\right]$$

$$\equiv I_{obs}(\nu)\, F(\nu)$$

Values of $F(\nu)$ have been calculated from measured absorption profiles and used to correct the observed profiles. Fig. 5.4 shows $F(\nu)$ plotted out for the line 4471 at various times in the plasma decay. Similar curves have been obtained for 4921, 3889, and 4713.

Fig. 5.4 shows that the peak absorption increases with time. This occurred because of (a) the population density of the lower state increased with time for at least the first 40 - 50μS, (b) the line width decreased with time which produced a narrower absorption line with a higher peak. The curves for 4921 are similar to those of 4471 but smaller because of the lower oscillator strength of 4921. Typical peak values of $F(\nu)$ for

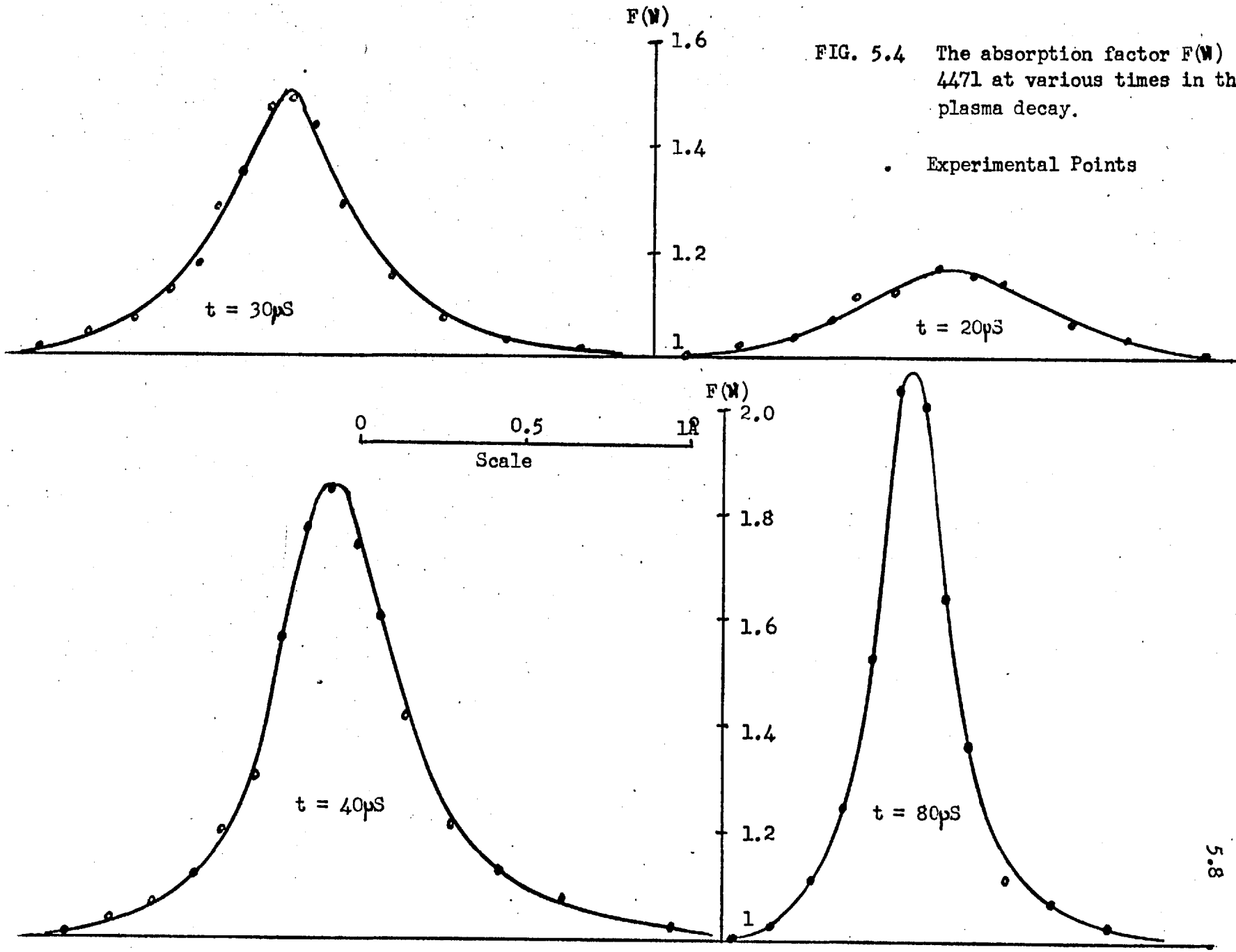

FIG. 5.4 The absorption factor F(W) for 4471 at various times in the plasma decay.

. Experimental Points

4921 are $\simeq 1.1$. At $t = 20\mu s$, the absorption of 4921 was negligible and so no correction was necessary to emission profiles emitted at this time.

CALCULATED POPULATION DENSITIES

From measurements of the total absorption in a line, it is possible to make an estimate of the population density of the lower state of the line. We have

$$k'(\omega, x) = 2\pi^2 r_0 c f_{mn} N_n(x) \left[1 - \frac{g_n N_m(x)}{g_m N_n(x)}\right] L(\omega, x) \qquad 5.2$$

The second term on the RHS of eq. 5.2 may be safely neglected. This is because, even if LTE conditions were satisfied, the populations N_n and N_m would be related by the Boltzman factor.

$$\frac{N_n}{N_m} \simeq e^{\frac{-E_n + E_m}{kT}} \simeq 0.05$$

Alternatively, if N_m is assumed to be in LTE with higher states only, then using eq. 5.3

$$N_m \sim 10^{12}$$

$$\text{or } \frac{N_m}{N_n} \gtrsim 10^{-1}$$

Therefore equation 5.2 becomes

$$k'(\omega,x) = 2\pi^2 r_0 c f_{mn} N_m(x) L(\omega,x) \qquad 5.8$$

It is also convenient to drop the x dependence in eq. 5.8. Again, this does not cause a serious error. It will be shown in a later chapter that the plasma is homogeneous down the centre of the tube, which was the region in which the absorption experiment was carried out. Eq. 5.8 can now be integrated ω.r.t. ω and x.

$$\int_{x_0}^{0} k'(\omega)\,dx = \tau(\omega) = k'(\omega)\,x_0$$

Where x_0 is the plasma length.

$$\int \tau(\omega)\,d\omega = 2\pi^2 r_0 c f_{mn} x_0 N_m \int L(\omega)\,d\omega \qquad 5.9$$

The line shape, $L(\omega)$ is defined such that,

$$\int_{-\infty}^{\infty} L(\omega)\,d\omega = 1$$

Rewriting the integral over ω in terms of the wavelength λ expressed in angstroms gives

$$\int \tau(\lambda)\,\frac{2\pi c}{\lambda_{mn}^2}\,d\lambda = 2\pi^2 r_0 c f_{mn} N_n x_0 \qquad 5.10$$

After substitution of the constants in 5.10, we have

$$\int \tau(\lambda)\, d\lambda \simeq 5.10^{-19} \cdot \lambda_{mn}^{2} f_{mn} N_n \qquad 5.11$$

The LHS of eq. 5.11 may be determined from the absorption measurements.

$$\tau(\omega) = \ln \left[I_o / I_{abs}(\omega) \right]$$

By plotting $\ln \left[I_o / I_{abs}(\omega) \right]$, the $\int \tau(\omega)\, d\omega$ may be obtained. More simply, for an order of magnitude calculation of N_n, the integral may be evaluated by taking the product of the half width of the profile $\left[\ln I_o / I_{abs}(\omega) \text{ o. } \omega \right]$ and the log of the peak absorption coefficient.

$$\int \tau(\lambda)\, d\lambda = \ln \left[I_o / I_{pk}(\lambda) \right] \times d$$

$$\equiv \Delta$$

Finally we have,

$$N_n \simeq 2.10^{18} \cdot \frac{\Delta}{f_{mn} \lambda_{mn}^{2}} \qquad 5.12$$

Table 5.1 lists the results for the lines 4471, 4921, 4713 and 3889 together with the lower state designations for each line at

various times in the discharge.

	Designation	Time μS			
		20	30	40	80
4471	2^3 P	$1 \cdot 6.10^{11}$	$3 \cdot 7.10^{11}$	$5 \cdot 7.10^{11}$	$3 \cdot 9.10^{11}$
4921	2^1 P	*	$1 \cdot 3.10^{10}$	$1 \cdot 3.10^{11}$	9.10^{9}
4713	2^3 P	*		5.10^{11}	4.10^{11}
3889	2^3 S	*		$\phi > 10^{13}$	

TABLE 5.1 Calculated population densities from absorption profiles

* Absorption too small to be measured

ϕ Total absorption at line centre so large that only a lower limit in N_n is given.

The values for N_n given in table 5.1 fall between values calculated from (a) eq. 5.3 where the state is assumed to be in LTE with the electron density and (b) and the equation

$$\frac{N_n}{N} = \frac{g_n \exp(-E_n/kT)}{Z(T)}$$

N = total no. of atoms

Z(T) = partition fn.

Where the state n is assumed to be in LTE with all other levels,

and in particular, the ground state. Clearly the n = 2 states are not in LTE with the electrons and it is difficult to make any further statements about their populations without considering the full population and depopulation mechanisms operating in the plasma.

CHAPTER 6

MEASUREMENT OF THE ELECTRON NUMBER DENSITY

Accurate measurements of the electron density, n_e , are essential if experimental profiles are to be compared with theoretical profiles. This is because the line profiles of the two lines 4471 and 4922 are very sensitive to n_e . Well established techniques exist for measuring n_e In the present experiment, a laser interferometer was used as the primary means of determining n_e as it has the advantage of permitting measurements of spatial gradients in n_e to be made. The laser results were verified by measuring the half-width of H_β which is strongly dependent on n_e.

LASER INTERFEROMETER

The laser interferometer measures the change in the refractive index of the plasma at the frequency of the lasing transition. The assumption was made, and will be justified later, that only free electrons were contributing, to any significant extent, to the change in the refractive index. Then the refractive index is given by eq. 6.1.

$$(n-1) \simeq - \frac{r_o \lambda^2}{2\pi} n_e \qquad 6.1$$

Where n is the refractive index at wavelength λ.

Fig. 6.1 shows the experimental arrangement of the laser interferometer system.

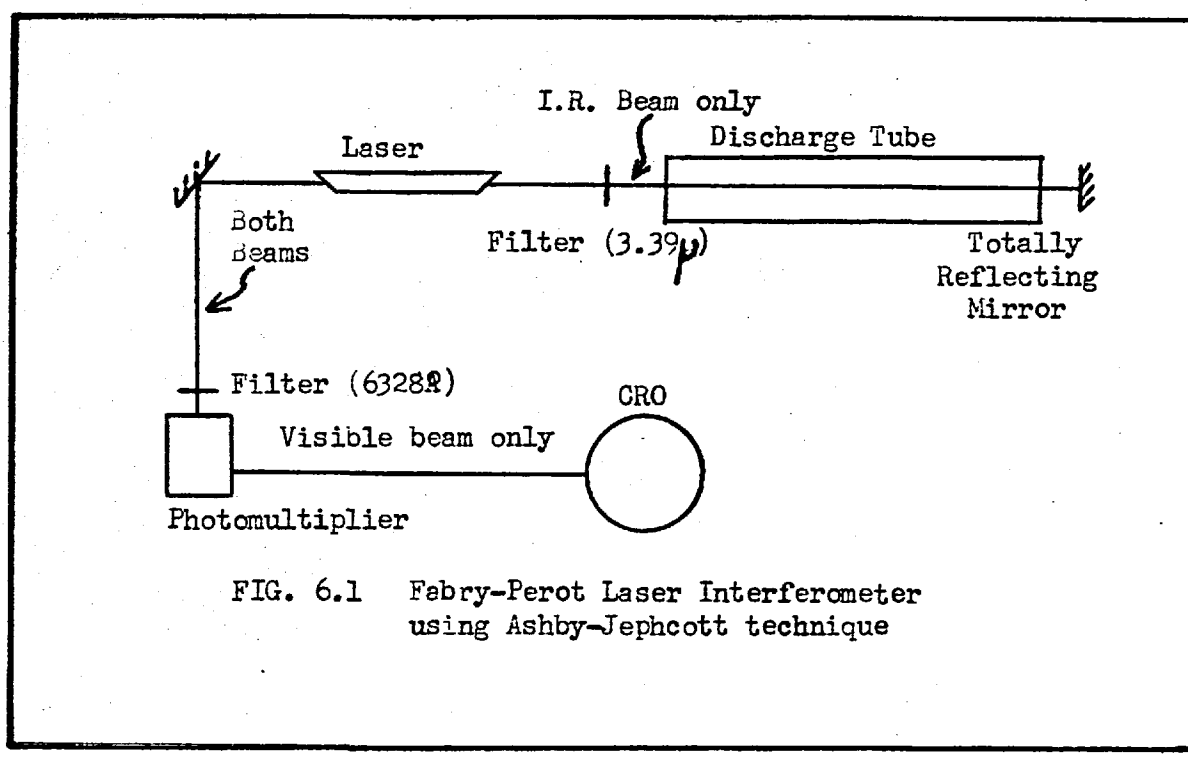

FIG. 6.1 Fabry-Perot Laser Interferometer using Ashby-Jephcott technique

The system shown in Fig. 6.1 is a Fabry-Perot interferometer using a technique due to Ashby and Jephcott (1963). This method uses the infra-red lasing transition at 3.39μ of a HeNe laser to respond to changes in the refractive index of the plasma. The infra-red line then modulates the intensity of the red line at 6328Å which is detected by a photomultiplier at the far end of the laser. The advantage of the method is that it is much easier to detect the visible line than the infra-red line and using the latter as the plasma probe gives much more accurate measurements of n_e. This can be seen by applying eq. 6.1 to the Fabry-Perot laser system.

$$2L n_e = 0{\cdot}196.10^{17} \lambda N \qquad 6.2$$

Here 2L is the total path length of the laser beam through the plasma, λ the wavelength of the probing beam expressed in μ, N the interference fringe number.

The working range of n_e was $10^{15} \sim 10^{14}$. This produces -

$\lambda = \cdot 6328$, total no. of fringes $= \frac{1}{2}$

$\lambda = 3{\cdot}39$, " " " " $= 3$

Clearly, it was essential to use the infra-red transition.

Fig. 6.2 is a block diagram of the triggering sequence.

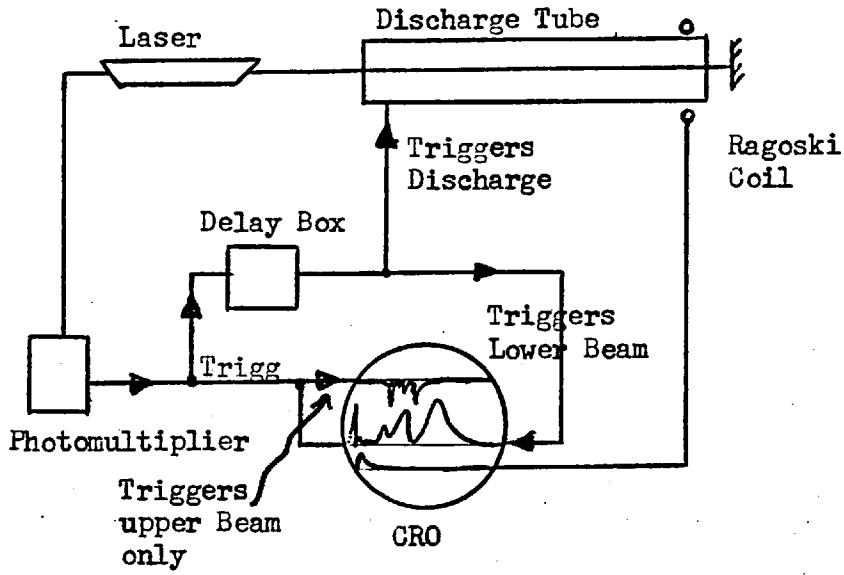

FIG. 6.2 Triggering sequence used in Laser Interferometer

The triggering arrangement was designed to eliminate, as far as possible, the effect of background vibration fringes which were always present. It was difficult to determine where the fringes due to changes in the refractive index ended and where the fringes due to vibration began unless care was taken. The upper beam of the CRT was triggered by the vibration fringes at a point corresponding to a vibration fringe minimum. After a time delay, which

was small compared to the vibration fringe frequency, the lower beam and the discharge were simultaneously triggered. Fig. 6.3 shows the form of a typical CRT trace.

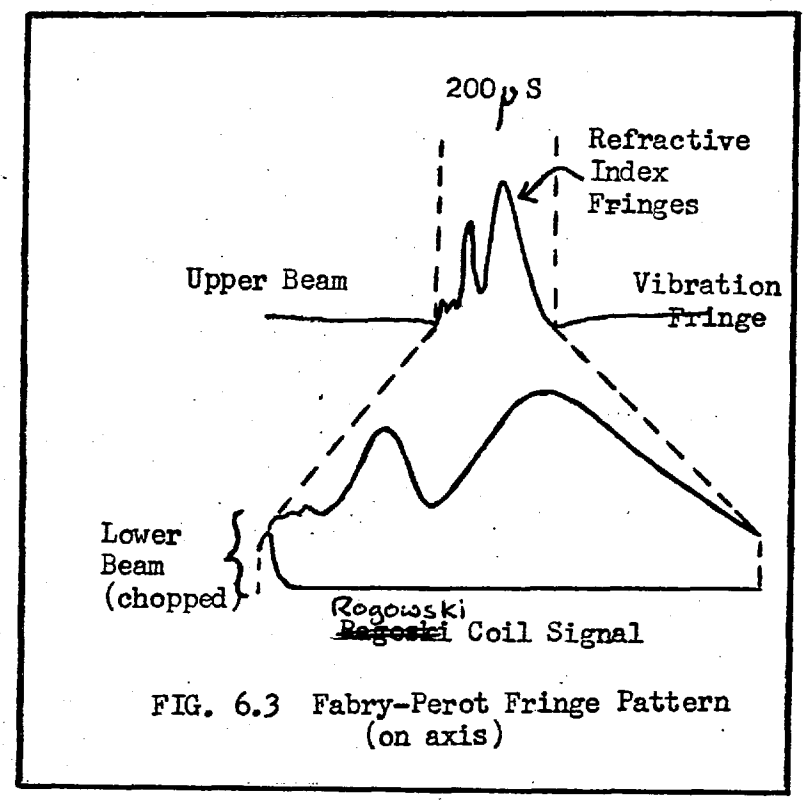

FIG. 6.3 Fabry-Perot Fringe Pattern (on axis)

The upper beam shows the fringes on a much slower time-base. A correction was then made for a change in the phase of the interfering laser beam due to a vibration only. Fringes were counted back from the point where the trace returned to its initial level on the vibration fringe. Fig. 6.4 shows the density υ. time curve obtained from eight shots, each point representing one half fringe.

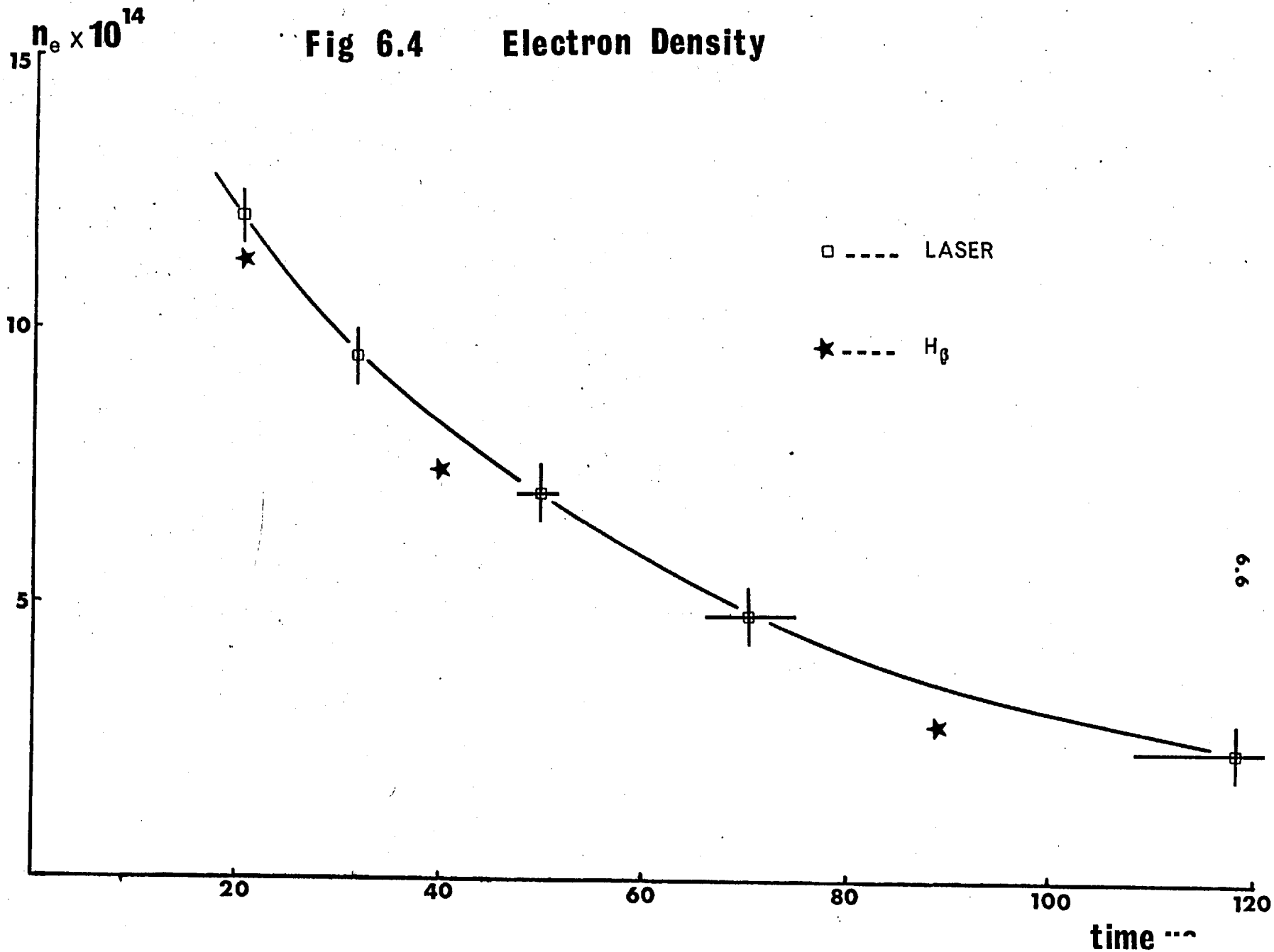
$n_e \times 10^{14}$
Fig 6.4 Electron Density
15
10
5
LASER
H_β
20
40
60
80
100
120
time

CONTRIBUTIONS TO THE REFRACTIVE INDEX OF THE PLASMA

It has been assumed above that only free electrons are contributing to any significant extent to the refractive index of the plasma. This assumption will now be justified. The free electron contribution to the refractive index, n, may be written as

$$(n-1)_{free\ el.} \simeq -\frac{r_o \lambda^2}{2\pi} n_e \qquad 6.3$$

Where r_o is the classical electron radius and λ, the wavelength at which n is calculated. The contribution from ions may be ignored immediately because its magnitude is less by a factor of the ion-to-electron mass ratio than that of the electrons. Bound electrons contribute to n_e according to eq. 6.4

$$(n-1)_{atoms} \simeq \sum_m \frac{r_o f_{mn} \lambda_{mn}^2}{2\pi} \left[1+\left(\frac{\lambda_{mn}}{\lambda}\right)^2+\dots\right] N_n \qquad 6.4$$

This estimates the effect from atoms in the state n. f_{mn} is the absorption oscillator strength of the transition mn, wavelength λ_{mn}. The sum is carried out over all upper states m. Equation 6.4 is valid only for large separations from the transition λ_{mn}, i.e. $|\omega-\omega_{mn}| \gg \Delta\omega_{mn}$ and can be used to estimate the

effect of the resonance lines of helium on the refractive index. Taking, for the resonance line, $N_n \sim 10^{16}$, $n_e \sim 10^{15}$, $f_{mn} \sim 1$ and $\lambda = 3.4\,\mu$ we have

$$\frac{(n-1)_{res.\,line}}{(n-1)_{free\,el.}} = \frac{f_{mn}\lambda^2_{mn}}{\lambda^2}\frac{N_n}{n_e} \sim 10^{-5}$$

Clearly, these states do not contribute significantly to n. A check must also be made on the meta-stable levels 2^3S. A lower limit on the population density of this state was obtained in the previous chapter as being $\sim 10^{13}$. A reasonable upper limit is $\sim 10^{14}$. Eqs. 6.3 and 6.4 then yield, for the series $2^3S - n^3P$.

$$\frac{(n-1)_{2^3S}}{(n-1)_{fr.\,el.}} \simeq 10^{-2}$$

The meta-stable state could, therefore, have contributed to a significant extent to the refractive index and a closer examination of the 2^3S population density is required. The lower limit, 10^{13}, on the density was calculated assuming the peak absorption coefficient of the line $3^3P - 2^3S$ at 3889Å was $\sim 10^2$ Although this was an arbitrary figure, chosen for convenience, no serious errors in the calculation of the 2^3S state density arise because the absorption coefficient enters the calculations only through the log.

i.e. $N_n \sim \ln\left[I_o / I_{pk}(\omega) \right]$

Choosing I_0/I_{pk} then gives $N_n \sim 10^{13}$ and, within experimental error, the absorption of the line is total at line centre. Now if the population density is assumed to be greater by a factor of 10, i.e. $N_n \sim 10^{14}$, total absorption will be observed not only in the line centre, but also in the line wings out to the point where $L(\omega) = 10^{-1} L(\omega_{pk})$. This would lead to a flat topped line profile for 3889. Comparison of profiles of this line taken in the end-on positions and in the side-on positions, that is with the monochromator viewing the flash tube through a diameter of the discharge tube, showed only a comparatively small difference between the two. The half-width of the line increased by 30% in the end-on position compared with the side-on position. At a density of 10^{14}, the half-width can be expected to increase by about 300%. Furthermore, no absorption could be detected, even at the line centre, in the side-on position in which the absorbing path length was decreased by a factor of 30. When $N_n = 10^{13}$, some degree of absorption would be observable at line centre.

These considerations show that taking $N_{2^3S} = 10^{14}$ certainly overestimates the true density, and even the lower limit of 10^{13} is probably too high. Therefore the contribution of this state

to the refractive index was under 1% of the free electron contribution.

The only other possible important contribution to n which can arise is that due to anomalous dispersion in the region of a line. The nearest line to the lasing line at $3{\cdot}39\mu$ listed in the National Bureau of Standards report NRSDC - NBS4 is the $1s4s\text{-}1s5p$ transition at $3{\cdot}33\mu$. An estimation of the effect of this line on the refractive index may be obtained from eq. 6.7 given by Griem (1964).

$$(n-1)_{line} \simeq \frac{r_o f_{mn} \lambda_{mn}^3 N_n}{4\pi\Delta\lambda} \qquad 6.7$$

Here, the term accounting for λ line emission has been neglected. The population of the lower state can be estimated from Saha's eq.

$$\frac{n_e N_1^z}{N_n^{z-1}} = \frac{2g^z}{g_n^{z-1}} \left[\frac{mkT}{2\pi\hbar^2}\right]^{3/2} \exp\left[-\frac{E_H}{kT}\right]$$

This yields $N_{1s4s} \simeq 10^9$ and finally

$$\frac{(n-1)_{line}}{(n-1)_{el}} \simeq 4.10^{-6}$$

These results show that only free electrons were causing changes in the refractive index.

SPATIAL MEASUREMENTS OF THE ELECTRON DENSITY

The curve shown in Fig. 6.4 is the result of measurements taken down the central axis of the discharge tube. Further measurements were taken 1 cm. off axis. This was as far off axis as the geometry of the electrodes permitted. The results were identical with those taken on axis except for a region in the far after-glow of the plasma. The traces consistently showed a sharp fall in the final half-fringe, corresponding to times of 100 μ and densities of 2.10^{14}. Fig. 6.5 shows such a trace.

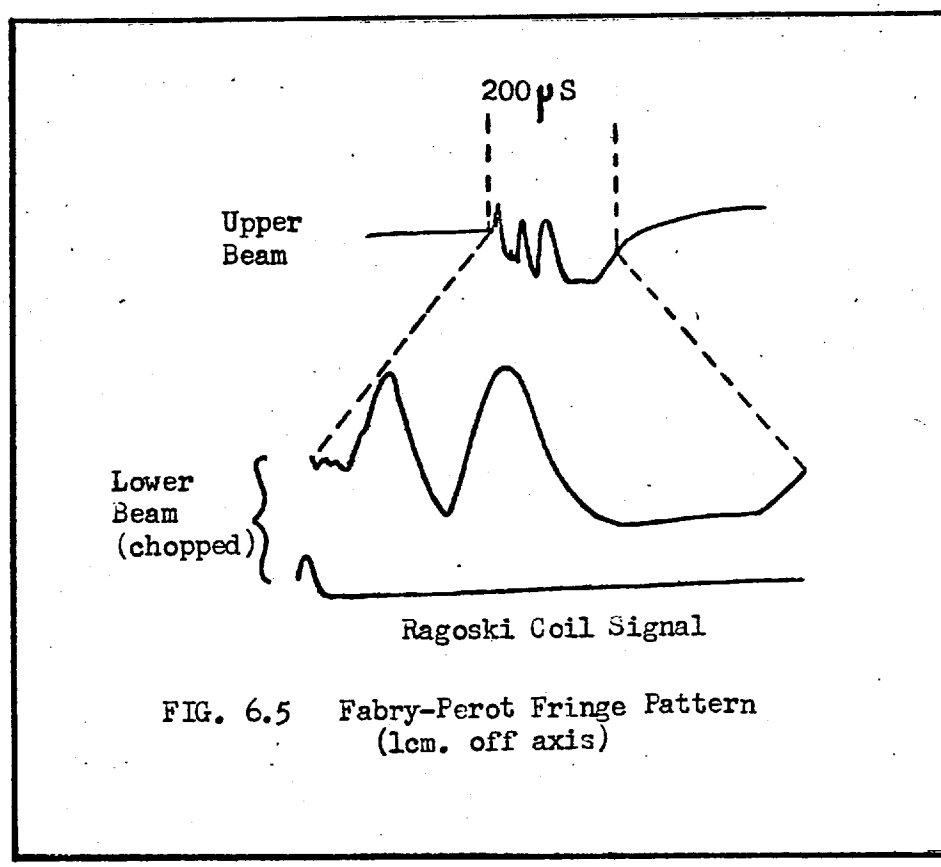

FIG. 6.5 Fabry-Perot Fringe Pattern (1cm. off axis)

The meaning of the last section of the trace is not clear. However, present interest does not extend beyond 80 μS and up to this time, there is no appreciable difference between the off and on-axis densities. The significance of the homogeneity of the electron density, at least in a central column of plasma 1 cm. radius, will be discussed in a later chapter.

MEASUREMENTS OF THE ELECTRON DENSITY FROM THE HALF-WIDTHS OF $H\beta$

Further measurements of the electron density were deduced from the half-width of the Stark broadened hydrogen line $H\beta$. The whole-half width of this line, assuming only Stark broadening is present, has been related by Griem (1964) to the electron density.

$$\Delta\lambda^{3/2} C(n_e, T_e) = n_e \qquad 6.8$$

$\Delta\lambda$ is the whole-half width expressed in angstroms and $C(n_e, T_e)$ are coefficients, tabulated by Griem (1964), which vary only slowly with n_e and T_e. Line profiles of $H\beta$ were obtained from hydrogen present as an impurity in the gas supply. Before calculating n_e from eq. 6.8, it was necessary to make appropriate corrections to the half-widths due to both absorption of the line

and Doppler broadening. An absorption experiment showed that the plasma was optically thin to $H\beta$. However, corrections were made to account for Doppler broadening. Table 6.1 shows the measured half-widths of $H\beta$ at various times in the discharge together with the corresponding Doppler widths which were calculated from measurements of the neutral helium line 4713 (see next chapter).

	TIME μS		
	20	40	90
Whole half-width $H\beta$ Å	2.12	1.69	0.97
Whole half-width 4713Å	0.15	0.11	0.10

TABLE 6.1 Whole-half widths of $H\beta$ and He I 4713

Instrument broadening must also be taken into account. The instrument whole-half width was 0.15Å. Because the Stark broadening is much larger than both Doppler and instrument broadening only a simple correction was made for the latter two. That is, the total width was assumed equal to the square root of the sum of the squares of the individual components. Using these corrected values of $\Delta\lambda$ and the tables of $C(n_e, T_e)$, the electron density was

calculated at times 20μS, 40μS and 90μS. These are plotted in Fig. 6.4 and can be seen to be in agreement with the laser results to about 5%.

CHAPTER 7

TEMPERATURE MEASUREMENTS

The profiles of 4471 and 4922 are functions of the electron temperature, Te, the atom temperature, Ta, and the ion-temperature, Ti. Both Griem and BCS assume that all three temperatures are the same in their calculations. In the present experiment, only Te and Ta have been measured but it can be shown that the ions and electrons are in thermal equilibrium among themselves and each other. Spitzer (1962) gives the following expression for the time required for an electron gas to establish a Maxwellian distribution among themselves.

$$t_{ee} = \frac{0.266\, T_e^{3/2}}{n_e \ln \Lambda}$$

$\ln.\Lambda$ is a slowly varying function of n_e and Te and is about 6 when $n_e = 10^{15}$ and Te = 10,000°K. The value of t_{ee} can then be estimated as $\sim 10^{-11}$ secs. The corresponding time for the ions is longer by a factor of $\left[\frac{m_i}{m_e}\right]^{1/2}$ and hence $t_{ii} \simeq 5.10^{-9}$ sec. It can also be shown that t_{ie}, or the time for electrons and ions to come to equilibrium with each other is $\simeq \frac{m_i}{m_e} \cdot t_{ee} \simeq 10^{-7}$ s. Now typical times of interest in the present plasma are $\sim 10^{-5} - 10^{-4}$ secs. and therefore the electrons and ions can be expected to be in thermal equilibrium i.e. $T_e = T_i$. A rough estimate can be made of t_{ai} as being about one order of magnitude larger than t_{ii} or $t_{ai} \sim 10^{-6}$ sec. It is, therefore, not possible to state that $T_i = T_a$ but, as T_a has been independently measured, this is not important.

ATOM TEMPERATURE, Ta

The atom temperature affects the line profile of 4471 through the Doppler effect, At typical densities and temperatures in this work, the Doppler half-width was about 0.2Å. The theoretical profiles already contain the Doppler width at temperatures in the range 5,000°K - 40,000°K and profiles for intermediate atom temperatures can easily be obtained by convolving an extra gaussian profile into the theoretical profile.

The atom temperature was obtained from half-width of the neutral helium line $2^3P - 4^3S$, 4713Å. This line was sufficiently intense that profiles could be constructed even at late times in the plasma decay. Also it had a narrow Stark width, and although not quite optically thin, a correction could be made for finite optical depth. 4713 was, in fact, the only line which satisfied all these criteria. The more intense lines, which were low lying series members, suffered heavily from self-absorption while the higher lying lines, although optically thin, were too weak and often strongly Stark broadened. Temperatures were obtained using eq. 7.2

$$kT = 4 \cdot 7 \cdot 10^8 \left[\frac{\Delta\lambda}{\lambda}\right]^2 A \qquad 7.2$$

kT is the temperature in eV, $\Delta\lambda$ the whole-$\frac{1}{e}$ width of the line measured in angstroms and A the atomic weight of the atom.

Before the Doppler half-width was extracted from the measured profiles, a correction was made to remove the instrument width from the total measured width. This was done by convolving a pure gaussian profile, representing the Doppler broadening of the line, with the instrument profile. Various Doppler profiles were used until a fit was obtained between the final convolved profile and the measured profile. Table 7.1 shows the total

measured half-widths of 4713, the calculated Doppler half-widths, the Stark half-widths, taken from Griem (1964), and the instrument width.

	TIME μs		
	20	40	80
Total half-width	19.5 *	17.5	15
Doppler half-width	18.5	12	9
Stark half-width	4.1	2.8	2
Instrument half-width	12	12	12

TABLE 7.1 Half-widths of He I 4713 and extracted Doppler widths

* units are degrees ($64^{\circ} \equiv 1\text{Å}$)

A further approximate correction has been made to account for the Stark width of the line. This was done using the Voigt equation for combining the half-widths of dispersive and Gaussian profiles.

$$B = [D^2 + 2 \cdot 8G^2]^{1/2} + D \qquad 7.3$$

B is the whole half-width of the combined profiles, D the half-half width of the dispersive component and G the $\frac{1}{e}$ —half-width of the Gaussian component.

Assuming that the Stark profile is dispersive, a new Doppler width, G, was found such that when substituted into equation 7.3, the combined width, B, was equal to the previously calculated value of the Doppler width. This procedure exaggerated the effect of the Stark width and hence gave a lower limit on the true Doppler width. Ignoring the Stark width, on the other hand, produced an upper limit on the Doppler width. The upper and lower limits, together with their associated temperatures are listed in Table 7.2.

	TIME μs		
	20	40	80
Doppler width (max.)	13.5	12	9
" " (min.)	10	9	9
Temp. (Max.) eV	1.6	1.3	0.5
" (min.) eV	.85	0.7	0.5

TABLE 7.2 Upper and lower limits on Doppler temperature

Fig. 7.1 shows curves corresponding to the upper and lower limits in Ta. As can be seen, there is a factor of two uncertainty in the temperature during the early stages of the plasma decay. This is not too serious for the following reasons –

FIG 7.1

PLASMA TEMPERATURES

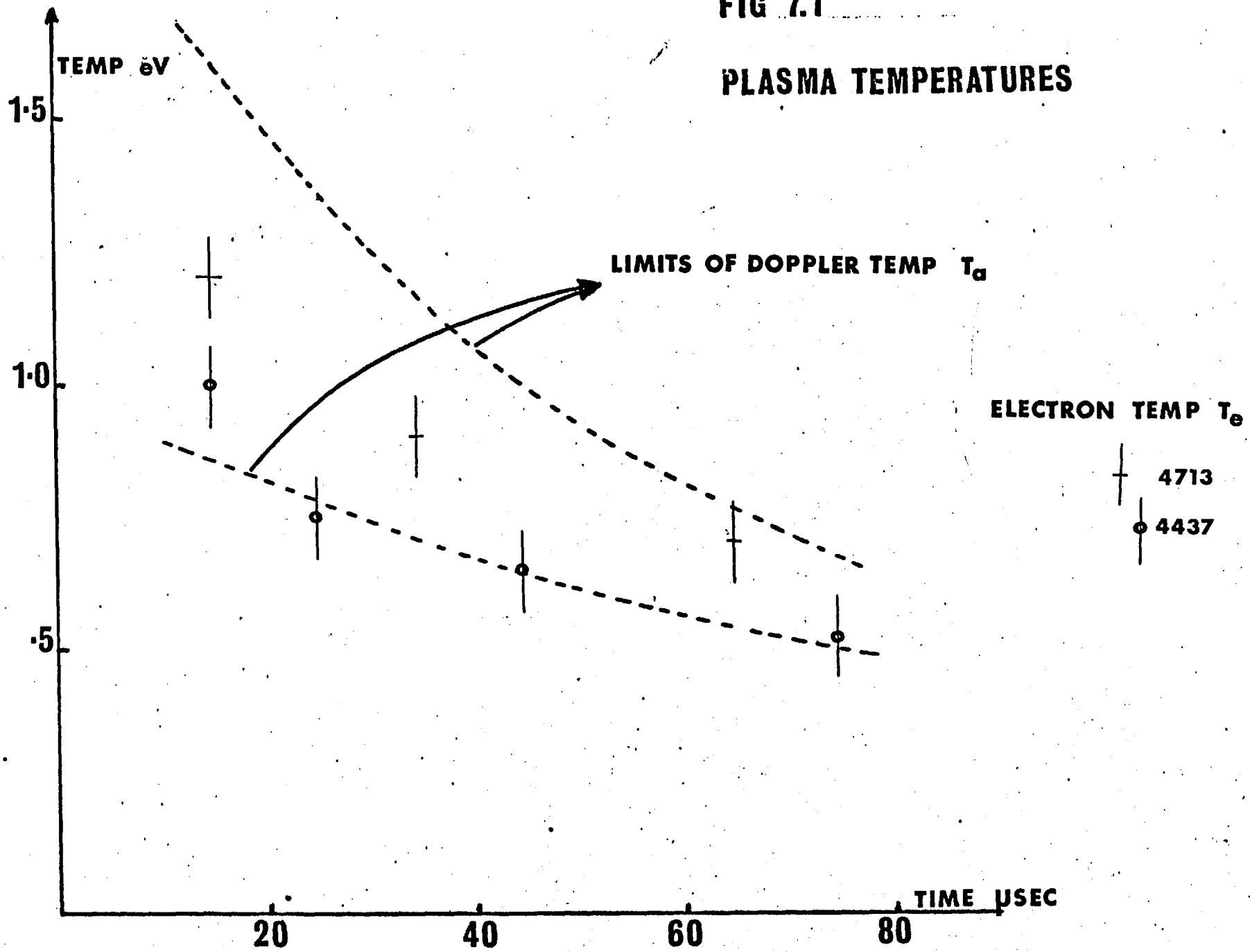

(a) the Doppler temperature effects both the allowed and forbidden components of 4471 in the same way so that their relative intensities and half-widths were not strongly effected,

(b) the half-width was in any case proportional to only the square root of the temperature,

(c) at early times, the half-width of 4471 was dominated by Stark broadening.

However, the effect on the profiles of 4471 of changing the temperature will be investigated in a later chapter.

THE ELECTRON TEMPERATURE

Three methods were used to determine the electron temperature

(a) a Boltzman plot of line intensities,

(b) continuum slope measurements,

(c) relative line to continuum ratios.

The first and third of these methods required that the upper states of the lines involved were in LTE with the electrons. Therefore, before either of these methods could be used, an estimation of the lowest lying atomic state in LTE with the electrons had to be made. This was determined using a criterion given by Griem (1964).

$$n_e \geq 7.10^{18} \frac{z^7}{n^{17/2}} \left[\frac{kT_e}{z^2 E_H}\right]$$

n_e is the electron density, n the principal quantum of an atomic state, z the degree of ionisation of the atom or ion, E_H the ionisation potential of hydrogen.

Equation 7.4 estimates the electron density required for a particular state, n, to be in LTE with the electrons. Assuming $RT \sim 1$ and $n_e \simeq 10^{14}$ eq. 7.4 reduces to

$$n^{17/2} \geq 2.10^{14} \qquad 7.5$$

The lowest value of n which satisfies equation 7.5 is n = 4. When n_e is 10^{15}, the constraint on n can be lowered to n = 3 but as eq. 7.4 is only approximate, only those lines whose upper state principal quantum number was greater than 3 were assumed to be in LTE with the electrons.

BOLTZMAN PLOT

The ratio of the total intensities of two lines whose upper states are in LTE with the free electrons is given by

$$\frac{I_1 \lambda_1^3 g_2 f_2}{I_2 \lambda_2^3 g_1 f_1} = \exp\left[\frac{kT_e}{E_1 - E_2}\right]^{-1} \qquad 7.6$$

I is the intensity of the line, λ the wavelength, g the statistical

weight of the upper level, f the oscillator strength and E the energy of the upper level.

Plots were made of the total intensity of a large number of lines whose upper state principal quantum number lay in the range n = 4 - 7 (beyond n = 7, the lines were too faint to observe). A modified form of eq. 7.6 was used

$$\ln\left[\frac{I\lambda}{gA}\right] \sim \frac{E'}{RT_e} \qquad 7.7$$

A is the transition probability and E' the ionisation energy of the level in question.

The total intensities were measured initially by opening up the exit slit of the monochromater to 6 Å while keeping the entrance slit at 0.15Å. In this way, the whole line was observed in one shot. This saved the lengthy procedure of scanning across each line but suffered from a disadvantage in that the wide exit slit increased the probability of including an impurity line in the total intensity. No corrections for self-absorption were made at this stage. The final plot according to eq. 7.7 did not yield a straight line. Nor was there any apparent asymptotic behaviour of the points towards a straight line. The points were, in fact, almost random. The electron temperature, in so far as it could be measured at all,

was about 0.1 eV.

In an attempt to improve on this situation, two line series were measured in greater detail. These were $2\,^3P - n\,^3D$ and $2\,^1P - n\,^1D$ series, with $n = 4 - 7$. The lines involved were scanned on a shot-to-shot basis and line profiles obtained. In this way, impurity lines which might have been included in the previous method, were eliminated. Finally, corrections were made for self-absorption where necessary, though for most of the lines, $n \geq 5$, these were slight or entirely negligible. Again a large scatter appeared on the plot and temperatures in the region of 0.1 - 0.3 eV were indicated.

The Boltzman plot was not a good method for determining Te for two reasons. Firstly, the slope of the straight line given by eq. 7.7 is not very sensitive to the temperature. The largest difference between the ionisation energies of any two upper states was about 0.5 eV and therefore the expression $[I\lambda/gA]$ changed at the most by a factor of 1.6 for a change in T_e of 1 eV to 0.5 eV. Secondly, there were considerable errors involved in measuring the intensities of the lines. The detecting system was calibrated for the wavelength range of interest using a tungsten standard lamp. It was difficult to estimate the magnitude of the errors

incurred in this procedure. However, a 2% error in measuring the lamp current leads to an error in the lamp temperature of about 10% and hence could have contributed significantly to the poor results. Similar errors occur in the measurements of I. These were most severe for the higher series members, n = 6, 7, where the lines were very weak. It is, nevertheless, difficult to explain why the experimental points were so random. The insensitivity of the method should have tended to put all points on a straight line rather than distribute them well to each side and so this method had to be abandoned.

THE CONTINUUM SLOPE

The dominant mechanism for the production of continuum radiation by the plasma was electronic recombination. The continuum intensity may be then written as

$$I_c \propto e^{-h\nu/kT}$$

A plot of $\ln I_c$ against ν produces a straight line of gradient $-h/kT$.

The continuum intensity was very weak in the plasma afterglow and to obtain a signal the entrance and exit slits of the

monochromator were opened up to 3Å. This increased the probability of observing an impurity line with the continuum and large regions of the spectrum were examined to find suitably impurity free continuum areas. Again, the results were very poor. Values of T_e deduced ranged from about 0.8 eV to small negative temperatures. This method, as the previous one, entailed the calibration of the spectral response of the detecting system. It suffered also from even greater difficulties with low intensity signals and consequently possible distortion by impurities. Finally, the sensitivity of the straight line gradient was low. A change in T_e from 1eV to 0.5eV produced again a change in the gradient of the plot of a factor of only 1.6. This method, too, was rejected as being insufficiently accurate.

RELATIVE LINE TO CONTINUUM RATIOS

The ratio between the total integrated intensity of a line and the continuum intensity under the line has been given by Griem (1964) as

$$\frac{I_l}{I_c} = \frac{3^{3/2}\pi^3(137a_0)^2 f g \exp[(E_\infty - E_i)/RT]}{2\lambda\Delta\lambda\, g_i[(g_{ff}/2)(RT/E_H)\exp(E_H/n^2RT) + \sum_n g_{fb}/n^3 \exp(E_H/n^2RT)]} \qquad 7.8$$

E_∞ is the ionization potential of helium, E_H the ionization potential of hydrogen, E_i the energy of the lower state of the line, g the statistical weight of the lower state and g_{ff}, g_{fb} the free-free and free-bound gaunt factors.

Eq. 7.8 is valid for temperatures up to 30,000°K and requires that the upper state is in LTE with the free electrons. As mentioned before, the latter restriction eliminates all lines for which $n < 4$. Two lines were chosen to evaluate Te. The $2^3P - 4^3S$ at 4713Å and $2^1P - 5^1S$ at 4437Å. These lines were scanned, the scan continuing beyond the far line wings to determine the background continuum intensity. There was considerable scatter in the magnitude of the latter representing an uncertainty in the continuum intensity of 40% but this led to uncertainties in Te of only 20%. The ratio I_l/I_c was calculated for a section of continuum 100Å wide centred on the line; that is, $\Delta\lambda$ in eq. 7.8 was taken to be 100Å. Eq. 7.8 was then evaluated for the two lines over a range of electron temperatures 0.3eV - 1.5 eV and values of Te determined from the measured ratio I_l/I_c. The results from the two lines are shown in Fig. 7.1 at various times in the plasma decay. It can be seen that the two sets of temperatures agree to within experimental error and also lie within the range of atom temperatures.

The line to continuum ratio method of measuring Te has several advantages over the two methods described previously. Firstly, there is no necessity to calibrate the spectral response of the detecting system as this may be considered constant over the small wavelength range of 100Å. Secondly, the ratio I_l/I_c is very sensitive to the temperature. A change of a factor of two in Te corresponds to a factor of ten change in I_l/I_c in the temperature region of interest. This meant that although difficulties still arose in measuring the continuum intensity, the calculated temperature was not strongly effected.

Finally, it should be re-emphasised, that the profiles of 4471 and 4922 are not very dependent on Te. This point will be discussed more fully in a later chapter on the possible sources and effects of errors arising in the experiment.

CHAPTER 8

THE EFFECT OF RADIAL DENSITY GRADIENTS ON THE LINE PROFILES

Jenkins (1970) has observed that radial density gradients in the plasma can dominate the relative intensities and shapes of the allowed and forbidden components of 4471 and 4922. This occurs because of the great sensitivity of the forbidden component to the electron density. If the total observed light is emitted by two or more regions of the plasma, each region having a different electron density, then the observed profile is a sum of the profiles emitted by each separate region. Working in the regime $n_e \sim 10^{16} - 10^{17}$, Jenkins has shown that by using an experimentally reasonable model of the plasma, profiles can be predicted which do not correspond to the profiles expected from a

homogeneous plasma. Using this technique, he can account for discrepancies between his observed profiles and those predicted by theory. In the present work, where $n_e \sim 10^{14} - 10^{15}$, and when interest lies in the plasma afterglow, the plasma can be expected to be comparatively homogeneous. However, an estimate has been made of the effect of radial gradients.

This was done in three ways, First, a system of variable apertures was placed between the plasma and the monochromator so that different regions of the plasma were studied. Secondly, a comparison was made between profiles taken in the end-on position and the side-on position where the weighting associated with radial zones was different. Thirdly, a theoretical model of the plasma was constructed and the profiles predicted from the model compared with experimental profiles. These three considerations will be discussed in the following sections.

APERTURES IN THE END-ON POSITION

Fig. 8.1 shows the optical arrangement used to observe light from various sections of the plasma.

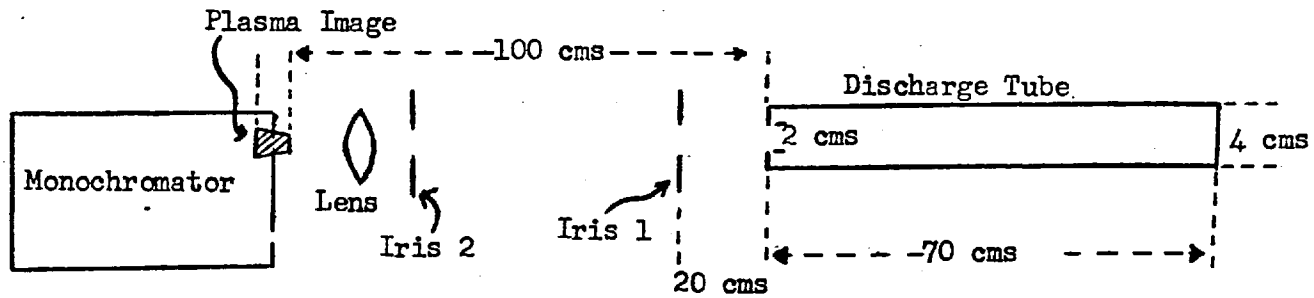

FIG. 8.1 Diagram of optical system used to discriminate against outer zones of plasma

It was not possible to focus exactly the whole of the plasma onto the entrance slit of the monochromator because of the large length of the discharge tube. The system shown in Fig. 8.1 produced an image of depth of focus of about 5 cms. and magnification $\frac{1}{2}$ for the near end of the tube and $\frac{1}{4}$ for the far end. The slit height could be reduced so as to descriminate against the outer radial zones of the plasma. This is shown in Fig. 8.2

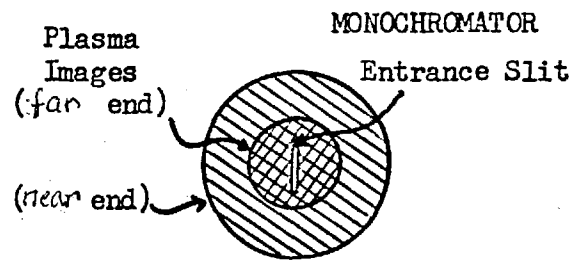

FIG. 8.2 Formation of Images of Plasma on Monochromator Entrance Slit

A similar effect can be achieved by varying the diameter of the two irises shown in Fig. 8.1. This was carried out, varying the diameter between 0.5 cm. and 3 cm. but always keeping the diameter of each iris the same. At the larger diameters, the iris no longer provided the limiting aperture of the system (this point will be discussed later in this chapter). Fig. 8.3 shows the regions of the plasma which could radiate into the monochromator through the iris system.

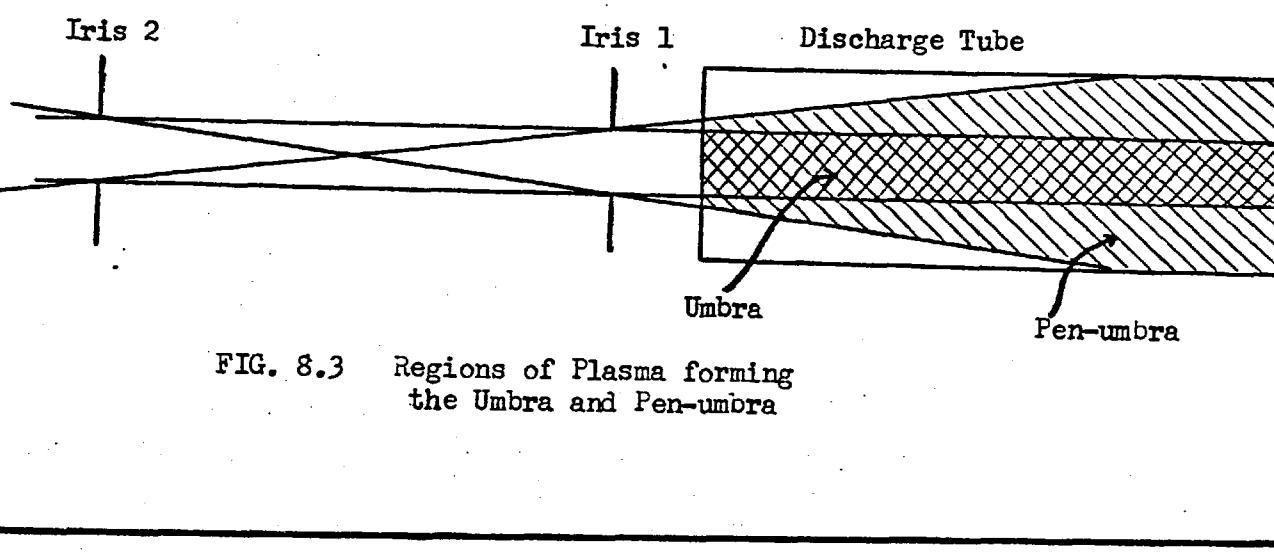

FIG. 8.3 Regions of Plasma forming the Umbra and Pen-umbra

The observed plasma may be divided into two parts. (a) an umbra which was a cylinder of plasma lying on the central axis of the tube and of the same diameter as the iris. The solid angle into which an element of plasma lying in this region could radiate was limited by iris 2 only. (b) A pen-umbra, constructed in the usual way. The solid angle into which elements in this region could radiate into was more complex but the exact weighting which ought to be given to such elements was not important in the pr esent instance.

Measurements were made varying not only the aperture diameters but also the entrance slit height. These consisted of measuring the ratio of the peak heights of the allowed and forbidden

components of both 4471 and 4922. This was a very sensitive test. More so than comparing the total intensities because light from lower electron density regions produced not only a relatively smaller forbidden component, but also a narrower profile and therefore the change in intensity at the line peak was more pronounced than the change in the total intensity. The results showed no difference in the ratio when the whole or only part of the plasma was viewed. Therefore, the emission from the outer, lower electron density regions was not sufficient to distort the profiles emitted from the central regions of the plasma.

SIDE-ON PROFILES

In the side-on position, each radial zone of the plasma had a weighting factor of r^2 (where r is the radius of the zone) associated with it. Furthermore, in this position the depth of the plasma was small (4 cms.) compared to typical distances in the optical arrangement and therefore all elements of plasma in view radiated into the same solid angle. There was no question of umbras and pen-umbras to reduce the effect of the outer regions of the plasma. It was hence expected that the effects of radial gradients would be far more pronounced in the side-on position

than in the end-on position. Again, the ratio, R_{pk}, of the allowed to forbidden peak intensities was measured and found to be greater by nearly a factor of two in the side-on positions. The measurements were repeated with the addition of a horizontal aperture placed over the discharge tube. This is shown in Fig. 8.4.

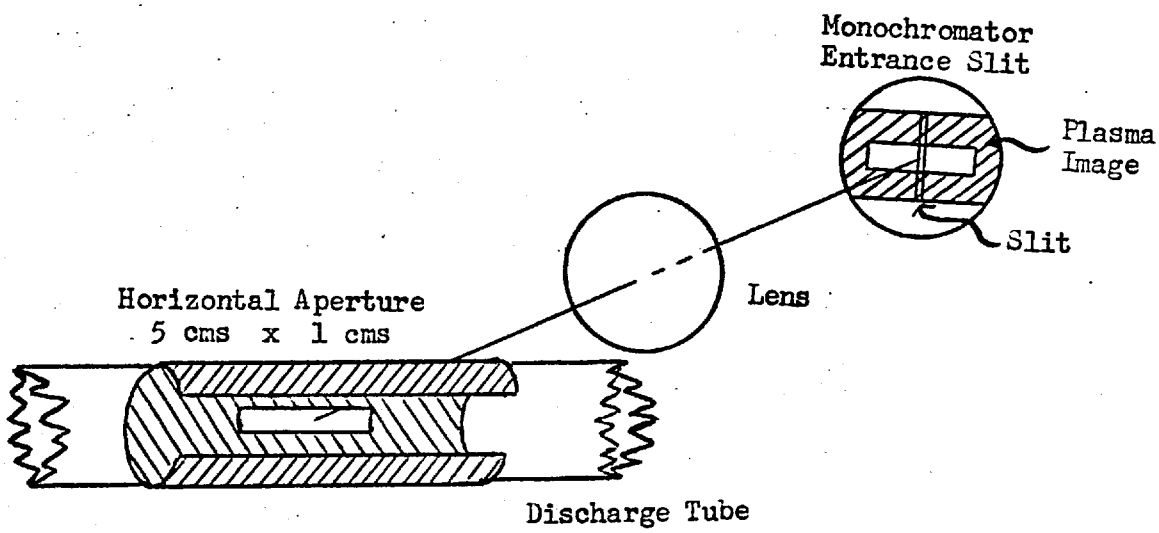

FIG. 8.4 Horizontal Aperture used in front of Discharge Tube when viewed the side-on position

The effect of the aperture was to remove the r^2 weighting from the radial zones. Now, only elements lying on a slice of plasma passing through a diameter of the tube could radiate into the monochromator. Measurements of R_{pk} showed it to be a little lower than the no aperture case but considerably higher than the

end-on position. These results will be considered quantitively later in this chapter.

THE PLASMA MODEL

There were three considerations to be taken into account in constructing a model of the plasma. The most important of these, at least in the end-on case, arose from the geometry of the discharge tube and optical system. Elements of plasma at the far end of the tube subtended a smaller solid angle at the monochromator entrance slit than elements at the near end. Also, off axial elements were wholly or partially vignetted by the electrode assembly and lens. These considerations were accounted for by dividing the plasma up into a number of sections and giving each section a weighting factor determined by its position in the tube. In calculating the weighting factors, the aperturing effect of the entrance slit itself was not considered. In fact, the slit would discriminate heavily against the outer zones of the plasma. This was because the slit height was 5 mm. and the size of the plasma image on the slit lay between 10 mm. and 20 mm. depending on which part of the plasma was being considered. Hence, only the central region, of diameter 1 cm. to 2 cm, could radiate into the

monochromator. Fig 8.5 shows the geometry used to calculate the various weighting factors and the sections into which the plasma was divided.

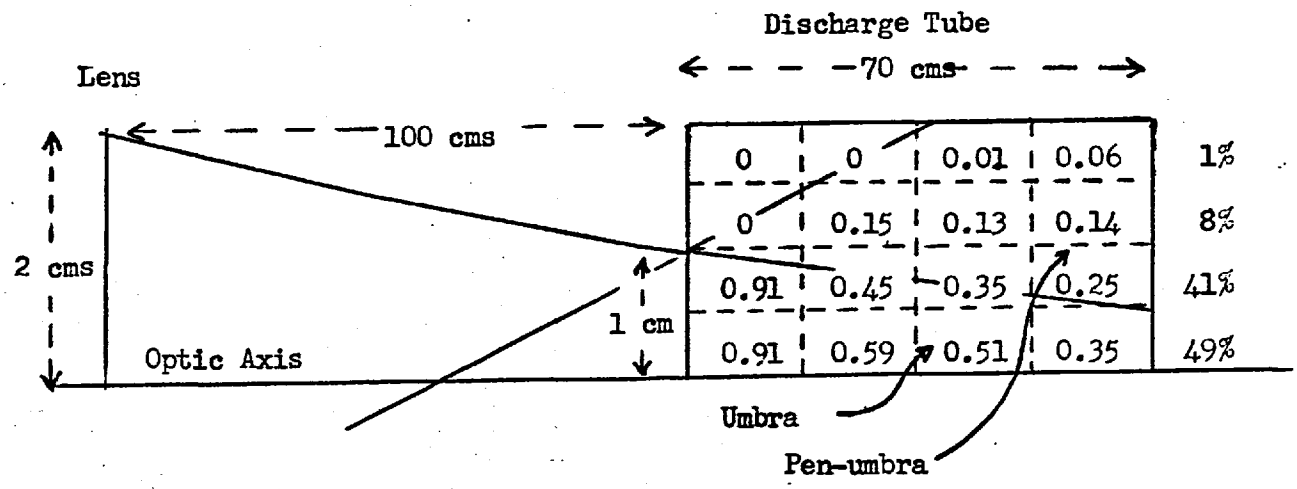

FIG. 8.5 Weighting Factor associated with each section of Plasma

The limiting apertures in Fig. 8.5 were provided by a 4 cm. diameter lens 100 cms. away from the front of the plasma and the 2 cm. diameter quartz insert forming the front boundary of the plasma. The sixteen small elements were evenly distributed throughout the discharge tube and were taken as representing the whole of the plasma. The column of numbers at the right hand side of Fig. 8.5 is the volume of weighted plasma, expressed as a

percentage of the whole, for each radial zone and it can be seen that 90% of the effective plasma lies in a central column of 1 cm. radius.

The choice of a model of the density gradient was to a certain extent arbitrary. Gerardo (1969) has measured density gradients in the afterglow of a plasma very similar to the present one except that the diameter of his tube was $\frac{1}{2}$ that of the present tube. Gerardo's gradients can, therefore, be expected to be more severe than those anticipated here. Furthermore, experiments to measure the density gradients (see Chapter 6) have shown that to within experimental error, the plasma was homogeneous in a central column 2 cm. diameter. Therefore a model was chosen such that the central region, a 2 cm. diameter column, was assumed to have a homogeneous density of 10^{15} and the remaining parts of the plasma were assumed to be 3.10^{14}. The latter figure almost certainly over-estimated the slope of the gradient and the results could be expected to err on the pessimistic side.

Finally, an emission coefficient was chosen for each zone. That is, the outer, low density zone was assumed to emit less light/solid angle/volume than the high density zone. An estimate of the coefficient was made from the total intensity of 4471

emitted by the whole plasma at densities of 10^{15} and 3.10^{14}. At the lower density, the total emission was less by a factor of three than at the higher density. The outer region was therefore weighted by a further factor of $\frac{1}{3}$.

With this model, the values of R_{pk} have been calculated in various conditions. (a) In the end-on position assuming no apertures other than those shown in Fig. 8.5. (b) In the side-on position with no apertures. (c) In the side-on position with the horizontal aperture which removed the r^2 weighting factor from the radial zones. These values have been compared to measured values in Table 8.1

		EXPERIMENTAL	CALCULATED
End-on		15	12.5
Side-on	No aperture	21	23.9
	Aperture	21	18.9

TABLE 8.1.

The conclusion which can be drawn from Table 8.1 is that the plasma model overestimated the contribution of the outer regions of the plasma to the line profiles. This can be seen by observing that the more weight that is given to the radial zones in the calculations, the larger is the disagreement between theory and

experiment. (The theory-experiment disagreement in the end-on position does not necessarily imply that the model is wrong. It will later be postulated that it is the calculated profiles of BGS and Griem which account for this discrepancy.) The fact that the ratio R_{pk} increases faster for the calculated values than for the experimental values as the radial weighting increases, indicates that the model was too severe. Further calculations were made for R_{pk} assuming that the whole of the plasma was at an electron density of 10^{15}.

$$R_{pk}\,[\text{end-on, using model}] = 12{\cdot}5$$

$$R_{pk}\,[\text{assuming } 10^{15} \text{ for whole plasma}] = 11{\cdot}8$$

This is a difference of only 6% and, even so, is an overestimate of the true difference.

The evidence against the distorting effect of radial density gradients may be summarised as follows. The use of a system of apertures, which could discriminate heavily against non-central regions of the plasma, produced no variations in R_{pk}. Also a model plasma has been constructed, which has been shown to over-emphasise the effect of radial density gradients, and can still account for a change in R_{pk} in the end-on position of only 6%

from a homogeneous plasma. Electron density gradients were therefore assumed to be negligible. Temperature gradients were also ignored as being considerably less important than electron density gradients.

AXIAL DENSITY GRADIENTS

No experimental work has been done on the present apparatus to investigate the effects of axial electron density gradients. However, Burgess (1965) has made measurements of axial gradients on similar discharge. The dimensions of the discharge tube used in this work were 50 cm. length by 15 cm. diameter. Measurements were made at early times in the discharge when the plasma was compressed and typical electron densities were $\sim 10^{18}$. Even under these conditions, Burgess found that the density was constant to within a few per cent in the central half of the tube. In front of each anode, the density fell by 20% and then rose again to the value measured in the centre of the tube. The total length of the discharge over which the density varies by more than 10% was less than 20 cm. or 40% of the tube length. The axial gradients in the present work can be expected to be far

less than this for several reasons. First, the discharge was twice as long and $\frac{1}{4}$ of the diameter of that used by Burgess. Therefore the homogeneous central region was expected to be much longer in the present case and represent a larger fraction of the total tube length. Secondly, interest in this thesis has always been concentrated in the afterglow of the plasma when the pinched phase was over and the plasma has expanded to fill the whole tube. Under these conditions, gradients are much less pronounced than when the discharge currents are still flowing in the plasma.

Finally, radial gradients have been shown to be unimportant earlier in this chapter. Because of the dimensions of the tube, axial gradients must be less important than radial gradients and therefore they have been ignored.

CHAPTER 9

COMPARISON OF EXPERIMENTAL PROFILES WITH THEORY

Figs. 9.1 to 9.4 show the experimental profiles obtained superimposed on the theoretical profiles of Griem and BCS. Figs. 9.1 and 9.2 are 4471 at electron densities of 10^{15} and 4.10^{14}, electron temperatures 1.1 eV and 0.6 eV and atom temperatures 1.2 eV and 0.6 eV. The latter temperatures have a large uncertainty on them, i.e. $T_a \sim 1.4 - 0.8 eV$ in Fig. 9.1 and 0.5 eV - 0.7 eV in Fig. 9.2 Figs. 9.3 and 9.4 show 4922 at the same plasma parameters. In all cases, the dots represent experimental points corrected for self-abrorption and normalised to unit total area. The solid lines are theoretical profiles taken from BCS and the broken lines are the

HELIUM I 4471 Å

$N_e = 10^{15}$

$T_i = 13{,}000°$

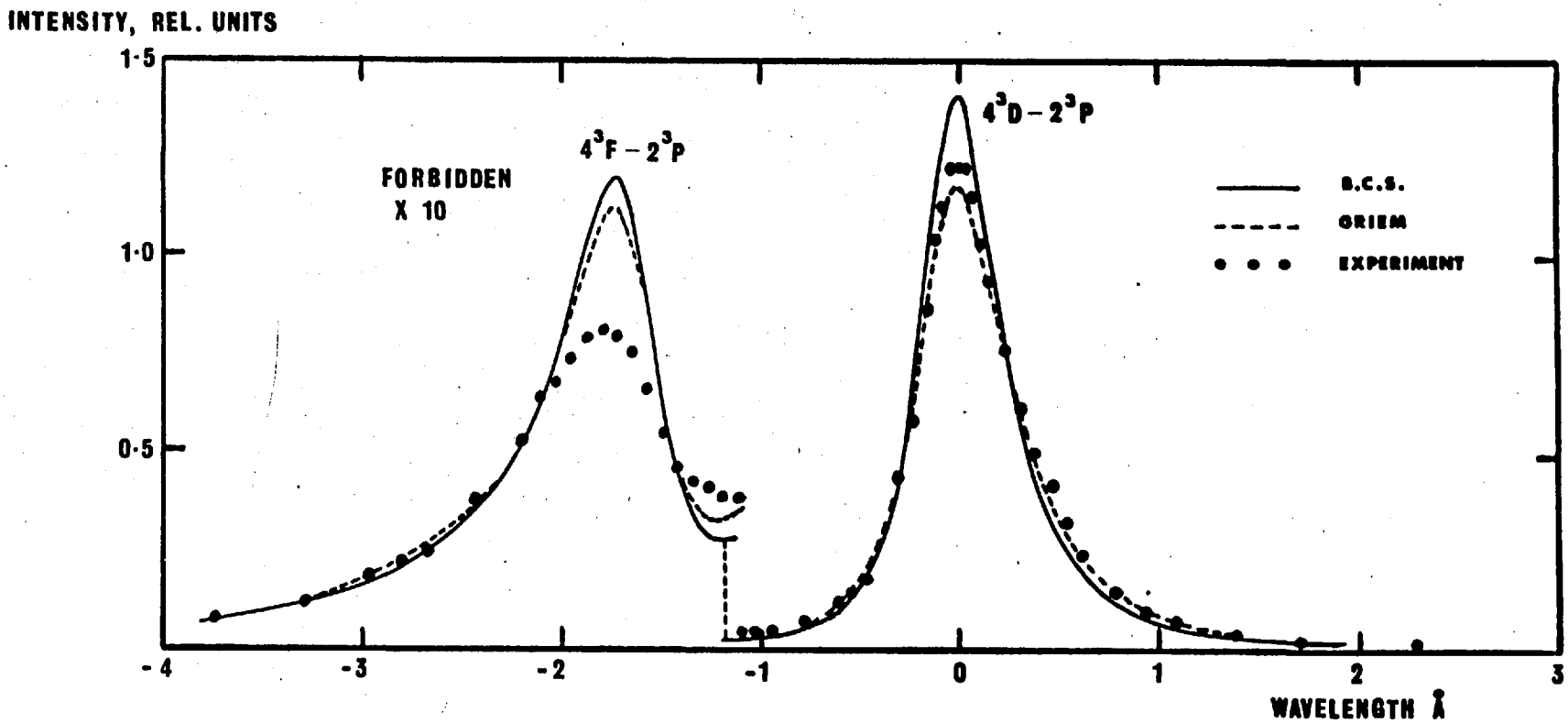

FIG 9.1

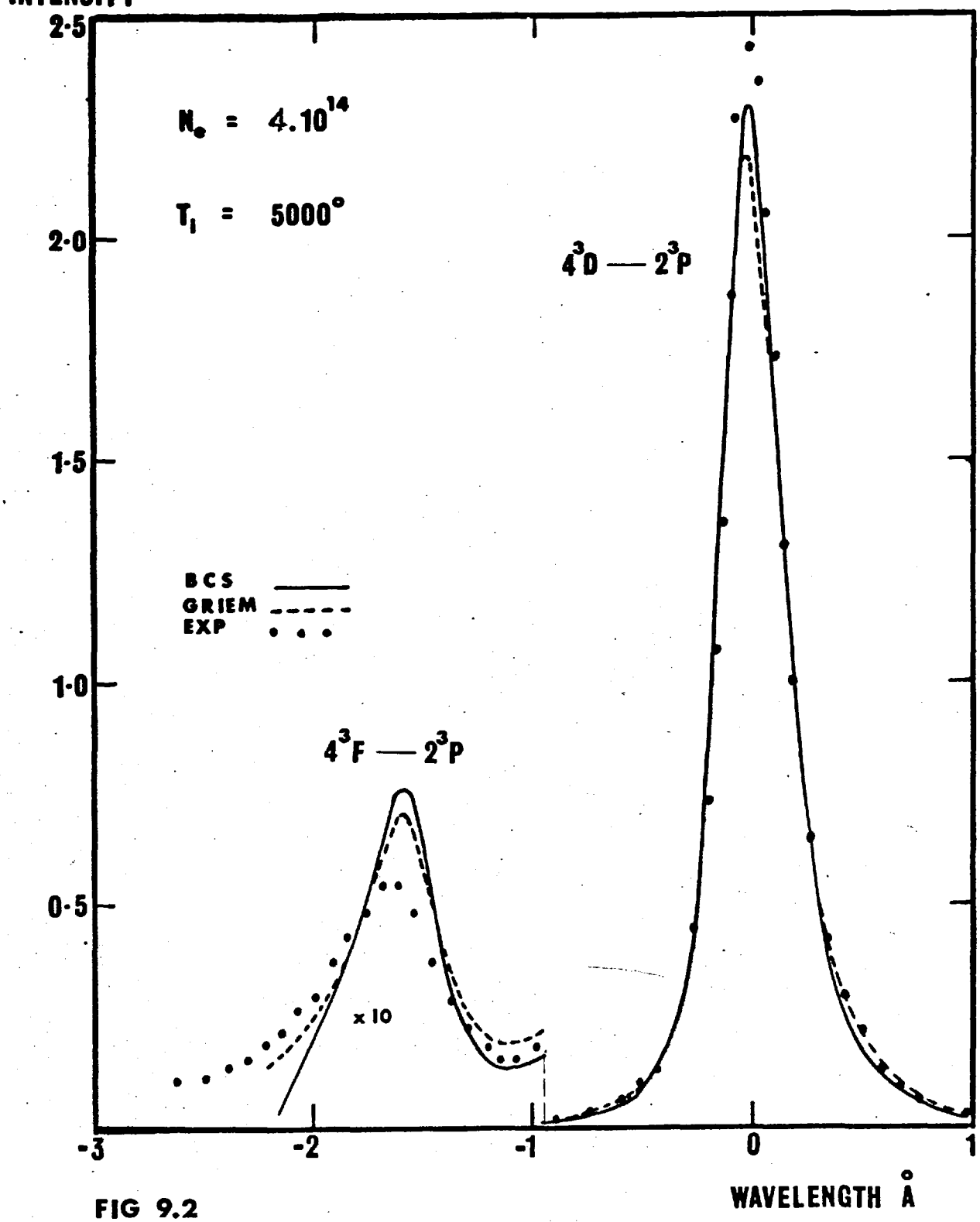
REL.
INTENSITY
HELIUM I 4471 Å
2·5
2·0
1·5
1·0
0·5
$N_e = 4.10^{14}$
$T_i = 5000°$
BCS
GRIEM
EXP
$4^3D - 2^3P$
$4^3F - 2^3P$
x 10
-3
-2
-1
0
1
WAVELENGTH Å

FIG 9.2

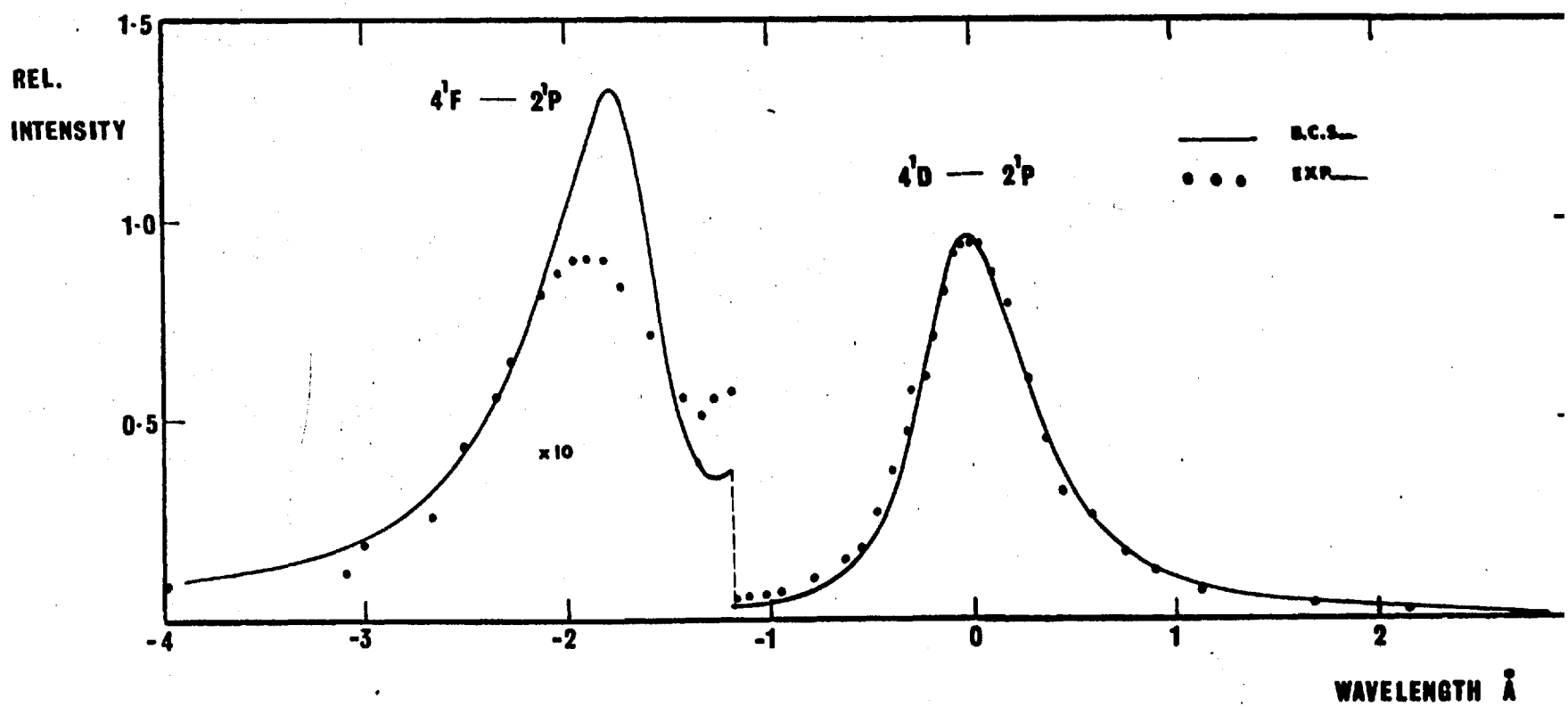
HELIUM I · 4921 Å
$N_e = 10^{15}$
$T_i = 13{,}000°$
REL. INTENSITY
1·5
1·0
0·5
$4^1F - 2^1P$
$4^1D - 2^1P$
B.C.S.
EXP.
x 10
-4
-3
-2
-1
0
1
2
WAVELENGTH Å

FIG 9.3

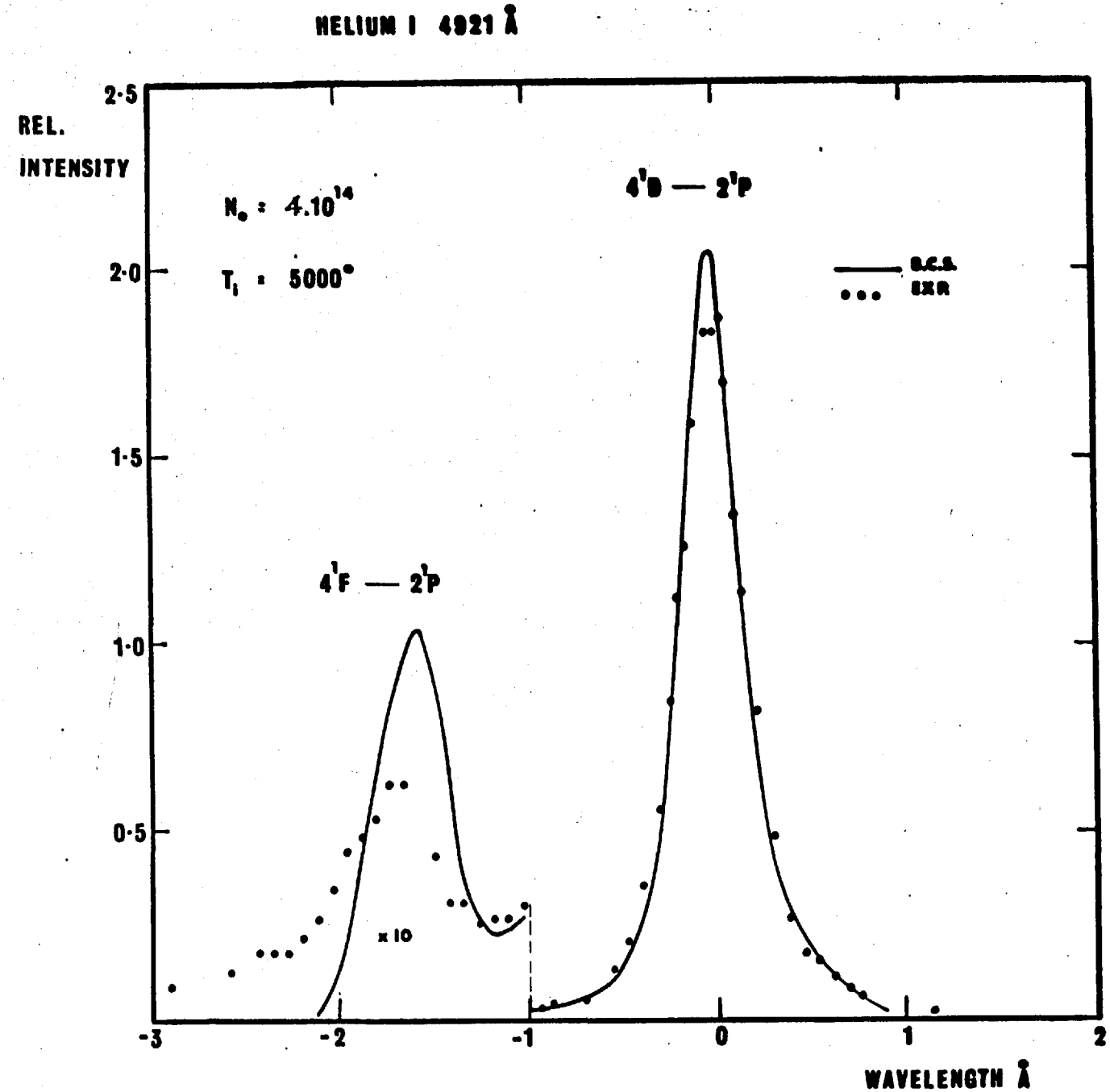
HELIUM I 4921 Å
REL.
INTENSITY
2·5
2·0
1·5
1·0
0·5
N_e = 4.10^{14}
T_i = 5000°
$4^1D - 2^1P$
B.C.S.
EXP
$4^1F - 2^1P$
x 10
-3
-2
-1
0
1
2
WAVELENGTH Å

FIG 9.4.

profiles of Griem. Both Griem's and BCS's profiles have been convolved with the instrument profile and then normalised to total unit area. The temperatures associated with the theoretical profiles are those nearest to the experimental conditions, i.e. electron, atom and ion temperatures are assumed to be equal and $T = 10{,}000^{\circ}K = 0.86$ eV at the higher densities, $T = 5{,}000^{\circ}K = 0.43$ eV at the lower densities. The theoretical profiles at $n_e = 4.10^{14}$ were constructed by graphically interpolating between the densities $n_e = 10^{14}, 3.10^{14}, 10^{15}$ which has possibly led to errors in the profiles in the wing of the forbidden component. Finally note that all forbidden lines are magnified by a factor of 10 and that Figs. 9.3 and 9.4 do not show a theoretical profile by Griem as these have not been calculated. All profiles are normalised with respect to wavelength such that the peak intensities of the allowed lines coincide.

In all four cases, the fit between experiment and theory is excellent for the allowed line, especially in the red wing. Agreement is poorest at the line centre but even here, the discrepancy is less than 10% and, at least for 4471, is of the same order as the difference between BCS and Griem. On either side of the line centre, BCS, Griem and experiment are all in agreement to within, typically,

5%. At the higher densities, the fit in the blue wing of the forbidden line is also extremely good. For the lower densities there is large disagreement between theory and experiment though this is probably due to the difficulty in extracting accurate theoretical profiles in this region and is therefore not significant. For a meaningful comparison between theory and experiment here, the programmes of Griem and BCS would have to be run at $n_e = 4.10^{14}$.

The most interesting regions of the profiles are at the peak of the forbidden line and in the dip between the two lines. In all cases the experimental points lie 30% below the theory in the forbidden line core and between 30% to 10% higher in the dip. Burgess (1970a) has proposed that the tendencies for the forbidden line to be smeared out by cutting off the peak and filling in the dip are part of the same process. This will be discussed in the next chapter. It is sufficient to say here that the discrepancy between experiment and theory, consistently shown in these profiles, indicates a fundamental error in the theory of BCS and Griem.

DISCUSSION OF THE ACCURACY OF THE PROFILES

Before discussing the conclusions to be drawn from the experiment, it is important to establish the validity of the profiles.

This is basically determined by the accuracy with which the various plasma parameters have been measured. The effect of radial gradients has already been considered and shown to be negligible. Measurements of the electron density, plasma temperatures and optical depth will be investigated in the next three sections of this chapter.

DENSITY MEASUREMENTS

Fig. 9.5 shows the dependence of the ratio, R, of allowed to forbidden line intensities in the region $n_e \sim 10^{15} - 3.10^{14}$. The curve was constructed from the profiles of BCS at a temperature of 10,000°K and interpolated between electron densities of 10^{15} and 3.10^{14}.

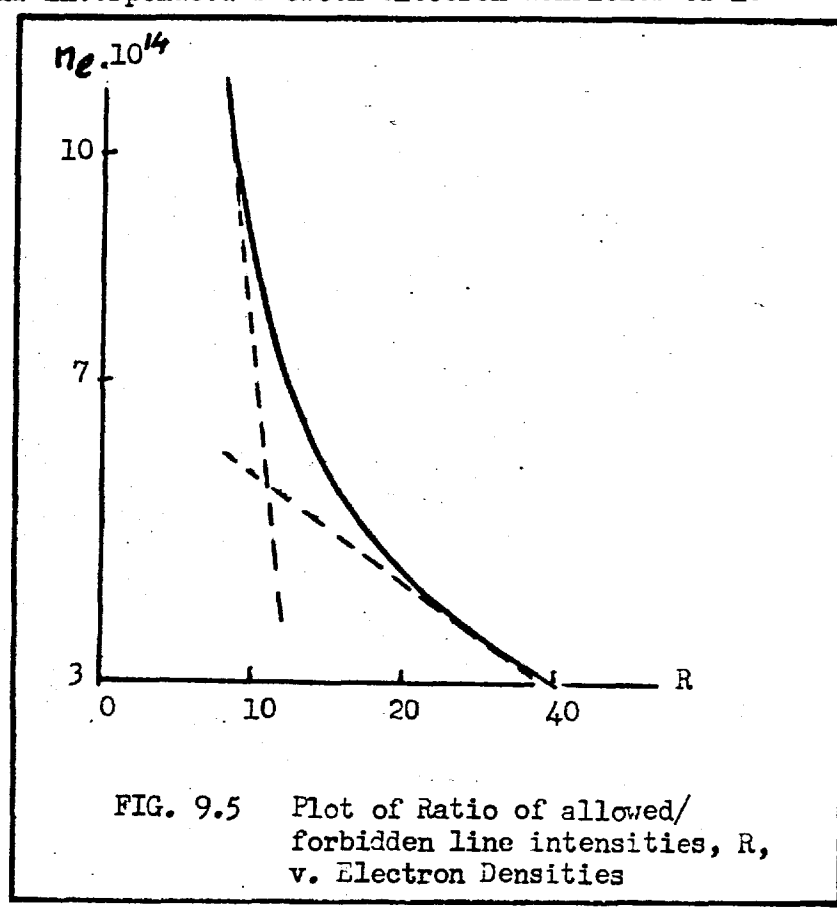

FIG. 9.5 Plot of Ratio of allowed/ forbidden line intensities, R, v. Electron Densities

For small changes in n_e, say $\Delta n_e \sim 10^{14}$, R is approximately a linear function of n_e and therefore the uncertainty in measured values of n_e would produce an uncertainty in R given by

$$1.8\,\frac{\Delta R}{R} \simeq \frac{\Delta n_e}{n_e} \quad \ldots\ n_e \simeq 10^{15} \qquad 9.1$$

$$\frac{\Delta R}{R} \simeq \frac{\Delta n_e}{n_e} \quad \ldots\ n_e \simeq 3.10^{14} \qquad 9.2$$

The discrepancy between the total intensities of the experimental and theoretical forbidden line is 15% for both 4471 and 4922 at $n_e = 10^{15}$. By eq. 9.1, the error in n_e, necessary to produce a 15% discrepancy, is 27%. The accuracy of the density measurements was limited by the uncertainty in the level of the zeroth fringe (see Chapter 6) and was better than $\pm$ 5%. This accuracy is well supported by the independent density measurements determined from the widths of H_β. These agreed with the laser results to about 7%. An error of 27% is therefore a factor of 4 - 5 greater than expected errors in the density measurements. Furthermore, if the density were reduced to make the ratio R agree with the theory, the half-width of the allowed line would decrease by 25% and the forbidden by a similar amount. At present, the half widths of the experimental profiles agree with the theoretical

profiles to within 10% at worst and to within 3% usually, at the higher densities. Clearly, if the electron number density is changed to bring about agreement between theory and experiment for the ratio R, then large discrepancies will appear in the half-widths and over the profiles in general.

Possible errors in the measurement of n_e are, therefore, unable to explain experiment-theory disagreement, because, not only is the required error in n_e far in excess of the expected errors but in any case such an error would increase rather than decrease the fit between experimental and theoretical profiles.

TEMPERATURE MEASUREMENTS

Large uncertainties exist in the measurements of the plasma temperatures. At $n_e = 10^{15}$ the temperatures lie in the following ranges $0.7eV \leq T_a \leq 1.2\,eV$; $0.7eV \leq T_e \leq 1.1eV$.

The atom temperature effects the profiles largely through the Doppler effect.

$$\Delta\lambda \simeq \left[\frac{RT}{4.7A} \cdot 10^{-8}\right]^{1/2} \lambda \qquad 9.3$$

$\Delta\lambda$ is the $1/e$- whole width of the line, in Å, A the atomic

Weight. For 4471 at $kT = 1eV$

$$\Delta\lambda \simeq 0.12\,eV.$$

The $1/e$-whole width including all broadening processes was $\sim 0.6\text{Å}$. Now if the atom temperature was increased by 30%, which was the magnitude of the error on Ta, $\Delta\lambda$ would increase by $\sim 15\%$ and the change in the width of the observed line would be only $\sim 2\%$. This is a negligibly small amount. The validity of the above agreement has been checked by numerically convolving experimental profiles with pure Gaussian profiles representing uncertainties in Ta corresponding to those expected from the temperature measurements. As predicted, no observable difference could be detected in the profiles before and after the convolution.

It was more difficult to calculate the effect of the electron temperature on the profiles. Instead an estimate was made by comparing the theoretical profiles of BCS at $n_e = 10^{15}$ and T = 5,000°K in one case and T = 20,000°K in the other. Here, T is the electron, atom and ion temperature all assumed to be the same and the profiles therefore contain the effect of both the electron temperature and the atom temperature. Fig. 9.6 shows the profiles obtained. There is very little difference between the two. The higher

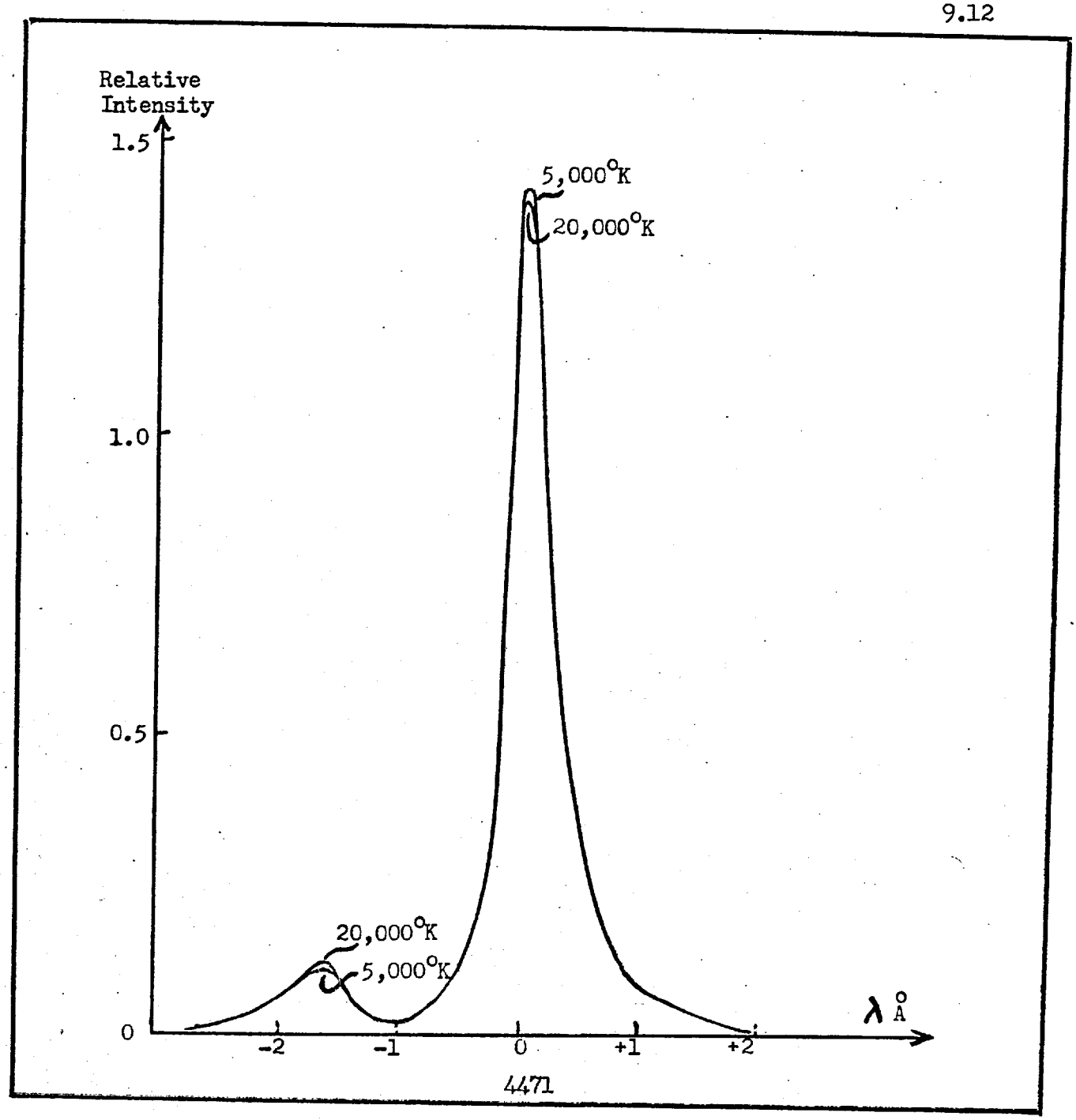

FIG. 9.6 Comparison of profiles of 4471 at $n_e = 10^{15}$, T = 5,000°K and 20,000°K taken from BCS. Where only only line is shown, the Profiles are indistinguishable.

temperature profile has a half-width which is 10% greater than the lower temperature profile and the peak intensities differ by only 3% for the allowed line and 5% for the forbidden line. These small differences arise in spite of the fact that the temperatures of the two profiles cover a range over 10 times that to be expected in the experimental profiles due to uncertainties in the measurement of T_e .

In conclusion, the profiles are so insensitive to temperature that even the large error bars on the temperature measurements do not produce an appreciable change in the final profiles.

ABSORPTION MEASUREMENTS

The line profiles have been corrected by multiplication with the factor

$$K_\nu = \left[\frac{\ln I_o/I_\nu^{obs}}{1 - I_\nu^{obs}/I_o} \right] = \ln R_\nu / [1 - R_\nu^{-1}] \qquad 9.4$$

where $R_\nu = I_o/I_\nu^{obs}$

In the line wings, where $R_\nu \simeq 1.1$, errors due to the correction procedure are clearly small. It was in the core of the line where the factor K_ν was large (1.2 - 2) that serious errors could arise. In the region of the forbidden line, $K_\nu = 1$ always and therefore it was particularly important to investigate possible errors in K_ν as these applied only to the allowed line and could strongly effect the allowed/forbidden intensity ratio.

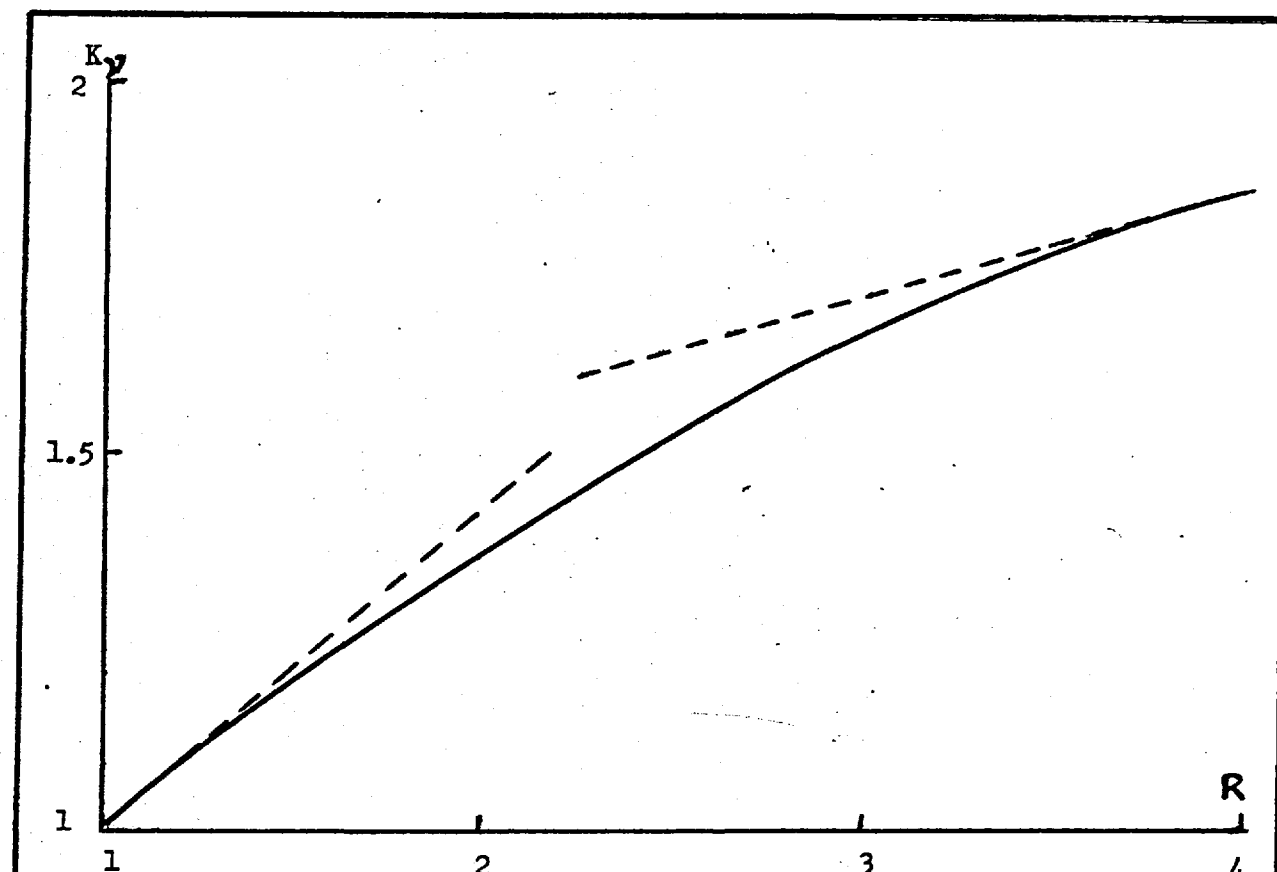

FIG. 9.7 Plot of Absorption factor, K_ν, v. Ratio $I_o/I_\nu^{obs} \equiv R$

Fig. 9.7 shows a plot of K_y v. R_y. The gradient, of the curve varies from 0.5 when R ~ 1 to 0 for R ~ ∞ . The range of experimental interest is $1 \leq R \leq 5$ and the corresponding range in the gradient was $0.5 \geq dK_y/dR \geq 0.15$. Hence, as R increases, K becomes less and less sensitive to R but counteracting this tendency is the fact that as R increases, the difficulty and errors in measuring R also increase. When R ~ 5, the error in R may be estimated at ~ 20%. The corresponding error in K was therefore ~ 3%. Errors in R occurred from two sources - (a) jitter in the intensity of the flash tube signal; (b) difficulty in measuring the height of the absorbed flash tube signal when absorption was heavy and the signal was not much larger than the photomultiplier noise and the thickness of the CRO trace. The errors due to (b) can be made arbitrarily small by increasing the size of the flash tube signal compared to the signal from the plasma itself. In the present operating conditions, R = 5 was about the largest degree of absorption which could be measured with any degree of accuracy.

Errors due to absorption may, therefore be estimated to be less than 5% over all parts of the profile. It is significant that the corrections differed by a factor of three between the two lines. Corrections on 4471 increased the total intensity of the allowed

line by typically 20% - 30% and those to 4922, by 6% - 10%. Yet both profiles showed the same theory-experiment discrepancy. Hence, it is impossible to explain the discrepancy in terms of the absorption corrections.

In conclusion, it can be said that errors in the plasma parameters cannot be reasonably expected to account for the discrepancy between theory and experiment. This is because not only are the uncertainties on the measurements far too low to do this, but even assuming they were much higher, the modifications they would make to the experimental profiles would not improve the theory-experiment fit. In the line wings, the fit is excellent and any change which could yield a fit at the forbidden line core would destroy the line wing fit.

It will be shown in the next chapter that the forbidden line core discrepancy can, at least qualitatively, be shown to be due to an error in the theory and that similar results by other authors can be explained in the same way.

CHAPTER 10

CONCLUSIONS AND FUTURE WORK

In the previous chapter, the experimental profiles have been presented and compared with the calculated profiles of BCS and Griem. Discrepancies have been shown to exist between theory and experiment in the region of the forbidden line centre and also it has been shown that these discrepancies cannot be explained in terms of experimental errors. In this chapter, possible errors in the theory will be examined.

Three aspects of the theory will be considered.

(a) The accuracy of the helium radial matrix elements.

(b) The accuracy of the ion-microfield distribution used in the theory.

(c) The validity of the quasi-static approximation used for the ions.

HELIUM RADIAL MATRIX ELEMENTS

The transition probabilities relevant in the present instance are the $4^3D - 4^3F$ and $4^1D - 4^1F$. These have been taken from the National Bureau of Standards report NRSDC-NBS4 where they are calculated in the coulomb approximation and are designated with and accuracy of B which means the accuracy lies in the range 3% - 10%. For the transition 4D - 4F, the accuracy lies at the lower end of this scale. This is because the two states involved are very nearly hydrogenic. GBKO have calculated the squares of the radial matrix elements $|\langle 4^3P|r|4^3D\rangle|^2$ using -

(a) effective principal quantum number
(b) effective charge
(c) hydrogenic approximation.

The results are listed below

	effect p.q.n.	effect charge	hydrogen
$\|\langle 4^3P\|r\|4^3D\rangle\|^2$	428·1	437·8	432
$\|\langle 4^1P\|r\|4^1D\rangle\|^2$	435·9	433·0	432

For the triplet system, the results agree to within 3% and to within 1% for the singlet system. The 4D - 4F system is more hydrogenic than the 4P - 4D and therefore the radial matrix

matrix elements will be more accurate. Even if the large errors in the radial matrix elements could be justified, it would still be impossible to account for the theory-experiment discrepancies. This is because the radial matrix elements effect not only the forbidden line intensity but also the half width of the forbidden line.

Therefore, if the matrix elements used by BCS and Griem were reduced to bring the peak intensity of the theoretical forbidden line into agreement with experiment, the good experiment-theory fit in the forbidden line blue wing would be lost. In fact, the theoretical forbidden line , which is already narrower than the experimental forbidden line, would become even narrower and the overall theory-experiment fit would be very poor.

THE EFFECT OF THE ION-MICROFIELD ON THE INTENSITY OF THE FORBIDDEN COMPONENT.

In chapter 2, the accuracy of the ion fields used by Griem and BCS were discussed and it was shown that when α, the ion-correlation parameter, = 0.3, the difference between the fields of Hooper and Mozer and Baranger was negligible. The strength of the forbidden line may be related to the allowed line by eq. 10.3 (see Griem 1964).

$$|d_{\alpha'\beta}|^2 \simeq \tfrac{1}{3}\left[\frac{4\pi\epsilon_0\hbar}{me}\right]^2 \left|\frac{\langle\alpha'|R|\alpha''\rangle}{\omega_{\alpha\alpha'}}\right| F^2 |d_{\alpha''\beta}|^2 \qquad 10.3$$

$d_{\alpha'\beta}$ and $d_{\alpha''\beta}$ are the dipole moment operators of the allowed and forbidden lines respectively and F is the ion field strength. Hence, the ratio of the intensities of the allowed to forbidden lines is proportional to the square of the ion field. Clearly, for errors in F of the order of 2%, the ion field may be ignored as a possible source of error.

THE VALIDITY OF THE QUASI-STATIC APPROXIMATION

The criterion used to determine the regions of validity of the quasi-static approximation is

$$\Delta\omega\Delta t \simeq 1 \qquad 10.4$$

Here, Δt is a typical ion collision time and $\Delta\omega$ defines a point on the line profile of separation $\Delta\omega$ from the line centre.

In the experiment described in this thesis, the quasi-static approximation is valid for the ions for points on the line greater than about 0.1Å separation from the line centre if the above criterion is used. The forbidden line is separated from the allowed line by 1.8Å in experimental conditions and therefore lies well within the quasi-static regime for the ions. This is the assumption made by both Griem and BCS throughout their calculations.

However, Burgess (1970b) has made an objection to the way in which Griem and BCS have applied eq. 10.4. Burgess argues that $\Delta\omega$ should be measured from the line centre only when the line in question is isolated. When a forbidden

component is present, the auto-correlation function of the complete profile can be approximately represented by a Lorentzian of the form -

$$C(t) = I_1 e^{-\gamma_1|t| + i\omega_1 t} + I_2 e^{-\gamma_2|t| + i\omega_2 t}$$

10.5

Where γ_1 and γ_2 are the half widths of the allowed and forbidden line respectively. Clearly, if the forbidden line is being considered, then $\Delta\omega$ should be measured, not from the centre of the allowed line, but from the centre of the forbidden line. This means that the quasi-static approximation is not valid for the ions in a range of 0.1Å in either side of the centre of the forbidden line under experiment conditions (ie. $n_e = 10^{15}$; $T \simeq 1\,eV$.). Figs. 9.1 - 9.4 show that the largest theory-experiment discrepancies appear near the forbidden line centre, the experimental profile being $\sim$ 30% lower than the theoretical profile. The next section of the thesis will discuss the effects of ion motion on the forbidden line.

THE TYPES OF COLLISION WHICH MUST BE CONSIDERED

There is, at the moment, no theory capable of treating the failure of the quasi-static approximation at the forbidden line centre. The types of collisions which such a theory must deal with are described below.

At the allowed line centre, the quasi-static approximation is invalid but the ions may still be treated in the adiabatic approximation. GBKO (1961) have calculated the profiles of isolated lines using the adiabatic approximation for the ions at the line centre and found that almost the same result is obtained as when the quasi-static approximation is used everywhere. At first sight, it would therefore seem that the same result would apply at the forbidden line, i.e. the adiabatic approximation would be valid at the forbidden line centre and would yield the same result as the quasi-static theory. However, this is not the case. The reason is, as pointed out by Burgess (1970b), that non-adiabatic ion collisions become important at the forbidden line centre. This can be seen by considering the energy transfer involved in a collision. It is easier to consider collision processes in absorption and reference will be made to fig. 10.1.

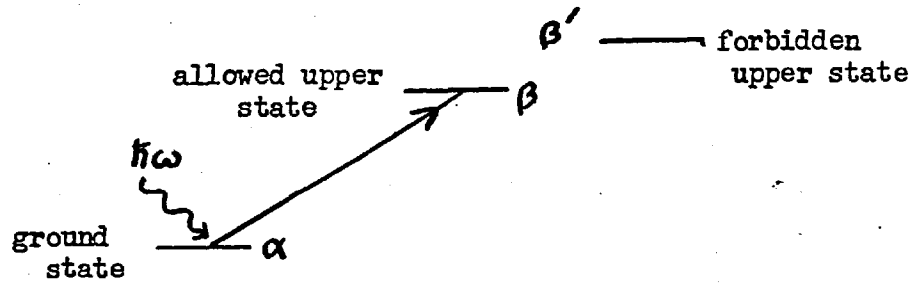

FIG. 10.1 Energy level diagram for line with Forbidden Component

For a non-adiabatic collision, there is a change in the atomic state during the collision. The equation of energy conservation can then be written,

$$\hbar\omega - [E_{\alpha\beta} + E_{\beta\beta'}] = \Delta E$$

ΔE is the energy transferred to the atom by the perturber and raises the atomic state from the upper state of the allowed line to the upper state of the forbidden line. At the allowed line centre, $\hbar\omega = E_{\alpha\beta}$ and hence $\Delta E = E_{\beta\beta'}$. But at the centre of the forbidden line, $\hbar\omega = E_{\alpha\beta'} = E_{\alpha\beta} + E_{\beta\beta'}$ and therefore $\Delta E = 0$. This position is reversed in the case of an adiabatic collision when no change in the atomic state occurs. Now, absorption of a photon, $\hbar\omega$, raises the atom from the ground state to β. This process is not energy conserving until a collision occurs and may be represented by —

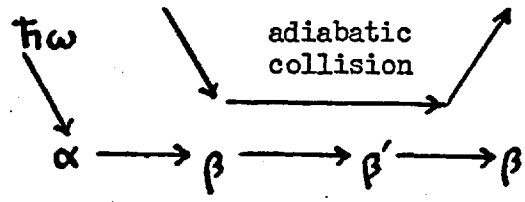

Clearly, if $\hbar\omega = E_{\alpha\beta}$, (i.e. in the allowed line centre), the energy transferred by the perturber is zero. Similarly, in the forbidden line centre, $\hbar\omega = E_{\alpha\beta} + E_{\beta\beta'}$ and $\Delta E = E_{\beta\beta'}$. These results are summarised below.

	Adiabatic	Non-adiabatic
ALLOWED LINE	0	$E_{\beta\beta'}$
FORBIDDEN LINE	$E_{\beta\beta'}$	0

TABLE 10.1 Energy transfer in Adiabatic and Non-adiabatic collisions

It can be seen from table 10.1 that non-adiabatic collisions have a resonance at the forbidden line centre because of the zero energy transfer at this point.

Furthermore, the non-adiabatic collisions are lower order perturbation expansion terms than the adiabatic collisions. The strength of the former have a $1/r^2$ dependence and the latter, a

$1/r^4$ dependence and therefore adiabatic collisions are very short range effects. On the other hand the non-adiabatic collisions are long range collisions and therefore overlapping in time.

A full treatment of these terms must, therefore, consider not only the ion dynamics, but also non-adiabatic overlapping ion collisions.

SOME PREDICTED EFFECTS ON THE PROFILES

Although no theory exists capable of fully accounting for the collisions just described, some qualitative results can be predicted. These may be divided into two aspects. First, the effects on the line shape and Second, the effect on the total relative intensity of the forbidden line must be considered.

The first effect can be deduced by analogy with the electrons. The effect of the electrons is to broaden the forbidden line and contribute to the intensity in the region between the two peaks. Similarly, when the ions are treated in the impact approximation a further broadening of the forbidden line is to be expected and, again further intensity will be added between the peaks. Therefore, the peak intensity of the forbidden line will be reduced below the theory of Griem and BCS and the dip intensity increased.

This has been experimentally observed and can be seen in Figs. 9.1 - 9.4. The reduction in the peak intensity is about 30% in all cases and the increase in the dip varies from 0 - 20%. For $n_e = 10^{15}$, the experiment-theory fit in the forbidden line blue wing is within 2-3%. A simple broadening effect on the forbidden line would not yield such a good fit on the wing and it is therefore necessary to postulate that a complete theory broadens the line towards the red wing only.

It is interesting to note that a correction, somewhat analgous to that suggested by Burgess (1970b), has been applied on more empirical grounds, by Hindmarsh and Farr (1969) to spectral lines broadened by the presence of a foreign gas. Such lines are known to show satellites in both red and blue wings. Previously, the satellite profiles have been calculated assuming the quasi-static approximation for the gas perturbers. Hindmarsh and Farr have taken into account the motion of the perturbers by broadening the red satellite with a Lorentzian of half-width γ, where γ is related to the life-time of a particular perturber configuration. A further paper, by McCartnan and Hindmarsh (1969) presents a measured profile of the red satellite of potassium 4047Å broadened by Krypton, together with a theoretical profile based on

the model of Hindmarsh and Farr. Agreement between the two is never worse than 95%. The relevant conclusion here is that the perturber may not always be treated by the quasi-static approximation in the region of a satellite or forbidden line. In these regions, $\Delta\omega$ must be measured from the forbidden line or satellite centre and a correction for the perturber motion may be necessary. A suitable way of making this correction for the potassium satellite was found to be to broaden the satellite which is just the effect already discussed.

It is difficult to make predictions concerning the relative intensity of the forbidden line when the ion motion is added to the theory. In the GBKO theory, the forbidden line is assumed to be caused by the ion-microfield exclusively, apart from a negligible contribution caused by non-adiabatic electron collisions which has been discussed by Burgess (1970) and Voslamber (1969). Non-adiabatic ion collisions can also contribute to the forbidden line intensity. The mechanism is simply that described earlier in this chapter. The zero energy transfer for a non-adiabatic collision at frequencies corresponding to the forbidden line centre induces some intensity in the forbidden line though this is likely to be a small effect. A further effect may be expected. The

inclusion of non-adiabatic collisions implies that adiabatic effects should be reduced and it is essentially the adiabatic effects which are mainly responsible for producing the forbidden line. Therefore, a reduction in the total forbidden line intensity would be predicted. It is difficult to assess the relative magnitude of the two contributions. Experimentally, the profiles of 4471 and 4922 at $n_e = 10^{15}$ show a decrease in the forbidden line intensity compared to the theory of about 10%. At the lower density, $n_e = 4.10^{14}$, the blue wing of the theoretical forbidden line has a large uncertainty on it arising from the interpolation technique used to extract the profile from tabulated profiles and it is therefore difficult to make a direct experiment-theory comparison. However, by using eq. 10.3, the ratio of the allowed to forbidden intensities can be calculated. When this is done, the experimental forbidden line is again less by about 10% compared to the theoretical line.

It should be pointed out here that the theory-experiment discrepancies described above will be much more apparent at low electron densities, i.e. $n_e = 10^{14} - 10^{15}$. Burgess (1970b) has explained the reasons for this. Firstly, at high densities, $n_e \sim 10^{17}$, the forbidden line saturates and therefore its

intensity becomes insensitive to the plasma conditions. Secondly, the half-width of the forbidden line increases more rapidly than the regime over which the quasi-static approximation is invalid. Therefore, a smaller fraction of the forbidden line is effected by the breakdown of the quasi-static approximation and its total effect becomes relatively smaller. It is therefore only at low densities, those of astrophysical interest, that the discrepancies will readily be observable.

RECENT EXPERIMENTAL PROFILES OBTAINED FROM STELLAR SOURCES

Underhill, Johnson and Poland, and Kodaira and Scholz have recently observed profiles in absorption, of 4471 from several O and B type stars. Using the broadening theory of Griem and BCS and model atmospheres of the stars, they have compared their experimental profiles with theory. In general, the stellar atmospheres were not homogeneous and not in LTE and the observed profiles were composed of many profiles arising from different depths in the atmosphere and therefore from regions of widely different plasma parameters. However, Snijders and Underhill (1970), using a model atmosphere assumed to be in LTE, have obtained profiles of 4471 showing strong similarities to those in the present work.

That is, they consistently find that the observed forbidden line is significantly less intense than the theoretical forbidden line. Kodaira and Scholz (1970) have obtained similar results. Fig. 10.1 shows a typical profile of 4471 where the loss of forbidden intensity in the forbidden core can be clearly seen. Note also the theory-experiment fit in the far wings of the profile.

The conclusion drawn by both authors is that the assumption of an LTE atmosphere is invalid. This is further supported by the work of Poland (1970) who has made calculations without the LTE assumption. He has obtained agreement between theory and experiment for the ratio of allowed to forbidden peak absorption to within 3% of observed measurements. However, Poland himself points out that because of some doubt in his choice of helium abundance, which is an important parameter in his calculations, the extremely good agreement between his results and experiment could, to some degree, be coincidental. Furthermore, Snijders and Underhill (1970) make a strong criticism of one of the assumptions made by Poland in a previous work, Johnson and Poland (1969). Here, they have assumed that the 2P levels of neutral helium are in LTE with the free electrons. At astro-physical parameters, $T \sim 10{,}000 - 20{,}000^{\circ}K$ and $n_e \sim 10^{12} \sim 10^{15}$, this assumption is dubious.

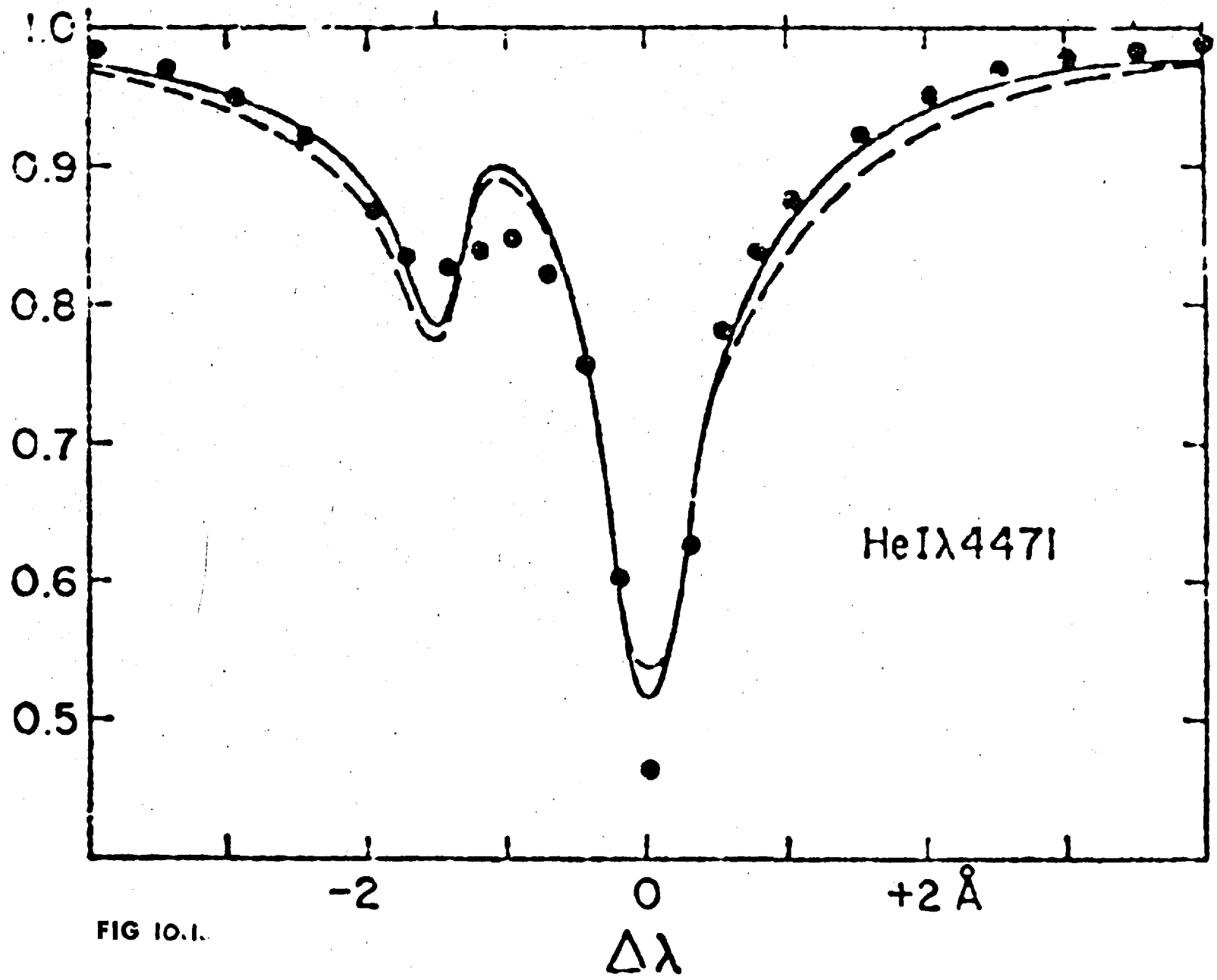

FIG 10.1.

None of the above works has considered the possibility that discrepancies have arisen because of errors in the line broadening theory itself. We wish to point out in this thesis that it undoubtedly is the broadening theory which is at fault and that, at least at first sight, the observed profiles of both Snijders and Underhill, and Kodaira and Scholz agree well with the laboratory profiles obtained here.

FUTURE WORK

The experiment has suggested two future lines of work. Firstly, on the theoretical side, much remains to be done to establish a theory capable of predicting accurately the forbidden lines at low densities. The chief requirements of such a theory are that it must account for not only ion dynamics but also non-adiabatic collisions involving the ions. The effect of the theory on present theoretical profiles must be concentrated on the forbidden line as the allowed line is accurately predicted by the present theories. The forbidden line must be broadened in such a way that the blue wing remains unaltered, the peak is reduced and the dip between the allowed and forbidden peaks is partially filled in. Finally, a reduction in the total intensity of the forbidden

line should be predicted. In the range $n_e \sim 10^{14} - 10^{15}$, this reduction should be about 10%.

On the experimental side, further useful work could be done both at the lower densities, $n_e \sim 10^{14} - 10^{15}$ and at the higher densities, $n_e = 10^{15} - 10^{17}$. In the latter case it is proposed that a much larger diameter discharge tube be built with a view to observing only a narrow column of plasma parallel to the axis of the tube and so eliminate the effects of radial gradients. A further experiment at lower densities, $n_e \sim 10^{15}$, is also proposed. The purpose is to investigate the variation of the theory-experiment discrepancy in the forbidden line with temperature. As the plasma is heated to higher temperatures, the region of invalidity of the quasi-static approximation will move further away from the forbidden line centre. Therefore a larger fraction of the forbidden line will be in a region where the ions cannot be treated on the quasi-static approximation. An experiment of this nature would provide a more sensitive test of the correct theory than measuring profiles at various electron densities because the effects of the electrons would be constant and therefore the ion effects could be studied more readily.

ACKNOWLEDGEMENTS

I would like to thank Professor W.R.S. Garton for allowing me the use of his laboratory during the course of the experiment.

Many thanks are due also to my superviser, Dr. D. D. Burgess who suggested the project and whose constant help and enthusiasm have sustained me throughout the whole of this work.

Also, all members of the spectroscopy group, in particular J. E. Jenkins, for the invaluable advice given on many occasions, S. Budd, J. Leveridge and W. Lewis, and R. Dangor, A. Chapman and S. Fielding of the plasma physics group.

To my mother, I would like to give thanks for typing the manuscript.

Finally, I would like to thank Culham Laboratories, UKAEA for financial support during the project.

REFERENCES

ASHBY, D.E.F.T. and JEPHCOTT, D.F. (1963)	Appl. Phys. Letts. 3, 13
BARANGER, M. (1958)	STIA Document No. AO 150692
BARANGER, M. (1962)	'Atomic and Molecular Processes' Ed. Bates, D.R., Ch. 13. Academic Press, N.Y.
BARNARD, A.J. COOPER, J. and SHAMEY, L.J. (1969)	Astronomy & Astrophysics. 1, 28
BERG, H.F. ALI, A.W., LINCKE, R. and GRIEM, H.R. (1962)	Physics Review, 125, 199
BURGESS, D.D. (1967)	Lecture Note, University of London (unpublished)
BURGESS, D.D. (1968)	Physics Review. 176, 150
BURGESS, D.D. (1970)	J. Quant. Sprectrosc. Rad. Trans., 10, 365
BURGESS, D.D. (1965)	Ph.D. thesis, University of London
BURGESS, D.D. (1970a)	J. of Physics B., 3, L.71
CHAPPELL, W.R. COOPER, J. and SMITH, E.W, (1969)	J. Quant. Sprectosc. Rad. Trans. 9, 149
COOPER, J. (1965)	Rep. Prog. Phys., 29, 35
DEBYE-HÜCKEL (1923)	Z. Phys. 24, 185
ECKER, G. (1957)	Z. Phys., 148, 593

GERARDO, J.B. and GUSINOV, M.A. (1969)	J. Appl. Phys. 40, 2533
GIESKE, H. (1968)	Rep. HDL - TR - 1406 (AD-687 283) Harry Diamond Labs. Washington, DC
GERDIEN, H. and LOTZ, A. (1922)	Wiss. Veröff Siemens, 2, 489
GRIEM, H.R. BARANGER, M, KOLB, A.C. and OERTEL, G. (1962)	Phys. Rev. 125, 177
GRIEM, H.R. (1968)	Astrophysics J. (1968) 154, 1111
GRIEM, H.R. (1964)	'Plasma Spectroscopy' McGraw-Hill
HINDMARSH, W.R. and FARR, J.M. (1970)	J. Phys. B., 2, 1388
HOLTSMARK (1919)	Ann. Phys. 79, 744
HOOPER, C.F. (1968)	Phys. Rev. 165, 215
JENKINS, J.E. (1970)	Ph.D. thesis, University of London (unpublished)
JOHNSON, H.R. and POLAND, A.J. (1969)	J. Quant. Sprectosc. Rad. Trans., 9, 1151
KODAIRA, K. and SCHOLTZ, M. (1970)	Astron. & Astrophys., 6, 93
KHINCHINE, A. (1934)	Maths. Ann. 109, 604
LEWIS, M. (1961)	Phys. Rev., 121, 501
LORENTZ, H.A. (1906)	Proc. Roy. Acad. Sci. (Amsterdam), 8, 591

MARGANAU, M. and LEWIS, M (1959)	Rev. Mod. Phys., 31, 569
McCARTAN, D.G. and HINDMARSH, W.R. (1970)	J. of Physics B., 2, 1396
MOZER, B. and BARANGER, M. (1959)	Phys. Rev. 115, 521
NELSON (1970)	Ph.D. Thesis, University of British Columbia (unpublished)
SADJIAN, H. WIMMEL, H.K. and MARGANAU, H. (1961)	J. Quant. Spectrosc. Rad. Trans. 1, 46
SPITZER, L. (1962)	'Physics of Fully Ionized Gases' Interscience pub.
STRUVE, O. (1929)	Astrophys. J., 70, 85
SNIJDERS, M.A.J. and UNDERHILL, A.B.	(unpublished)
UNDERHILL, A.B. (1966)	'The Early Type Stars' D. Reidel Pub. Co., Dordrecht - Holland
VOSLAMBER, D. (1969)	CEA - Euratom Rep. EUR - CEA - FC - 527
WOLFF, H. (1958)	Z. Phys., 150, 614

Journal of Physics B
Atomic and Molecular Physics

Letters to the Editor

Experimental observations of the profiles and relative intensities of He I 2^3P–4^3D (λ 4471) and 2^3P–4^3F (λ 4470) at low electron densities

Abstract. Accurate profiles of the astrophysically important He I 4471 Å transition and its associated forbidden component have been obtained for the first time in a laboratory plasma of independently known electron density at electron density values comparable to those in B-class stars. Comparison of the experimental profiles with the most recent and accurate theoretical predictions shows very good agreement for the halfwidth and profile of the allowed component and for the profile of the far wing of the forbidden component, but a very considerable discrepancy exists between theoretical and experimental values of the intensity near the peak of the forbidden component.

Optically forbidden ($\Delta l = 0 \pm 2$) transitions appearing in the wings of allowed neutral helium lines are prominent features of the spectra both of laboratory plasmas, and of early (O and B) type stars, being induced by the electric microfield in the plasma and the resultant breakdown of the parity selection rule. In the stellar case, the Stark-broadened profiles of the allowed lines and the intensities of the Stark-induced forbidden components relative to those of the associated allowed transitions are important as a means of determining surface densities, and hence gravities, and/or helium abundances. Theoretical estimates of such forbidden component intensities have been made (and used astrophysically) for many years. However, the first full calculations of the profiles and intensities of allowed and forbidden components of astrophysically important He lines, including both ion and electron contributions to the broadening and treating the latter by means of the modern theory of electron impact broadening, have been carried out only very recently by both Barnard *et al.* (1969), and by Griem (1968). The only previous experimental profile study of the astrophysically important He I 4471 line was an early study by Wulff (1958) at an electron density in excess of astrophysically interesting values, and of the experiment reported here, by about a factor of 30.

Recently we have obtained detailed profiles of the He I 2^3P–4^3D (λ 4471) line and the nearby 2^3P–4^3F (λ 4470) forbidden component for electron densities in the

range 4×10^{14} cm^{-3} $< n_e < 2 \times 10^{-15}$ cm^3. These observations were made on the late afterglow phase of a critically damped linear pinch similar to that discussed by Burgess *et al.* (1967). At the times of interest the plasma was current free, and had expanded to fill the 4·2 cm inner diameter, 70 cm long discharge vessel. n_e was measured both on and off the axis interferometrically, using the 3·39 μm transition of a He–Ne laser, and the feedback technique developed by Ashby and Jephcott (1963). To within experimental error ($\pm$ 10%) the density was found to be constant in the central region of the tube used for the spectroscopic observations. Electron temperature estimates were obtained from line-to-continuum observations, and were of the order of 8000 K. (The line profiles are not sensitive to the electron temperature.) The published theoretical profiles already include Doppler broadening, and the effective Doppler temperature for neutral He was therefore measured experimentally by observing the negligibly Stark-broadened He I 4713 Å line. Under conditions of interest the effective Doppler temperature was 13 500 K, and as such the Doppler width increased the total width of the He I 4471 Å transition by about 15%.

Line profiles were obtained by scanning in discrete wavelength steps on a shot-to-shot basis with a 1 m Czerny–Turner photo-electric recording spectrometer, and recording the resultant time histories on a cathode ray oscilloscope, the discharge being exceptionally reproducible in the afterglow region, (e.g., see the small scatter in experimental points, figure 1). Profiles taken on quite separate runs were identical in all respects. The instrumental width was 0·15 Å in comparison with Stark-broadened widths typically of 0·5 Å, and the effects of instrumental broadening were included in comparing experimental and theoretical profiles by numerically convolving the theoretical line profile corresponding to the independently measured electron density with the measured instrumental profile. Resultant corrections to the profile were small. Great care was taken to observe only a region of the plasma of uniform electron density, earlier work in this laboratory at higher electron densities (J. E. Jenkins, Ph.D. thesis to be published) having shown the previously inadequately appreciated importance of high plasma homogeneity in studying forbidden-line profiles. Besides limiting observations to emission from a central 1 cm radius region of the plasma column (radius 2 cm) within which measured electron densities were known to be constant, the homogeneity was further checked by varying the radius of the observed emitting region by a factor of 3 within the central homogeneous zone, with no observable effect on the measured line profiles. The optical depth was measured at each point in the line profile by placing a high brightness pulsed continuum source behind the plasma and observing the transmission directly. A correction was applied for finite optical depth (approximately unity at the peak of λ 4471) where necessary (see below). Measured and theoretical profiles were compared by normalizing both to unit total intensity and superimposing them. (This procedure discriminates against any small residual effects of density inhomogeneities better than normalization to peak intensity of the allowed component, since low-density regions would contribute most in the latter region.) The experimental results for $n_e = 10^{15}$ cm^{-3} are shown in comparison with the theoretical predictions of Barnard *et al.* and of Griem, in figure 1.

Contributions to the profile due to Doppler and instrumental broadening are both small, and in this density range the theoretical predictions of the halfwidth of He I 4471 are accurate to better than 10%. Similarly, the theoretical profiles of the whole allowed component and of the far wing of the forbidden component are also in excellent agreement with experiment. However, a major discrepancy exists between the experimentally measured intensity near the peak of the forbidden component and

the predictions of both theories. This discrepancy is much larger than the difference between the two separate theoretical calculations, and also is considerably too large to be accounted for by experimental errors. Inhomogeneities in the plasma or errors in the correction for optical depth sufficient to cause the observed discrepancy are

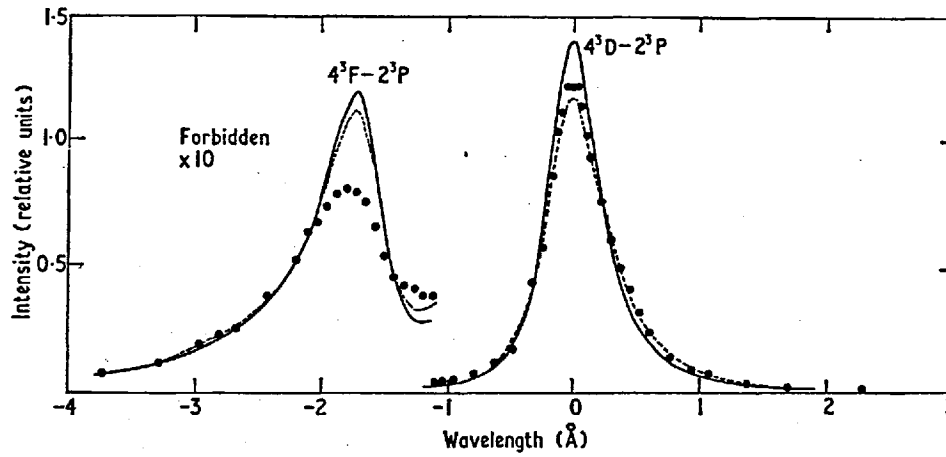

Figure 1. Comparison of experimental profiles (full circles) for He I 4471 Å 2^3P–4^3D and 4470 Å 2^3P–4^3F with theoretical predictions of Barnard *et al.* (full curve) and of Griem (broken curve) at $n_e = 10^{15}$ cm^{-3}, $T = 10\,000$ K.

ruled out entirely by the experimental technique, but in any case would also produce considerable disagreement between theory and experiment in other regions of the profile, including the halfwidth of the allowed component, since both effects primarily modify the peak height of the latter. A similar discrepancy has also been observed for He I 4921 Å, where optical depth corrections are much smaller.

It therefore appears that at these electron densities a real and very sizeable discrepancy exists in theoretical predictions of both peak and total intensities of the forbidden 2^3P–4^3F component. This discrepancy seems too large to be accounted for by errors in evaluating the matrix elements involved in the calculations of the static Stark effect of the ions. In any case, such errors in the matrix elements would modify the ion contribution to other regions of the profile, particularly the far wing of the forbidden component, and would also reduce the predicted electron impact broadening, neither of which effects is observed.

The two theoretical predictions differ most in the region between the allowed and forbidden components. Since in both theories the quasi-static ion broadening primarily splits the 4^3D and ^3F levels, the intensity between the allowed and forbidden components is due almost entirely to electron impact broadening, and it is this region that is most sensitive to differences in the treatment of electron correlations. Barnard *et al.* used the recently corrected treatment of Debye shielding of electron impact broadening (Chappell *et al.* 1969, Burgess 1970), yielding a lower intensity than the previously accepted theory used by Griem. The experimental results lie consistently high of *both* calculations. No conclusions can be drawn therefore about either approach in so far as their treatment of electron correlations is concerned, other than that some larger contribution to the intensity has been missed in both

calculations. In view of the lowering of the peak intensity of the forbidden component, the most natural explanation is probably an unaccounted for (dynamic) contribution to the broadening of the forbidden component spreading intensity into the region between the two lines.

In the following paper some comments are made on the validity of the theoretical calculations of the profiles of these lines, with particular attention to the usual justification of the quasi-static model for the ion broadening as used in both theories. A fuller description of the experimental set-up and line profiles for He I 4471 Å and 4921 Å taken over a wider range of densities will be published in due course.

The authors would like to acknowledge many useful discussions with J. E. Jenkins. C. J. Cairns was supported under a contract from UKAEA Culham Laboratory, as partially was the experimental work.

Physics Department,
Imperial College of Science and Technology,
London, S.W.7.

D. D. Burgess
C. J. Cairns
22*nd May* 1970

Ashby, D. E. T. F., and Jephcott, D. F., 1963, *Appl. Phys. Lett.*, **3**, 13–6.
Barnard, A. J., Cooper, J., and Shamey, L. J., 1969, *Astron. Astrophys. J.*, **1**, 28–36.
Burgess, D. D., Dangor, A. E., and Jenkins, J. E., 1967, *Br. J. Appl. Phys.*, **18**, 1281–5.
Burgess, D. D., 1970, *J. Quant. Spectrosc. Radiat. Transfer*, **10**, 365–71.
Chappell, W. R., Cooper, J., and Smith, E. W., 1969, *J. Quant. Spectrosc. Radiat. Transfer*, **9**, 149.
Griem, H. R., 1968, *Astrophys. J.*, **154**, 1111–22.
Wulff, H., 1958, *Z. Phys.*, **150**, 614–31.

Some comments on present theoretical calculations of the profiles of forbidden components in the wings of Stark-broadened spectral lines

Abstract. Objections are raised to the basic theoretical validity of all previous calculations of the intensities and profiles of optically forbidden transitions induced by the electric microfield in a plasma. These theoretical objections are relevant in the case of neutral helium lines at the densities of interest in early-type stars when such forbidden components are strongly excited. They also relate to the discrepancy between theory and experiment reported in the preceding experimental letter.

The preceding letter has reported detailed observations of the profiles and intensities of the He 4471 Å line (2^3P–4^3D) and the associated 2^3P–4^3F forbidden component at relatively low electron densities. As discussed there, whilst the experimentally observed halfwidth and profile of the allowed component and the shape of the far wing of the forbidden component are in excellent agreement with the recent calculations of Barnard *et al.* (1969) and of Griem (1968), there is a severe discrepancy in intensity in the region of the centre of the forbidden component, the experimental value being considerably lower than theoretical predictions. In this paper a very basic